Coastal sources of estuarine inflow

Elizabeth Brasseale

A dissertation

submitted in partial fulfillment of the

requirements for the degree of

Doctor of Philosophy

University of Washington

2020

Reading Committee:

Parker MacCready, Chair

LuAnne Thompson

Julie Keister

Program Authorized to Offer Degree:

School of Oceanography

University of Washington

Abstract

Coastal sources of estuarine inflow

Elizabeth Brasseale

Chair of the Supervisory Committee:

Parker MacCready

School of Oceanography

This dissertation considers the source of water that enters estuaries from the coastal ocean using a series of realistic and idealized ocean models. The first project examines the source of planktonic larvae of the marine invasive species, the European green crab (*Carcinus maenas*), which was observed in the eastern Salish Sea for the first time in 2016. Green crab spawns were simulated using particle tracking experiments in an ocean model of the eastern Pacific Ocean to investigate the likelihoods that larvae released from four potential source locations on the West Coast could be successfully transported into the eastern Salish Sea. The project determined that particle release timing and oceanographic processes (i.e. flow reversals in the Strait of Juan de Fuca) played a role in the probability of successful transport. The next project examined the sources of inflow to an estuary in an idealized three-dimensional primitive equation model with simple forcing. The model grid features an estuarine channel next to a sloping, unstratified shelf with mixing provided by a

single frequency, 12-hour tide. Inflow is identified using Total Exchange Flow method (MacCready, 2011) in conjunction with particle tracking. When there are no shelf currents, the source of inflow is influenced by planetary rotation. In this instance, there may be important interactions between inflow and outflow. However, the third project demonstrates the response of estuarine inflow to the introduction of wind stress, also using idealized models. The rates and paths of estuarine inflow are found in five surface-forcing experiments: one control case without wind stress, two with downwelling-favorable wind stress, and two with upwelling-favorable wind stress. In these experiments, the source of inflow on the shelf is determined primarily by the direction of wind stress, and the impact of planetary rotation is much less significant. The last project considers the sources of inflow to the Strait of Juan de Fuca under two wind conditions. This was done using two particle tracking experiments and a realistic model of the Salish Sea and neighboring Pacific Ocean. In both experiments, inflow was sourced laterally from the up-wind direction. The Juan de Fuca canyon was a source of deep inflow in both experiments, suggesting submarine canyons may be an important conduit of inflow under all wind stress conditions. The results suggests that wind stress may be less important than other shelf dynamics on time scales longer two weeks.

TABLE OF CONTENTS

LIST OF FIGURES

LIST OF TABLES

ACKNOWLEDGEMENTS

This project has been funded wholly or in part by the United States Environmental Protection Agency under assistance agreement PC-00J90701 through the Washington Department of Fish and Wildlife (WDFW). The contents of this document do not necessarily reflect the views and policies of the United States Environmental Protection Agency (EPA) or the WDFW, nor does mention of trade names or commercial products constitute endorsement or recommendation for use. This project was additionally funded by the National Science Foundation under grant OCE-1634148. The work in this dissertation is coauthored by Parker MacCready. Chapter 2 was coauthored by Emily Grason, P. Sean McDonald, and Jeff Adams.

There are many people who facilitated this dissertation who need to be acknowledged. Parker MacCready designed this project and contributed his mentorship and unique sense of humor every step of the way. My committee, LuAnne Thompson, Julie Keister, and Alex Horner-Devine, were wonderful in their ongoing advice and support. The UW Oceanography graduate student community has been an amazing resource both academically and personally, and I need to especially recognize the members of my cohort who were with me for six years or more: Hally, Jake, Marta, Shirley, and Elisa. In particular, I want to thank Hally for being there with me on our eerily parallel trajectories. I also need to thank Jake for being my “work husband”, spending hours a day with me every day for six and a half years, during which time I learned as much about visual

design, smooth jazz, and space travel as I did about physical oceanography. Sarah and Katy were also in my office family, and they made OSB 331 feel like home. The friends I saw regularly for D&D and writing the *Touch Tank* were also central to my graduate school experience. I carry those friendships in my heart. I need to thank my Mom, Dad, and my siblings Mary, John, Nancy, and Richard for their unending love. Finally, this dissertation would not have been possible without the love and support of my partner Dan Bentson, for filling my mornings and evenings with laughter, affection, and conversation. Your wisdom and goodness are unmatched.

I would like to acknowledge that this dissertation was written during two coincident national emergencies, the coronavirus pandemic and the nationwide uprisings in response to the death of George Floyd. Thank you to the anti-racist activists who have organized and continue to organize during this moment of elevated social consciousness, especially to those who are working to reform academia.

Chapter 1. INTRODUCTION

The most rewarding aspect of studying earth science is the practice of connecting theory to place. The research in this dissertation was undertaken at the University of Washington in a north-facing office of the Ocean Sciences Building, overlooking the Montlake Cut which connects Lake Washington to Puget Sound, a glacially-carved, fjord-like estuary. Puget Sound is part of the Salish Sea, an inland sea in the Pacific northwest shared by the United States and Canada, which also includes the waters of the Strait of Juan de Fuca and the Strait of Georgia. As is typical for fjord-like estuaries, the branches of Puget Sound are deep and narrow, creating a body of water that is on the salty and stratified extreme for estuaries (Geyer and MacCready, 2014). Consequently, 80–90% of the water in Puget Sound is Pacific Ocean water. The question driving this dissertation is, where in the coastal ocean did that water originate? That question is important because it connects all of the activity of the eastern Pacific Ocean into Puget Sound. Such activity includes seasonal and interannual deoxygenation in the eastern Pacific region (Crawford and Peña, 2013) which is communicated to Puget Sound (Feeley et al., 2010). Understanding the connection from the coastal ocean to Puget Sound is also key in assessing the inevitability that marine invasive species on the west coast of the United States and Canada may expand their range inland (Behrens Yamada, 2017; Grason et al., 2018). These phenomena are of interest because Puget Sound sustains charismatic megafauna, calcium-carbonate-shelled filter feeders, culturally-significant anadromous fish, keystone zooplankton, and the curiosity of oceanographers.

In some ways, the research in this dissertation is motivated by an attempt to understand or predict anomalies. This is the case with Chapter 2, which asks, “Why are European green crabs found in the Salish Sea now for the first time after being on the West coast for thirty years?” This question is addressed using particle tracer experiments that are programmed to behave like green crab larvae in a realistic numerical model of the Salish Sea and neighboring eastern Pacific Ocean.

However, exploration of broader questions such as, “How will business-as-usual change in Puget Sound as the eastern Pacific Ocean responds to climate change?” is complicated by a lack of understanding of the paths by which coastal ocean water reaches estuaries in general. The literature purporting a general theory for estuarine inflow is limited to analytical studies using two-layer oceans (Beardsley and Hart, 1987; Masse, 1990). This problem rose to become one of the central aims of this thesis: to build up a clearer picture of the process of estuarine inflow, using modern modeling resources and analyses. This is first done in a base case study in Chapter 3 and then in four experiments with alongshore wind stress in Chapter 4. Both these chapters use idealized estuary-shelf models with simple geometries. Inflow is identified using a combination of particle tracking experiments and exchange flow calculations in different parts of the model using the Total Exchange Flow method (MacCready, 2011; Lorenz et al., 2019).

In 0, the theory developed in Chapters Chapter 3 and Chapter 4 is applied in a return to the prime directive — where did water in Puget Sound originate in the coastal ocean? This chapter contains an analysis of two preliminary particle tracking experiments set during samples of each of the two wind regimes experienced in the Pacific northwest. These experiments use a more recent

version of the Salish Sea model than that used in Chapter 2. This final chapter by no means culminates the work on this question. Rather, it lays down a springboard for future experiments and observations to find the sources of inflow to the Salish Sea and more generally to all estuarine and fjord systems around the planet.

Chapter 2. Larval transport modeling support for identifying population sources of European green crab in the Salish Sea

An edited version of this chapter was published in *Estuaries and Coasts*, Copyright 2019: Brasseale, E.A., E.W. Grason, P.S. McDonald, J. Adams, and P. MacCready, 2019. Larval transport modeling support for identifying population sources of European green crab in the Salish Sea. *Estuaries and Coasts*, 42: 1586–1599, doi:10.1007/s12237-019-00586-2.

2.1 Introduction

The European green crab (*Carcinus maenas*, henceforth green crab) is frequently listed among the most damaging invasive species worldwide (Narberhaus, 2018). This species has established populations in several temperate marine habitats including southeastern Australia and Tasmania, Argentina, South Africa, and both coasts of North America (le Roux et al., 1990; Geller et al., 1997; Carlton and Cohen, 2003; Thresher et al., 2003; Ahyong, 2005; Hidalgo et al., 2005). In locations where green crabs are abundant, primary direct impacts occur via competition with and predation on native species (Grosholz et al., 2000; Whitlow 2009; de Rivera et al. 2011) and occasionally indirectly via facilitation (Grosholz, 2005) or trophic cascades (Kimbro et al., 2009). Increasing evidence also suggests that green crabs can damage seagrass beds and impede their restoration through mechanical disturbance and uprooting while foraging (Malyshev and Quijon, 2011; Neckles, 2015; Matheson et al., 2016), as well as by consuming both meristem tissue and seeds of the plants (Malyshev and Quijon, 2011; Infantes et al., 2016). These habitat impacts are associated with significant declines in abundance and biomass of seagrass-associated fish and shifts in community structure (Matheson et al., 2016).

The presence of green crabs on the west coast of North America was first detected in 1989–1990 in southern San Francisco Bay (Cohen et al., 1995; Grosholz and Ruiz, 1995). Genetic studies subsequently confirmed the source population as the North American east coast (Darling et al., 2008), the species most likely having been introduced unintentionally in shipments of bait or seafood (Carlton and Cohen, 2003). Local population growth and larval dispersal permitted spread to nearby embayments to the north and south of San Francisco Bay by 1994 (Grosholz and Ruiz, 1995). Range expansion since then has been primarily northward; advection and survival of larvae in this direction is stronger during years with positive Pacific Decadal Oscillation (PDO) and El Niño Southern Oscillation (ENSO) indices (Behrens Yamada and Kosro, 2010). Green crabs were first detected in embayments of Oregon and Washington (United States) and British Columbia (Canada) in 1997–1999 (Behrens Yamada, 2001; Jamieson et al., 2002), coinciding with years of extremely high ENSO indices. Populations are now established in coastal fjords on the west coast of Vancouver Island and have continued to spread northward episodically (Klassen and Locke, 2007; Gillespie et al., 2015; DFO, 2018), presumably facilitated by local production and retention of larvae (Banas et al., 2009; Behrens Yamada et al., 2015; DiBacco and Therriault, 2015). By contrast, green crabs are only periodically abundant in coastal embayments of Oregon and Washington, appearing to rely on advection of larvae from established populations farther south (Behrens Yamada and Gillespie, 2008; Behrens Yamada et al., 2015).

Despite being present in coastal embayments of Oregon, Washington, and British Columbia, no green crabs were observed in the Salish Sea, an inland sea of Washington State (Grason et al.,

2018) and southern British Columbia (Figure 2.1), throughout the 2000s. Jamieson et al. (2002) attributed the paucity of green crab sightings in the region to hydrogeographic conditions in the Strait of Juan de Fuca that might inhibit incursions of larvae because prevailing surface currents are seaward. In 2012 an established population, consisting of multiple year classes, was discovered in Sooke Basin, 40 km west of Victoria, British Columbia (Curtis et al., 2015) and well within the Strait of Juan de Fuca (Figure 2.1). The current strongest hypothesis for the route of introduction for that population was the transfer of contaminated bags of mussels from Clayoquot Sound, an infested embayment on the outer coast of Vancouver Island. We base this inference on two lines of evidence. First, Department of Fisheries and Oceans Canada (DFO) carried out an investigation that surmised this to be the most probable source (T. Therriault, pers. comm). In addition, ongoing genetics work (Tepolt et al., in prep) demonstrates that the population in Sooke Basin does not show connectivity with populations either on the United States west coast or from Barkley Sound. Thus, the green crab seemingly overcame the apparent oceanographic barrier via human-mediated transport into the western portion of the Salish Sea.

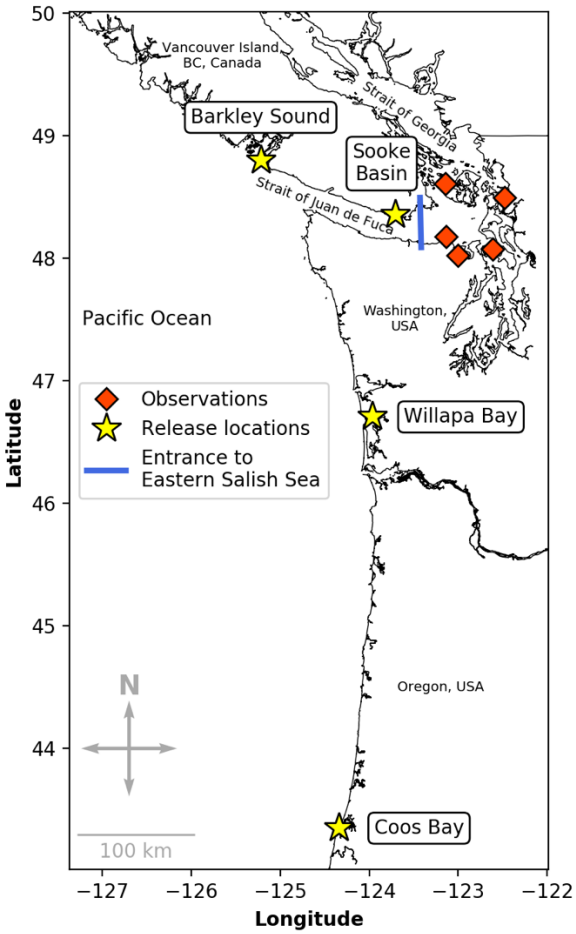

Figure 2.1 Map of study area showing Pacific northwest coastal ocean and Salish Sea, which contains Strait of Juan de Fuca, Strait of Georgia, and waters further inland including the Puget Sound. Eastern Salish Sea delineated from Strait of Juan de Fuca by blue line. Orange diamonds = confirmed green crab observations in eastern Salish Sea. Yellow stars = larval release locations.

Following discovery of the population in Sooke Basin, early detection monitoring was initiated in Washington State in 2015. A distributed citizen science network of sentinel sites was established, resulting in the first confirmed green crab detections eastward of Vancouver Island in 2016 on San Juan Island and in Padilla Bay (Grason et al., 2018). Since that time, green crabs have been found at very low abundances at four additional locations in the eastern Salish Sea (Figure 2.1). Two lines of evidence support the inference that green crabs have only recently

(2014 or later) arrived in the eastern Salish Sea. Firstly, monitoring in this region from 2000–2010 found no green crabs (WDFW, unpublished data). Second, sizes of all recent captures indicate these individuals belong to year classes of 2014 or thereafter (Grason et al., 2018). Moreover, it is likely these new detections resulted from 'natural' dispersal of larvae rather than by human-mediated transport because crabs of similar size/age were observed in multiple disparate locations not associated with known transport vectors (e.g., ballast water exchange at ports, seafood distribution centers, shellfish aquaculture activities).

Identifying the pathways by which green crab larvae can penetrate into the eastern Salish Sea and understanding the oceanographic processes responsible for successful recruitment are critical to management of the species in Washington State and British Columbia, as well as ongoing transboundary cooperation to control spread in the region. Here we considered whether Sooke Basin was the likely larval source for green crabs observed in the eastern Salish Sea or if larvae could have arrived from the Pacific Coast. Grason et al. (2018) suggested a Sooke Basin origin as the most parsimonious explanation if the Strait of Juan de Fuca represents an oceanographic barrier to transport of invasive larvae. However, it was recently postulated that periodic flow reversals caused by storms can transport larvae from coastal sources eastward through the Strait of Juan de Fuca (Behrens Yamada et al., 2017). Under normal conditions, flow in the upper water column is westward within the Strait of Juan de Fuca, preventing eastward transport of coastal larvae inhabiting near-surface waters. During flow reversals, which occur in fall and winter and less frequently in spring and summer (Frisch et al., 1981), near-surface flow changes direction and moves eastward in the Strait of Juan de Fuca, enabling eastward advection of invasive larvae (Thomson et al., 2007; Giddings and MacCready, 2017). Thus, the goal of the

present study was to evaluate the likely source population for larvae that arrived in the eastern Salish Sea, given what is known about the present distribution of green crabs along the west coast of North America.

We used an oceanographic circulation model to explore likely sources and seasonal timing of larval releases that might have contributed to the observed distribution of green crabs captured within the eastern Salish Sea. In so doing, we evaluated three questions:

1. Given observed ocean conditions, what is the relative probability that larvae released from nearby locations with known populations of green crabs could be transported into the eastern portion of the Salish Sea?
2. Based on current understanding of green crab larval dynamics and seasonality, when is transport of larvae into the eastern Salish Sea likely to be most successful?
3. What oceanographic conditions and mechanisms are likely to support successful transport of green crab larvae into the eastern Salish Sea?

2.2 Methods

2.2.1 *Green Crab Larval Biology*

Although few data exist concerning the general biology, life history, and development of *Carcinus maenas* in the northeastern Pacific, Atlantic populations have been studied extensively. Generally, the timing of reproductive events depends on latitude (Queiroga, 1996), and reproduction can occur over only a few months (Berril, 1982) or throughout the year (Queiroga, 1996), depending on seasonal temperatures. After mating, female crabs can release embryos more than once within a year; the number of broods produced is dependent on the length of the

reproductive season and resource availability. Several authors have suggested that shallow mid-latitude estuaries of the northeastern Pacific meet these conditions (Cohen et al., 1995; Behrens Yamada, 2001; Jamieson et al., 2002). Banas et al. (2009) report ovigerous females in Willapa Bay, Washington from January through July, while DiBacco and Therriault (2015) observed ovigerous females over a shorter interval (mid-February to June) in British Columbia.

Females carry their broods for several months, and egg development is temperature-dependent. Behrens Yamada (2001) reported females remaining ovigerous for 2–3 months at 12 °C (December–February). Once embryos are fully developed, female crabs may move toward the mouths of estuaries where hatching occurs, typically over successive nighttime high tides or soon thereafter (Queiroga et al., 1994). The timing of release has important implications for the export of larvae since the subsequent ebbing tide will flush them from the estuary (Zeng and Naylor, 1996a).

Larvae develop through four zoeal and one megalopa stage before settlement occurs 4–9 weeks after hatching, but again this is dependent on water temperature (Dawirs, 1985; Nagaraj, 1993; de Rivera et al., 2007). In laboratory experiments, total development time to first benthic instar was 32 and 62 d at 18 °C and 12 °C, respectively (Dawirs, 1985); average development at 12.5 °C is 59 d (de Rivera et al., 2007). Field results provide similar estimates, and Queiroga (1996) found that development occurred in 56 d at 13.5 °C and at a salinity of 35.

Larval abundance peaks April–July in the northeastern Atlantic and North seas (Lindley, 1987), while near the southern geographic limit of the species' native range, larvae are abundant during

two periods: February–April and October–December (Sprung, 2001). Development takes place on the continental shelf (Lindley, 1987; Queiroga, 1996). In Portuguese waters, Queiroga (1996) found that larvae were restricted to the inner and middle shelf, with zoeae 1 occurring closest to coastal estuaries and the later zoeae stages furthest offshore (15–20 km). Megalopae were also present nearshore, which indicates onshore transport of that stage. According to Queiroga (1996), all larvae were collected within 45 km of the Portuguese coast.

2.2.2 *Experimental overview*

A model was used to recreate ocean conditions from 2014–2016 and larval releases were simulated in the source locations (described below) as separate particle tracking experiments. 10,000 particles were released per experiment in order to provide a statistical distribution of possible transport paths of planktonic crab larvae. Though an individual female green crab can release several hundred thousand larvae in a single brood (Griffen, 2014), this number of particles was chosen to provide a relatively high-resolution distribution while balancing computational demands of particle tracking experiments. For each experiment, the particles were released from a single location and tracked for 75 d. Experimental releases were conducted on one day per month during periods when green crabs are known to release larvae (see section on *Particle release timing* below) in order to sample ocean conditions during different seasons. After the tracks were generated, the success of the invasion was determined by calculating the percentage of the 10,000 released particles transported into the eastern Salish Sea during a competency window (see section on *Particle development* below). This percentage was interpreted as the likelihood that a crab larva would reach the eastern Salish Sea if released from that location at that time.

2.2.3 *Modeling tools*

The ocean model was built in the Regional Ocean Modeling System (ROMS) (Shchepetkin and McWilliams, 2005), a free surface, hydrostatic, primitive equation model. The model was forced with atmospheric, tide, river, and ocean boundary conditions to simulate the 3D circulation and water properties throughout the domain. It does not include wetting and drying in intertidal zones. The model included 16 river point sources using daily discharge values from the United States Geological Survey (USGS, http://waterdata.usgs.gov/usa/nwis/) and Environment Canada (http://www.wsc.ec.gc.ca/applications/H2O/). These include 14 Puget Sound rivers, the Fraser River, and the Columbia River. Eight tidal constituents derived from the 1/4° TPXO7.2 inverse global tidal model (Egbert and Erofeeva, 2002) were forced at the open boundaries. Meteorological forcing of surface pressure, wind, air temperature, relative humidity, shortwave radiation, downward longwave radiation, and rainfall were taken from a Weather Research and Forecasting regional model with 12-km resolution (Mass et al., 2003). Open ocean boundary conditions for daily-averaged velocity, salinity, temperature and sea surface height came from the HYCOM global model (HYbrid Coordinate Ocean Model, http://hycom.org/). The river, atmosphere and ocean-forcing models were data-assimilative and so did an excellent job of keeping their forecast fields close to observations. The grid horizontal resolution was 1.5 km on the shelf, and 4.5 km far offshore. There were 40 vertical levels, distributed from the seafloor to the sea surface, giving excellent resolution of both bottom and near-surface processes. The large domain allowed important interactions between the inland and coastal waters, for example the influence of coastal upwelling and the Columbia River plume on the inflow to the Strait of Juan de Fuca. The ocean circulation model has been extensively validated in terms of currents,

temperature, salinity, sea surface height, and biogeochemistry by hindcast experiments from 2004–2007 (Davis et al., 2014; Giddings et al., 2014; Siedlecki et al., 2015).

The particle model is a separate program that uses the output of the ocean model. The integration required to get the horizontal positions for the particles from the ocean circulation output was done following methods developed in previous particle tracking projects (Banas et al., 2009; Giddings et al., 2014). Particle tracks were calculated by forward integration in time using bi-linear interpolation of the archived hourly snapshots of 3D velocity fields and 2nd-order Runge-Kutta integration. A 3600-second time step was used which resolved tidal oscillations. Experiments using shorter time steps and 4th-order Runge-Kutta integration gave very similar results.

Particles migrate vertically in the water column since all stages of green crab larvae exhibit diel vertical migration (DVM) (Queiroga et al., 2002), and vertical position significantly impacts horizontal transport (Queiroga et al., 1997). The vertical positions of the particles were programed to move to 3-m depth at sunset and to 15-m depth at sunrise, which is consistent with field observations in British Columbia (DiBacco and Therriault, 2015). Although we chose to time the migration of our particles with the photoperiod, other vertical migratory behaviors such as endogenous tidal rhythms have been observed in green crabs in other environments in the field (Zeng and Naylor, 1996), so applying this behavior to all green crab larvae stages in all locations introduces uncertainty in our results. These water column positions were based on observations of DVM for zoeae I and megalopa but were used for all zoeal stages despite evidence that DVM varies due to the lack of observations of zoeal stages II-IV (DiBacco and

Therriault, 2015) and the difficulty of approximating larval development in rapidly changing ocean conditions (as described below in *Particle development*). Swimming rate (0.6 cm s^{-1}; Mileikovsky, 1973) was not resolved in this DVM model since we observed that larval swimming rates could overcome displacement from vertical diffusion the vast majority of the time (>99.9% of model time steps). Most complications in particle tracking arise from difficulties in treatment of vertical diffusion due to turbulence (Visser, 1997; Banas et al., 2009), however by prescribing vertical position as a function of time, that difficulty was avoided.

2.2.4 *Particle release locations*

Four sites where green crabs have been detected were evaluated as possible origins of green crabs in the eastern Salish Sea: Barkley Sound and Sooke Basin (British Columbia, Canada); and Willapa Bay, Washington, and Coos Bay, Oregon (United States). These sites were selected to encompass dispersal patterns that could transport larvae into inland waters from across the range of the green crab on the North American west coast: Morro Bay, California (Carlton and Cohen 2003) to Bella Bella, British Columbia (Gillespie et al. 2015).

Sooke Basin was considered a likely source based on proximity to sites where green crabs were captured in 2016 and 2017 (Grason et al. 2018). Prior to those observations, Sooke harbored the only confirmed population of green crabs in the Salish Sea. When first detected in 2012, the population in Sooke was already sufficiently abundant to be considered established and has remained so since that time (Gillespie et al. 2015; T. Therriault, pers. comm.). Subsequent surveys of embayments on the Strait of Juan de Fuca portion of Vancouver Island and the Southern Gulf Islands in 2013 and 2016 found no green crabs, and a repeat survey in 2017 found

only a handful of individuals at one adjacent site, Becher Bay (T. Therriault, pers. comm.), suggesting Sooke Basin was a likely source of propagule origin within the Salish Sea.

Green crabs have been detected, at least periodically, in all three coastal sites (Barkley Sound, Willapa Bay, and Coos Bay) since at least 1999, though abundances across these sites, and over time, have varied by several orders of magnitude (Behrens Yamada et al. 2013; Gillespie et al. 2015). Barkley Sound was selected as representative of northern source populations because of its relative proximity to the Salish Sea and because it has the highest crab abundance of all sites surveyed in British Columbia (Behrens Yamada et al. 2013; Gillespie et al. 2015). The Columbia River plume (on the border between Washington and Oregon) can significantly impact along- and cross-shelf dispersal of plankton because the density difference poses a barrier between the plume and the coastal ocean (Banas et al. 2009; Peterson and Peterson 2009). Plankton outside of the plume can have their alongshelf transport blocked by the plume, and, if entrained into the plume, the plankton will be transported by the plume. We addressed the potential role of the plume by selecting release sites both north and south of the Columbia River. Willapa Bay was chosen as a particle release site to the north of the plume because green crabs have been detected more frequently and at higher abundances in that estuary compared to Grays Harbor. Among the four larval release sites explored in the present study, however, Willapa Bay has the smallest population of adult green crabs, and the species has been undetectable during periods when conditions were unfavorable to northward larval dispersal (Behrens Yamada et al. 2013). Lastly, we chose Coos Bay, Oregon, to represent possible source populations to the south of the Columbia River plume.

The relative freshness of the Columbia River plume poses a problem for green crab larvae during springtime, since laboratory studies have shown that larvae do not survive in a salinity 20 or less (Bravo et al. 2007). The Columbia River plume salinity varies seasonally with the magnitude of river flow. The river flow is highest in the spring, freshening the plume to a salinity of 5–15, below the survivability threshold. In late summer through winter, flow rates are lower and the plume salinity is between 20–25, which is sufficiently saline for survival of entrained larvae (Nash et al. 2009).

For each of the particle release sites, the specific location of release was chosen to be as close to the mouth of the bay as possible while still near a location where green crabs have been found. For example, particles in Willapa Bay were released just offshore of Toke Point (Banas, et al. 2009). This is in line with the Queiroga et al. (1994) finding that ovigerous green crabs migrate towards the mouths of estuaries when their larvae are released (described in *Green crab larval biology* above) while also maximizing the likelihood that the released particles would exit the embayments and reach the coastal ocean. The impact of this choice is that particles leave the embayments sooner than they would if they were released at the head. Particles released at the head might take days or weeks longer to exit the embayment into the coastal ocean, or they might not exit the embayment at all. This impact has only been tested for one of the four source locations used in this study (Willapa Bay in Banas et al. 2009) where self-retention was shown to be possible for particles released away from the mouth, and the magnitude of retention is higher in summer than in spring. However, this result cannot easily be extrapolated to the other source locations because of the differences in size and river flow.

2.2.5 *Particle release timing*

Because the seasonal timing of larval release varies with latitude and there is evidence of multiple release periods in some regions (Banas et al., 2009), particle release dates were selected based primarily on published observations of planktonic larvae. These patterns are a function of the water temperatures required for successful development of eggs and larvae (de Rivera et al., 2007, see *Green crab larval biology*). For experiments in Barkley Sound and Willapa Bay, particles were released during spring in April–May and July–August to match observed reproductive patterns of green crabs from those sites (Banas et al., 2009; DiBacco and Therriault, 2015). No data on seasonality of ovigerous females from Sooke Basin are available, but we assumed that because Sooke Basin is between Barkley Sound and Willapa Bay, crabs in this location likely exhibit reproductive seasonality similar to those two sites. Observations from Coos Bay, nearly 500 km south of Willapa Bay, indicate a different reproductive cycle with a spring release that begins in January and continues through April, and a shorter, lower abundance, summer release in August (Shanks et al., 2011), so particle releases were simulated for January–April, and August of each year.

Green crabs preferentially release larvae at high tides and at night which increases dispersal and reduces predation (Zeng and Naylor, 2018). We aimed to maximize the likelihood that particles from a monthly release would be successfully transported out of the embayments (and eventually into the eastern Salish Sea) by timing the releases for the nighttime high tide before the lowest low tide of the month. Our results might therefore overestimate the absolute average probability that a larva from a given site could be successfully transported into the eastern Salish Sea.

2.2.6 *Particle development*

In the present experiments, particles experience a wide range of temperatures as they move from bays to shorelines and are transported up the coast and might experience a temperature range of 2–3° C over the course of their DVM. Because it was computationally intractable to model larval development in a rapidly-changing environment, all particles were considered potentially able to settle after 30 d and for up to 75 d (roughly the minimum and maximum development times observed in the laboratory). This 45-d range of competency was intended to maximize the modeled opportunity for particles to be successfully transported into the eastern Salish Sea.

A particle was considered to have been successfully transported into the eastern Salish Sea if its position during competency was east of an arbitrarily-defined boundary to the eastern Salish Sea: a line extending from Victoria, British Columbia to Port Angeles, Washington (Fig. 1). We evaluated relative support for each of the release locations as potential source populations by comparing the proportions of particles that were successfully transported into the eastern Salish Sea across release dates.

2.3 RESULTS

Across all locations and dates (38 simulated releases totaling 380,000 particles), < 2% of particles were successfully transported into the eastern Salish Sea, supporting the assumption that such advection is likely to be relatively rare. Nevertheless, all four source locations had more than one release date that resulted in successful transport of at least one of the 10,000 particles (Table 2.1).

Table 2.1 Percent of 10,000 released particles successfully transported into eastern Salish Sea organized by date of release (row) and release location (column). Particles were counted as

successful if present in eastern Salish Sea when 30–75 d old. Grey shading = no release. White shading = no successfully transported particles. Light yellow shading = 0–1% success. Yellow shading = 1–10% success. Dark yellow shading = >10% success.

Date	Sooke Basin	Barkley Sound	Willapa Bay	Coos Bay
10 Aug 2014	11.38	4.10	27.46	0.22
27 Jan 2015				0
22 Feb 2015				0
22 Mar 2015				0
19 Apr 2015	0.81	0	0	0
18 May 2015	0.03	0	0	
3 July 2015	0	0	0	
1 Aug 2015	0.09	0.03	0.02	0
17 Jan 2016				0.08
13 Feb 2016				0
12 Mar 2016				0
9 Apr 2016	1.90	0	0	0
8 May 2016	0.68	0	0	
2 July 2016	0	0	0	
2 Aug 2016	0.64	0.01	0.05	20.16
AVERAGE	1.73	0.46	3.06	1.86

2.3.1 *Effect of release location on transport success*

Releases from Sooke Basin resulted in successful transport of at least some of the particles on seven of nine release dates, more frequently than any of the other three sites. On the majority of

these dates, however, the probability of successful transport was extremely low, and, on average, only 1.73% of all particles released from Sooke Basin were predicted to enter the eastern Salish Sea within their competency period. When each site was averaged across all release dates, particles released from Willapa Bay were more likely to enter the eastern Salish Sea than those from the other sites, at an average of 3.06% transport success. Coos Bay had an average transport success of 1.86% comparable to Sooke Basin, and Barkley Sound was the least likely with only 0.46%.

It was possible for a particle to be present in the eastern Salish Sea and not be counted as successfully transported because it was flushed back out to the coastal ocean before it reached competency at 30 d of age. Most particles that reached the eastern Salish Sea remained there and were not subsequently flushed. Due to proximity, particles released from Sooke Basin often reached the eastern Salish Sea within a week, but the percentage of successfully transported particles could ultimately be low if they were then swept by the tidally-averaged westward flow out to the Pacific Ocean before they reached 30 d old.

2.3.2 *Effect of release timing on transport success*

Within each site, there was substantial variability in the proportion of particles that were successfully transported into the eastern Salish Sea depending on the date of release. For every release site, the release date with the greatest probability of successful transport occurred in August, though the year differed depending on site. The northern three release sites were most successful in August 2014, while the southernmost site was most successful in August 2016. For Barkley Sound and Willapa Bay, the two sites of intermediate distance to the eastern Salish Sea,

August was the only month of release in which any of the particles reached that region during their competency period. Coos Bay differed from this trend only in that the release during August 2015 did not result in any particles reaching the eastern Salish Sea, while one in January 2016 did. But this is a month in which first stage zoea are not typically observed in the water column at the more northern sites (see *Particle release timing* in Methods section), so we did not model particle releases in those locations for that date.

2.3.3 *Oceanographic conditions favoring transport success*

To see how dependent particle transport success was on flow reversals, a timeline was made overlaying transport successes from each release experiment with whether the Strait of Juan de Fuca had reversed flow or normal flow at the surface during the dates the particles were active (Figure 2.2). These results supported the hypothesis that flow reversals could contribute to successful transport of larvae into the eastern Salish Sea from the outer coast. That is, for the three coastal source locations, successful transport only occurred following flow reversals, but such reversals were not required for particles released from the sole inland source location, Sooke (Figure 2.2). During some April and May releases, particles released in Sooke Basin were successfully retained in the eastern Salish Sea, albeit at low probabilities, without any coincident flow reversal during the dispersal window. Releases from the other locations during those months did not result in any successful transport of particles to the eastern Salish Sea. Reversal events did not always result in successful transport of particles, however. Even though those released from Coos Bay in January, February and March overlapped with flow reversals, they nevertheless had very low probability of being transported into the eastern Salish Sea, and in some release months no particles from Coos Bay were transported to that region.

2.4 DISCUSSION

Overall, the probability of larvae reaching the eastern Salish Sea from any site appears to have been quite low, even though our experiments were run during years with strong ENSO conditions, which have been observed to be favorable for larval transport and survival (Behrens Yamada and Kosro, 2010). We also observed that successful transport of particles into the eastern Salish Sea could be geographically and seasonally variable.

2.4.1 *Effect of release location on transport success*

Sooke Basin was a potential source of crab larvae for other areas of the Salish Sea, but larvae from Sooke were not as persistent and ubiquitous in the eastern Salish Sea as might be expected based on geographic proximity. Indeed, as discussed above, distance of the source to the eastern Salish Sea by itself was not a strong predictor of probability of transport success. One release event (August 2016) from Coos Bay had a higher rate of transport success than any release from Sooke Basin, contrary to the hypothesis that the closest source is necessarily the most likely source. Sooke Basin is unique among release sites in that particles debouche into the Strait of Juan de Fuca rather than the Pacific Ocean. The Strait of Juan de Fuca has two features that enhance the likelihood of transport success relative to the coastal ocean: a restrictive coastline and high flow variability (Sponaugle et al., 2002). Particles released from Sooke exit into the Strait of Juan de Fuca and are restricted topographically to travel either to the eastern Salish Sea or to the Pacific Ocean. The high flow variability from the tidal currents in the Strait of Juan de Fuca enhances horizontal dispersion of particles so that even when tidally averaged flows would

transport particles to the Pacific Ocean (as during a non-reversed flow regime), some particles can be transported into the eastern Salish Sea.

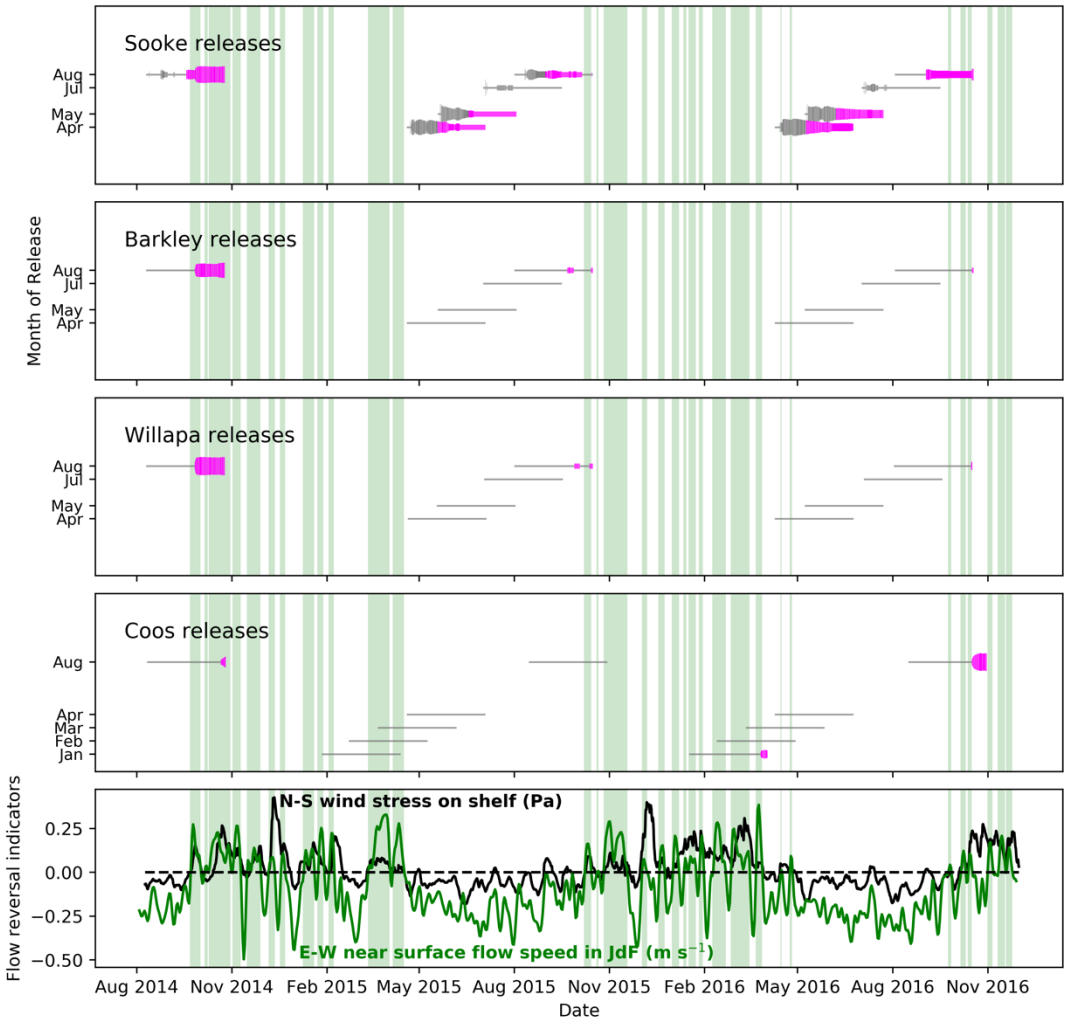

Figure 2.2 Timeline indicating successful transport of larvae into eastern Salish Sea per release overlaid with occurrence of flow reversals (green shading). Bottom subplot shows presence of two flow reversal indicators: wind direction over coastal ocean (black) and flow direction in Strait of Juan de Fuca (green). Release locations separated into subplots. Horizontal lines represent release dates. Number of larvae transported into eastern Salish Sea indicated by line thickness. Line is magenta when larvae meet two conditions: present in eastern Salish Sea and 30–75 d old. Otherwise, line is grey.

Transport success from Willapa Bay and Barkley Sound coincided temporally, despite being on opposite sides of the Strait of Juan de Fuca. During typical flow regimes, the Strait of Juan de Fuca is upstream of Barkley Sound. While there is evidence that some upstream larval dispersal is not uncommon (Gharouni et al., 2017; Pringle et al., 2011; Sponaugle et al., 2012), it was expected that transport success from Barkley Sound would be low and out of phase with transport success from Willapa Bay. This hypothesis was supported in part by the result that transport success from Willapa Bay was consistently greater than transport success from Barkley Sound, but the hypothesis was challenged by the synchrony of success from the two locations.

Transport success from Coos Bay was inconsistent. This could be due to the influence of the Columbia River plume, which (as hypothesized in *Particle release locations*) can block upshelf transport from sites south of the plume if particles are not entrained in the plume (Peterson and Peterson, 2009). Whether particles being transported from the south are blocked by the Columbia River plume or entrained in it may depend on the direction of the plume at the time that particles arrive. Another hypothesis is that since the distance between Coos Bay and the eastern Salish Sea was greater than for the other sites, the stochastic nature of larval dispersal makes successful transport inherently less likely. Regarding the latter, it appeared that time was not the limiting factor, and particles from Coos Bay that did reach the Strait of Juan de Fuca were transported there on timescales similar to particles from the other two coastal sites.

2.4.2 *Effect of release time on transport success*

Seasonal patterns emerged from the results. Broadly speaking, the eastern Salish Sea might be most easily reached by larvae that are present in the water during early fall. August particle releases were the most consistently successful, with transport success into the eastern Salish Sea from every location for every year (except for from Coos Bay in August 2015). Furthermore, the releases that had the greatest fraction of successfully transported particles were August releases. On the other hand, summer was the least likely season for transport success. Particles released in July were never successfully transported into the eastern Salish Sea. Since the wind direction was persistently southward during the releases in April 2015, May 2015–2016, and July 2015–2016, transport success was expected to be consistently low or impossible for those release experiments. This hypothesis was supported by the result that no particles released in April, May or July in Coos, Willapa, and Barkley were successfully transported into the eastern Salish Sea, but challenged by the springtime transport successes from Sooke Basin. This could be explained by the seasonal variation in tidal amplitude in the Strait of Juan de Fuca from a greater tidal range in early summer near the summer solstice to a smaller tidal range in late summer (Mofjeld and Larsen, 1984). A greater tidal range would come with stronger tidal currents, extending the tidal excursion and increasing the horizontal dispersion of particles in the Strait of Juan de Fuca, allowing more particles to be advected into the eastern Salish Sea during westward subtidal flow in the Strait of Juan de Fuca. For the coastal release locations, the improbability of larvae reaching the eastern Salish Sea during spring would be compounded by the spring freshet of the Columbia River plume, a seasonal event that freshens the plume below the salinity threshold for larval survival (as described in *Particle release locations*). During the fall and winter, the only

seasons with transport success of particles from coastal release locations, the Columbia River plume salinity is high enough for larvae to survive (Nash et al., 2009; Bravo et al., 2007).

It had been hypothesized that winter would be a likely season for advection of larvae into the eastern Salish Sea because of southerly winds and the likelihood of flow reversals in the Strait of Juan de Fuca (Behrens Yamada et al., 2017). However, the winter particle releases in Coos Bay during January and February were not successful except for the release in January 2016, suggesting winter is not as likely as previously expected to coincide with arrival of larvae into the eastern Salish Sea.

2.4.3 *Effect of oceanographic conditions on transport success*

Fall and winter particle releases co-occurred with flow reversals, but only one spring release, April 2016, co-occurred with a brief flow reversal (which is typical, as meteorological conditions during spring and summer are less conducive to flow reversals). Within the fall and winter, flow is reversed approximately half the time, with reversals as brief as a few days and as long as a few weeks (Thomson et al., 2007). For green crabs, spring spawns produce more larvae than fall spawns (as described in *Particle release timing*), so there is a mismatch between spawn size and the likelihood of co-occurrence with flow reversals and transport success. This mismatch contributes to the overall low probability of green crabs reaching the eastern Salish Sea.

Flow reversals contributed to transport success differently for each of the release sites. Successful transport from Sooke Basin into the eastern Salish Sea was possible without flow reversals, although flow reversals enhanced transport success. Particles released from Willapa

and Barkley were successfully transported into the eastern Salish Sea during flow reversals, but only when the timing of the flow reversal corresponded to the presence of particles in adjacent waters. By examining particle tracks (Figure 2.3), the synchrony of Willapa Bay and Barkley Sound appears to reflect a lag between the flow reversals and particle releases. When particles were released from Barkley Sound during a southward flow regime, they had a chance to disperse southward before the flow reversed northward. Therefore, it may still be true that coastal larvae enter the Strait of Juan de Fuca from the south during a flow reversal, and it is more likely that larvae entering the Strait of Juan de Fuca from the south were released in the south, but it is not impossible for larvae released in the north to enter from the south.

For Coos Bay, the relationship between flow reversals and transport success was weaker. Even though Coos Bay green crabs spawn later in the year when flow reversals are more common, transport success from Coos Bay was not more likely than from the other sources. This might be because of the great distance between Coos Bay and the eastern Salish Sea, as noted above.

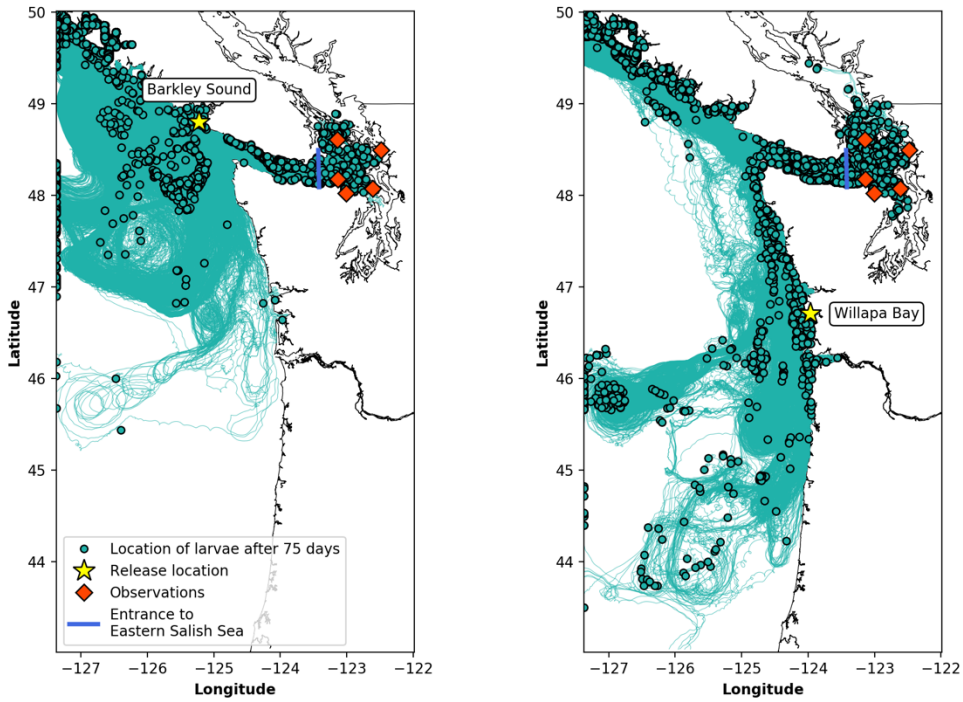

Figure 2.3 August 10, 2014 larval release experiments from Willapa Bay and Barkley Sound. Larvae were successfully transported into the eastern Salish Sea from both release locations.

2.4.4 *Future Directions*

Although results of these particle release experiments revealed viable transport pathways between established green crab populations and the eastern Salish Sea, additional information could further improve our understanding of potential green crab spread in this this region. In particular, the absolute probability of larvae reaching the eastern Salish Sea from any one of the four sites tested here will also be strongly influenced by the size of the adult crab population at the release site. That is, the probability that a given site is a source for green crab larvae entering the eastern Salish Sea is a product both of the likelihood that any individual larva released from that site could be transported there, *and* of the actual number of larvae released from that site. Data to assess relative population densities are not consistently available for the times and

locations assayed here, but we can draw some general conclusions. For one, Willapa Bay, despite showing a relatively high potential for transport success for larval releases from 2014–2016, had extremely low densities of adult green crabs during those years, indeed below detection limits in 2014 (Behrens Yamada et al., 2013). Thus, the overall chance that Willapa Bay was a source population is quite low. By contrast, periodic monitoring in Sooke Basin and Barkley Sound indicates that those populations are typically much larger than either Coos or Willapa Bays, presumably increasing the likelihood that those sites, rather than the southern sites, could act as a source relative to model results. Similarly, there is uncertainty in the modeled probabilities of successful recruitment from all four sources because only a handful of potential release periods were evaluated.

There are also a few open questions that arise from restrictions in the model domain that could be addressed in future investigations. The model domain prevented us examining the possibility that green crab larvae can be advected into the eastern Salish Sea from the north, through Johnstone Strait, or from populations in California. The first scenario is considered unlikely because transport through Johnstone Strait is one-fifteenth of the magnitude of transport through the Strait of Juan de Fuca (Thomson, 1981). We attempted to account for the possibility of larvae arriving from California by modeling particle release from Coos Bay, the closest population to the southern model extent.

Another source of uncertainty inherent in the model is that it does not resolve exchange flow in sites where female green crabs release larvae. Because smaller rivers were not included in the model, particles were transported out of embayments by tidal currents alone and not exchange

flow. The impact of exchange dynamics within embayments on large scale connectivity is an open question and would also be a good topic for future study.

2.5 CONCLUSIONS

The main conclusion is that green crab larvae released in any of the source locations tested in this study could be transported into the eastern Salish Sea, but only infrequently. This connectivity influences the potential for unassisted (by humans) regional spread of green crabs (Pineda et al., 2007). In addition, larvae from Sooke Basin are apparently not substantially more likely to be advected into the eastern Salish Sea than larvae from populations on the Pacific Coast, possibly affording some protection for inland shorelines from further range expansion by this relatively dense population. Understanding sources, connectivity, and pathways of spread (Hulme 2009) can inform ongoing trans-boundary management efforts between the United States and Canada. Two potential strategies include targeting likely source populations for eradication and control and focusing early detection and control efforts during years with oceanographic conditions favorable to dispersal. These findings also help explain why green crabs apparently did not expand their range into the Salish Sea (excepting Sooke) prior to 2016: the overall low probability of transport into the Salish Sea from any of the potential sources observed here, combined with the fact that ENSO events, and associated warm waters, were much weaker between 1999 and 2014, likely did not provide sufficient opportunity for advection of larvae. Lastly, global climate change is predicted to increase the frequency and intensity of ENSO events (Cai et al., 2015) which, based on prior research (Behrens Yamada and Kosro, 2010) and the present model results, indicates greater likelihood of successful transport of green crab larvae into the eastern Salish Sea. In the face of more frequent or more intense ENSO events, the Strait

of Juan de Fuca might pose less of a barrier to further introductions of green crabs or other non-indigenous species.

Chapter 3. THE SHELF SOURCE OF ESTUARINE INFLOW AND ITS CONSEQUENCES FOR RIVER PLUME SHAPE

3.1 INTRODUCTION

Buoyancy-driven flows arise from gravity acting on density gradients that arise, for example, from a source of fresh water flowing into a large reservoir of sea water. The classic example of buoyancy-driven flow is in estuarine circulation (MacCready and Geyer 2010; Geyer and MacCready 2014). Estuaries are constricted regions where a river meets and mixes with ocean water. This transition can happen abruptly to form a sharp gradient, as is the case with salt wedge estuaries like the Fraser River, or it can happen gradually over tens or hundreds of kilometers, as is the case with partially-mixed estuaries like Chesapeake Bay. The mixed water that forms in the estuary is composed of the river water and a significant amount of ocean water that originates on the shelf. Much has been written about the path by which mixed water leaves the estuary as a river plume (Horner-Devine et al., 2015). Here, we focus on the path by which dense ocean water is drawn into the estuary from the shelf.

Estuarine inflow plays a number of roles in estuarine and shelf ecology. As shelf water is drawn into the estuary, it flushes the resident estuarine water. Duxbury (1979) hypothesized that variability in the density of shelf water (variability that is driven by upwelling) accelerates exchange flow by increasing the density gradient across an estuary, supported by observations of residence time within Grays Harbor, Washington, USA. Shelf inflow was found to be an important controller of residence time in a box model of the Strait of Georgia while variability in Fraser River run off had little impact on residence time (Pawlowicz et al., 2006). Banas et al.

(2004) also found a low correlation between river flow and salt transport in Willapa Bay off the Oregon coast, showing that a hundred-fold increase in river flow only increased salt transport by a factor of three; further, ocean water propagated into the bay even during low- and no-flow conditions because of lateral tidal stirring.

Inflowing water can have a large impact on the biogeochemical characteristics of estuaries. Inflow to the Salish Sea, for example, is episodically found to originate from the deep abyssal Pacific and have high nitrate but low oxygen, aragonite saturation, and pH. One path into the Salish Sea via the Strait of Juan de Fuca has been observed in the Juan de Fuca canyon during upwelling-favorable winds, which enables water from below the shelf break to reach the Salish Sea (Alford and MacCready, 2014). This hypoxic deep-water signature is visible throughout the Salish Sea and in the Puget Sound (Feeley et al., 2010). A comprehensive numerical model of the Pacific northwest coastal waters has shown the importance of exchange flow on nutrient availability on the shelf. Ninety-eight percent of the available nutrients in the outflow of the Strait of Juan de Fuca originated in the ocean, brought into the fjord-like estuary as inflow and upwelled to the surface through mixing processes (Davis et al., 2014). There has also been evidence that exchange flow in estuaries plays a major role in transport of nutrients on continental shelves. A three-dimensional model study of the Columbia River plume noted the influence of estuarine exchange flow on cross-shelf exchange: 25% more water was exchanged across the shelf when flow from the Columbia River was included in the model (Banas et al., 2009).

As is standard for ocean physics, the dynamic solution to the estuary inflow problem is different when the relevant length and time scales are large enough that planetary rotation can be felt. Here we focus on large-scale estuaries whose plumes form approximately geostrophic coastal currents after tidal averaging. A large-scale estuary can be defined by the ratio of river plume width to the internal Rossby radius of deformation, defined as the Kelvin number. The Kelvin number is $K = fW/\sqrt{g'h}$, where f is the Coriolis parameter, W is the width of the estuary mouth, and $\sqrt{g'h}$ is the maximum internal wave speed given by the reduced gravity, $g' = g(\rho_{in} - \rho_{out})/\rho_0$ assuming a two-layer stratification, and depth, h, of the buoyant plume. A river plume with small K is governed by nonlinear advection; a river plume with large K is governed by planetary rotation (Garvine, 1995). Large K estuaries are the subject of most of the prior literature on estuarine inflow (described below) because the dominant geostrophic dynamics can be represented with linear equations. Larger estuaries will have a greater impact on shelf circulation because larger volumes of water need to be transported across the shelf.

Prior work to find the sources of estuarine inflow on the shelf sought analytical solutions in the form of the arrested topographic wave (Csanady, 1978) using simplifying assumptions (Beardsley and Hart, 1978; Masse, 1990). One such assumption is that the estuary has large K such that geostrophic balance dominates and nonlinear terms in the equations of motion can be neglected. Inflow and outflow are assumed to happen in a two-layer flow. Interfacial stress modifies flow in the upper layer and bottom stress modifies flow in the lower layer, but entrainment across the layers is neglected. Exchange flow within the estuary is treated as a boundary condition at the coastline where water is removed from the shelf at a point or finite width mouth. Layer models suggested the estuarine inflow is sourced from the right of the

estuary mouth in the Northern hemisphere. In the region of the shelf where inflow is sourced, streamlines were almost parallel to isobaths, approaching the estuarine channel at a gentle onshore angle. The flow turns onshore sharply near the mouth so that inflow enters the estuary perpendicular to the coastline (Beardsley and Hart, 1978; Masse, 1990). These thirty-year-old analytical models comprise our current theoretical understanding of estuarine inflow.

Ocean modeling has advanced in the last thirty years such that the estuary inflow problem can be approached in a sophisticated way using primitive equation models. These models can resolve ageostrophic dynamics, vertical variation in transport, and interactions between inflowing and outflowing currents. Vertical resolution has been found to enable or enhance exchange flow on the shelf, even in unstratified water, because of Ekman transport in boundary layers (Gawarkiewicz and Chapman, 1991; Ekman, 1905). Although a large K estuary is expected to produce predominantly geostrophic shelf flow, using a primitive equation model resolves ageostrophic tidal dynamics near the estuary mouth and allow for mixing outside of the estuarine channel. Interactions between inflow and outflow likely occur if, as the analytical models predicted, the inflowing current occurs roughly beneath the outflowing current. Vertical shear would increase where the opposing currents overlie each other.

This study will use a three-dimensional model with a simple set up to foreground the shelf circulation features that can be connected to density-driven exchange flow within an abutting estuarine channel. First, the source of inflow will be examined using particle tracking and volume transport. These results will be compared qualitatively with results from previous analytical models. Next, the dynamics of the system will be examined using momentum budgets

following the inflowing particles to evaluate the dynamic assumptions in the previous work. Finally, an idealized theory will be laid out for how an inflowing current beneath a river plume can alter the position and shape of the river plume.

3.2 METHOD

To investigate the sources of inflow to an estuary, a model of an idealized estuary was built using the Regional Ocean Modeling Systems (ROMS). ROMS solves the three-dimensional Reynolds-averaged Navier-Stokes equations on a stretched vertical coordinate grid (Shchepetkin and McWilliams, 2005). The model used in this study is based on that designed in MacCready et al. (2018) and features a river flowing out onto an unstratified shelf (shelf salinity 31 g kg^{-1}) that was linearly sloped (slope of 1 m per 1 km offshore distance). The river channel is v-shaped and widens and deepens toward the mouth (Figure 3.1). The horizontal grid resolution was highest near the estuary mouth, with a grid cell length of 500 m. Horizontal resolution increased telescopically from the mouth to 2.5 km near the model edges. The vertical grid had 30 levels that stretch to accommodate bathymetry. Fresh water flowed in through the river channel at a constant rate of 1500 m^3 s^{-1}. Boundary conditions at the three open ocean boundaries (offshore, upstream, and downstream) follow Chapman (1985) for the surface elevation and Flather (1976) for momentum terms. The model used a single-frequency, 12-hour tidal forcing. Vertical mixing was modeled using the k–ϵ turbulence closure parameters in the general length scale options (Umlauf and Burchard, 2003). There were no shelf currents or winds. This simplified forcing scheme was used as a starting point to isolate the processes drawing shelf water into the estuary. The model was run for 120 days. All time averages presented in the results are taken from day 50 until the end of the model run.

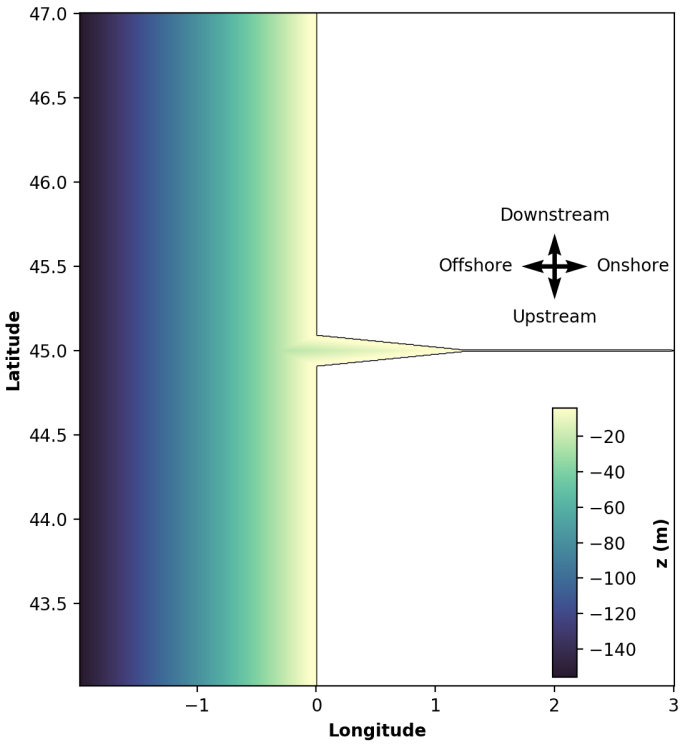

Figure 3.1 Model domain, bathymetry, and direction definitions.

When describing results, the terms “downstream” and “upstream” will be used to refer to the direction of coastal trapped wave phase propagation. For example, the buoyant plume forms a coastal current downstream of the estuarine channel. Inflow is expected to be drawn from downstream of the channel, so to reach the channel it must travel in the upstream direction.

To identify the estuary-bound current on the shelf, particle tracking and integrated volume transport perspectives are used. That is, inflow is depicted in one analysis as streamlines and in the second analysis as the volume of flow across a cross section.

3.2.1 *Particle tracking analysis*

In the first analysis, particles were released onto the shelf and passively advected by the shelf currents. Their paths were tracked, and the tracks were filtered by whether the particles reached water with salinity fresher than 20 g kg^{-1}. This salinity is only present within the estuarine channel, therefore indicating a particle was advected from its start position on the shelf into the channel and underwent mixing. This approach resolves time and direction of flow but does not include the volume of flow along each path; all flow paths are displayed with equal significance. Particle tracking was implemented as an offline model that utilized the output of the ocean model. Particle positions were advected using bi-linear interpolation of three-dimensional velocity fields in the hourly ocean model output. The integration methods are similar to those used in previous studies (Banas et al. 2009; Giddings et al. 2014; Brasseale et al. 2019). Tracks were calculated by forward integration in time (with a 300-second time step to resolve tides) using 4^{th}-order Runge-Kutta integration. Particles were dispersed vertically according to a random walk model developed by Visser (1997) to simulate the effect of vertical turbulent mixing.

The particles were released into the model after the spin up period and were tracked for a 75-day period. 12000 particles were released, distributed across 1200 latitude-longitude pairs and 10 depths that were spaced evenly throughout the water column. This was done to ensure that boundary layers were resolved at all locations but results in a higher vertical density of particle releases in the shallower water near the coast.

3.2.2 *Particle track momentum balances*

The particle tracks demonstrate where inflow originated from, but the tracks alone do not reveal why inflow originated from those regions on the shelf. To understand what drives inflow toward the estuary, a momentum budget is calculated for each inflowing particle at each step along its path. This is done using ROMS diagnostic output, using saved terms in the Navier-Stokes equations which ROMS calculates to update the modelled flow field. ROMS uses the hydrostatic approximation, and mixing from horizontal shear is neglected.

x-direction momentum:

$$\frac{\partial u}{\partial t} + u\frac{\partial u}{\partial x} + v\frac{\partial u}{\partial y} + w\frac{\partial u}{\partial z} - fv = -\frac{1}{\rho_0}\frac{\partial p}{\partial x} - \frac{\partial}{\partial z}\left(\kappa\frac{\partial u}{\partial z}\right) \qquad \text{(Chapter 3. 1)}$$

ROMS diagnostics: *u_accel, u_xadv, u_yadv, u_vadv, u_cor, u_prsgrd, u_vvisc*

y-direction momentum:

$$\frac{\partial v}{\partial t} + u\frac{\partial v}{\partial x} + v\frac{\partial v}{\partial y} + w\frac{\partial v}{\partial z} + fu = -\frac{1}{\rho_0}\frac{\partial p}{\partial y} - \frac{\partial}{\partial z}\left(\kappa\frac{\partial v}{\partial z}\right) \qquad \text{(Chapter 3. 2)}$$

ROMS diagnostics: *v_accel, v_xadv, v_yadv, v_vadv, v_cor, v_prsgrd, v_vvisc*

where *u*, *v*, and *w* are the *x*-, *y*-, and *z*-directional velocities respectively; *f* is the Coriolis parameter; ρ_0 is the background density; *p* is the hydrostatic pressure; and κ is the eddy diffusivity. ROMS outputs diagnostic terms at a time step halfway between each output of the flow field and the particle output. To generate a history of forcing experienced by the particle, the forcing variables from the diagnostic output at the particle's location are averaged from the output file prior to and the output file previous to the particle's time stamp.

The momentum equations were translated into a Lagrangian reference frame and rotated into a streamwise-normal (*s*-*n*) coordinate system, following the *s*-*n* coordinate momentum balances of Hench and Luettich (2003) and McCabe et al. (2009). The rotation to an *s*-*n* coordinate system is appropriate because the particle paths are curved, and the dynamic balances are better understood as being along or perpendicular to particle motion. The translation of the equations from an Eulerian to Lagrangian reference frame was done by adding local acceleration to the advective terms to form the material derivative of velocity with respect to time. The *s*-*n* coordinate system is defined for each particle such that the streamwise direction, *s*, is directed along the track the particle is travelling and the normal coordinate, *n*, is perpendicular to the particle track everywhere. The velocity in the streamwise direction, u_s, is the speed at which the particle is traveling and the velocity in the normal direction, u_n, is zero by definition. A variable θ is defined as the angle between the *x*-*y* coordinate system and the *s*-*n* coordinate system. The vertical coordinate, *z*, is unchanged. After translation and rotation, the momentum equations in the *s*-*n* coordinate system are:

s-direction momentum:

$$\frac{Du_s}{Dt} = -\frac{1}{\rho_0}\frac{\partial p}{\partial s} - \frac{\partial}{\partial z}\left(\kappa\frac{\partial u_s}{\partial z}\right) \qquad \text{(Chapter 3.3)}$$

n-direction momentum:

$$u_s\frac{D\theta}{Dt} + fu_s = -\frac{1}{\rho_0}\frac{\partial p}{\partial n} - \kappa\frac{\partial u_s}{\partial z}\frac{\partial \theta}{\partial z} \qquad \text{(Chapter 3.4)}$$

The terms in the *s*-direction momentum equation are the streamwise acceleration, the streamwise pressure gradient, and friction arising from vertical divergence of streamwise stress. The terms in the *n*-direction momentum equation are the change in particle direction, the Coriolis force, the stream-normal pressure gradient, and friction. For more information about the derivation of the *s*-*n* coordinate momentum equations, see previous work in the appendix of Hench and Luettich (2003) for the derivation and McCabe et al. (2009) for a vertically-resolved generalization.

After the time series of momentum terms were extracted from the model output for each particle's track, including the terms in Eqs. (Chapter 3.3) and (Chapter 3.4) and the particle position, were tidally averaged using a Godin filter (Godin, 1972) before being rotated into the *s*-*n* coordinate system for each step of each particle's time series. The streamwise direction relative to the *x*-*y* coordinate system, θ, was inferred from the direction of the Coriolis force vector, which is always stream-normal. To compare a diversity of curving particle tracks, the momentum series were plotted with particle positions normalized by their streamwise distance from a reference point at the channel mouth. That is, the x-axis in figures is generated by unraveling the curved particle tracks and lining up their end points at a reference location in the channel mouth.

3.2.3 *Transport analysis*

To complement the particle tracking analysis, inflow is analyzed as transport of the volume of shelf water towards the estuary. Transport calculations give a more accurate picture of the relative importance of flow paths and can be used to form closed transport budgets. Transport calculations were performed using the Total Exchange Flow method (TEF, MacCready, 2011),

which was developed to translate flow fields in estuaries into a framework based on the Knudsen relations (Knudsen, 1900; translated in the appendix of Burchard et al., 2018). That is, TEF assumes flow at a cross section of an estuary, no matter how complex, can be deconstructed into a two-layered flow: a salty layer transporting salt up-estuary, and a fresher layer of mixed water transporting salt out of the estuary. This is done by calculating transport in salinity classes and determining a "dividing salinity" (MacCready et al., 2018; Lorenz et al., 2019) to separate water masses responsible for up-estuary salt flux from down-estuary salt flux. We extend this assumption to the shelf. A shelf with an abutting estuary can be assumed to have two fundamental water masses: dense shelf water transporting salt towards the estuary, and buoyant plume water travelling away from the estuary. Transport is estimated across several cross-sections through the estuary and on the shelf. On the shelf, the cross sections are drawn as boxes centered on the estuary such that TEF transports are evaluated using salt flux into and out of the box in analogy to salt flux up-estuary and down-estuary. Flow is sorted on the three sides of the shelf box using a single dividing salinity for each box. To help answer the motivating question of where inflow originates, horizontal resolution is maintained through the transport calculation. The resulting flow vectors represent transport across the columns of grid cells at the perimeters of the shelf boxes. Note that the grid cells have different widths, since there is higher resolution near the mouth.

3.3 RESULTS

As a brief overview, the main results are as follows. The greatest source of the estuarine inflow in the model was from downstream on the shelf. Inflow from this region forms a current beneath the plume-shelf interface and travels along trajectories consistent with previous studies. However, the resemblance to previous studies only holds far from the channel mouth. As

inflowing particles approach the channel mouth, the river plume bulge diverts particle paths from predicted paths. Inflow sources were also found in the plume and in shelf water upstream of estuarine channel. Inflowing particles originated at all depths, but preferentially travelled through the middle of the water column. These results are shown in more detail below.

For the simulations used here, exchange within the estuary was typical of a partially-mixed estuary in the Geyer and MacCready (2014) parameter space, with a freshwater Froude number of 8.2×10^{-3} and a mixing parameter of 0.74. The outflow flowed out onto the shelf in a buoyant plume and traveled downstream from the channel (Figure 3.2a). Exchange flow began on the shelf as the plume nose arrived (inflow across the shelf box in Figure 3.3 becomes nonzero at the same time that outflow does, which is around Day 30. Notice in the middle panel of Figure 3.2a that on Day 30 the plume nose had just crossed latitude 45.5, where the downstream edge of the shelf box in Figure 3.3 was drawn). Magnitudes of time-averaged transport of shelf water and mixed plume water were calculated across a series of cross sections in the channel and across boxes drawn on the shelf (Figure 3.4). The net transport across all cross sections was 1500 m^3 s^{-1}, which is required for mass conservation of the river input of 1500 m^3 s^{-1} into the model. The magnitudes of transport of dense water into and buoyant water out of the cross sections increased with distance from the freshwater source (Figure 3.4b). Transport magnitudes increased monotonically in the estuary, as was seen in earlier model simulations (MacCready 2011). We also find that transport continues to increase monotonically on the shelf.

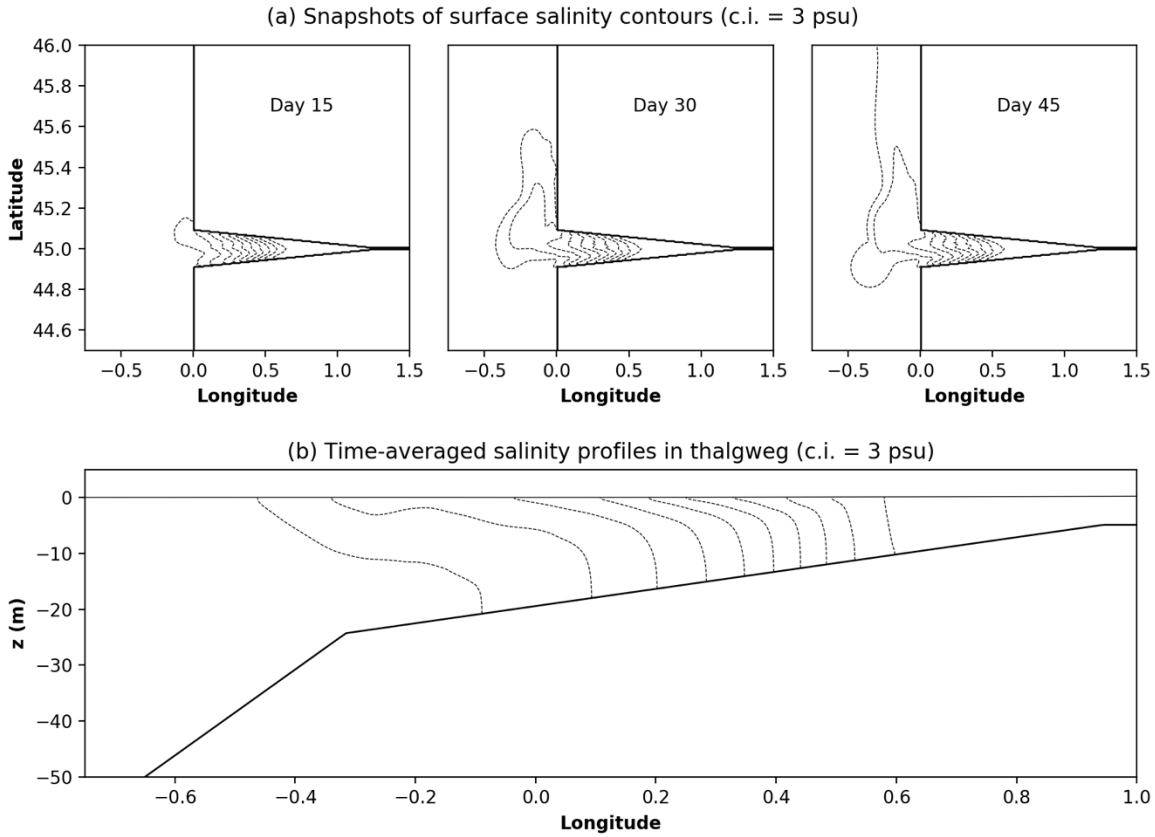

Figure 3.2 Salinity distribution in the model, (a) shown in plan view at three times during spin up, and (b) the time-averaged contours of salinity in profile at a cross-section along the thalweg of the channel.

TEF transport on the shelf demonstrates that exchange flow is occurring outside the estuarine channel. Although exchange flow is traditionally thought of as an estuarine phenomenon (MacCready and Geyer, 2010), the schematic of exchange flow can be extended to include exchange that occurs outside the estuarine channel. Prior work has been done to bridge the gap between estuarine processes and plume properties by focusing on mixing in the near field region (Cole and Hetland, 2016). Following the line of reasoning from the results here, there is a continuity in the dynamics of the plume and the dynamics estuary. TEF does not distinguish between estuary-bound shelf water and plume-bound shelf water.

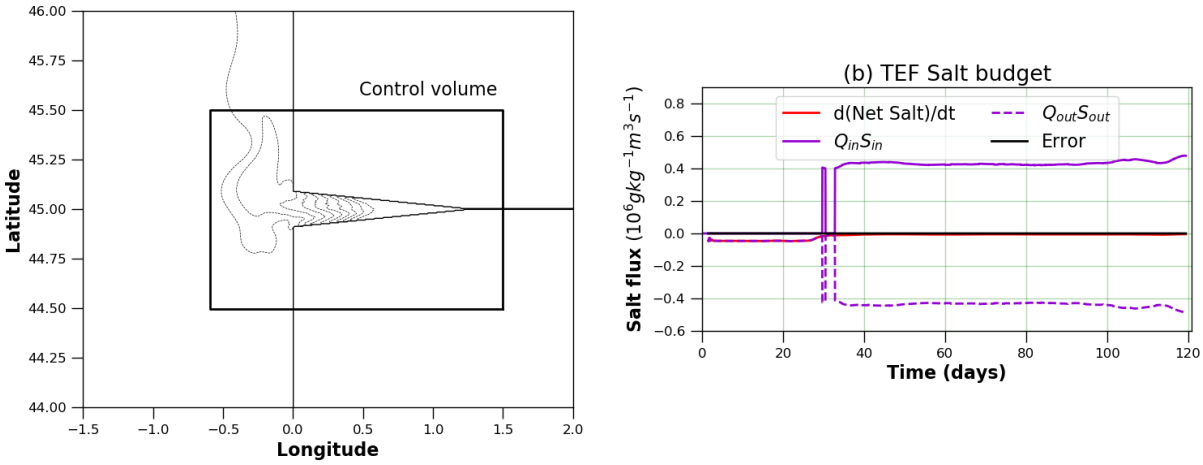

Figure 3.3 Salinity fluxes within a control volume, (a) depicted by a box around the time-averaged surface salinity, and (b) a plot of evolution in time of transport of salinity into the volume ($Q_{in}S_{in}$), transport of salinity out of the volume ($Q_{out}S_{out}$), the change in salt within the control volume (*d(Net Salt)/dt*), and the error.

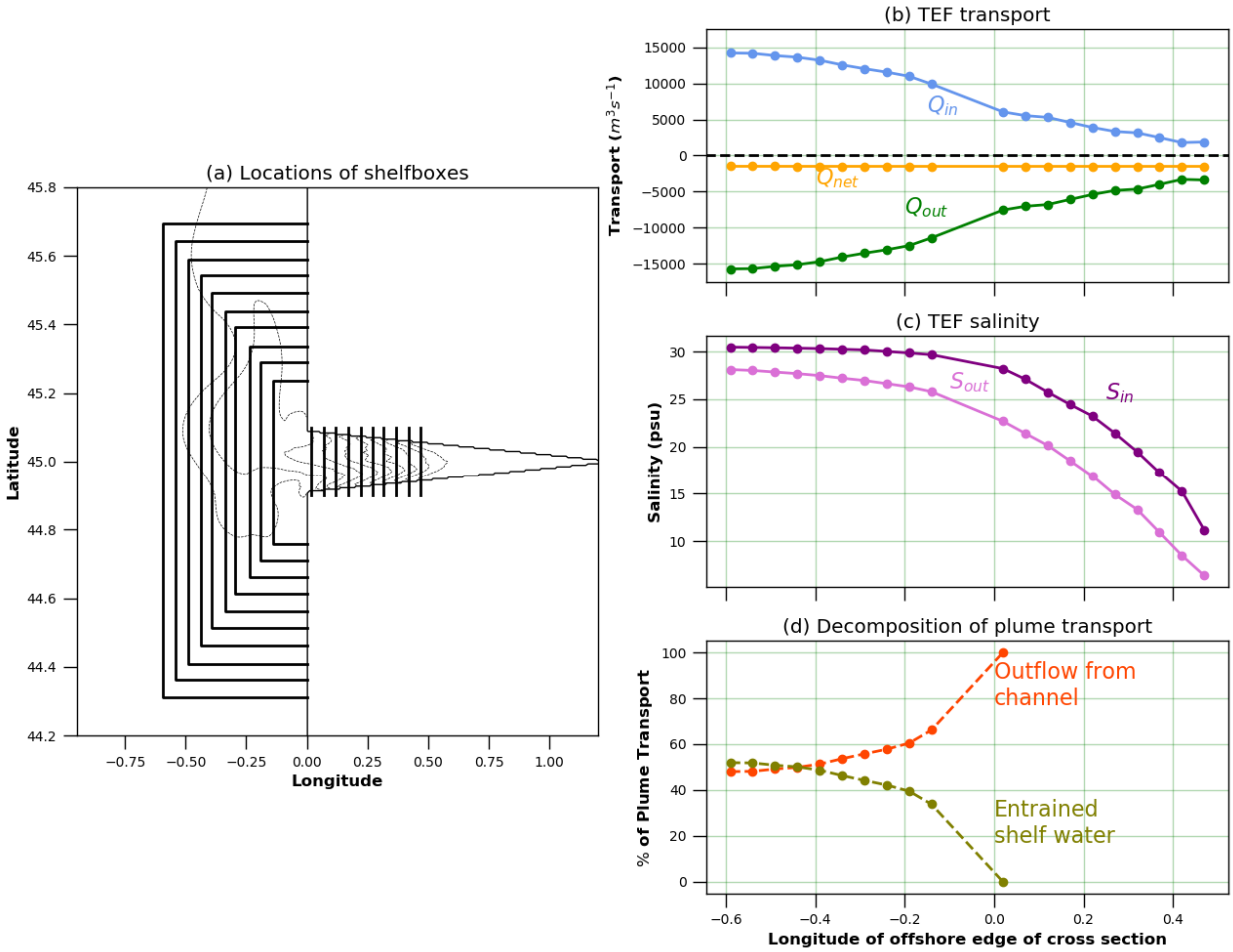

Figure 3.4 Time-averaged TEF quantities calculated in the estuarine channel and on the shelf. (a) The locations of the shelf boxes and estuary sections with the time-averaged surface salinity (contoured as in Figs. 2 and 3a). (b) The volume transports into, out of, and the net transport across each shelf box or estuary section. (c) The flux-weighted salinity of flow into and out of each shelf box or estuary section. (d) How much plume water originated in estuary vs. shelf entrainment.

3.3.1 *Inflow paths*

Both particle tracking and TEF results suggest three separable sources of estuarine inflow. The first source is downstream of the estuary along the offshore edge of the plume (green paths in Figure 3.5) which will be referred to as “downstream shelf” inflow. These downstream shelf

particles follow a path consistent with that described in the previous literature (Beardsley and Hart, 1987; Masse, 1990). From their origin downstream of the estuary, the particles take a straight path at a gentle upslope angle relative to isobaths. When these particles reach the bulge, they take a sharp turn left towards the estuarine channel. The other two sources of inflow were not demonstrated in previous literature about estuarine inflow (Beardsley and Hart, 1987; Masse, 1990). The first of these sources will be referred to as "plume backwash" (yellow in Figure 3.5); that is, water from the plume that retreats back into the estuary. We term the second new source "upstream shelf" water because it is found upstream of the channel (pink in Figure 3.5). Upstream shelf water is entrained by time-dependent wobbling of the bulge. TEF across shelf boxes of different sizes gives a similar result (Figure 3.6b). At the largest shelf box, all inflow and all outflow pass through the downstream edge. As boxes are drawn closer to the mouth, inflow appears across all sides of the shelf boxes (Figure 3.6b). This is evidence of multi-directional inflow paths near the channel mouth.

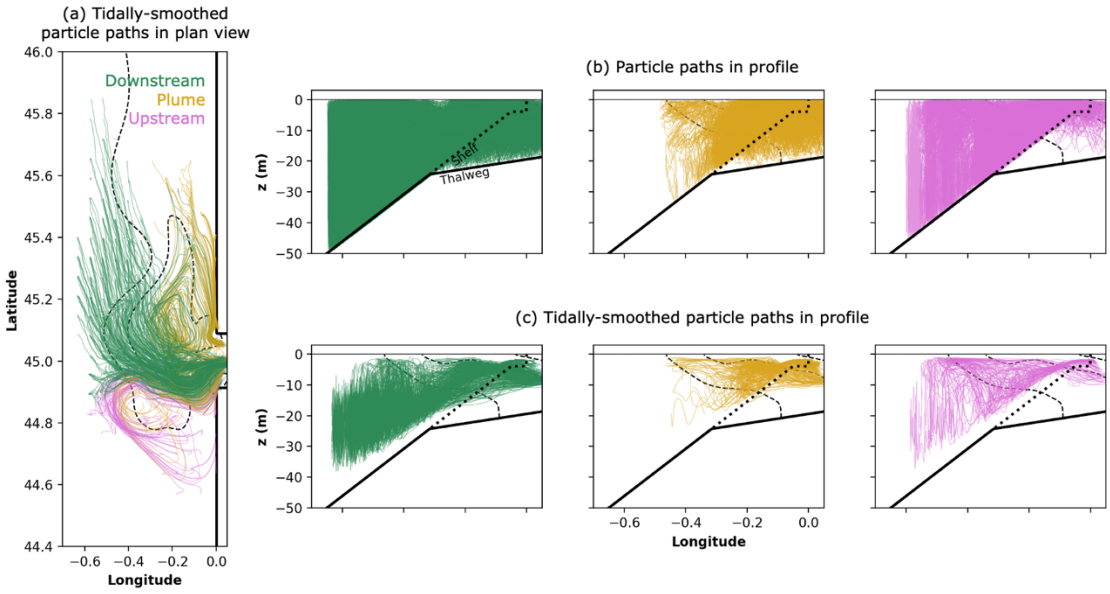

Figure 3.5 Inflowing particle paths plotted (a) in plan view after tidal smoothing, and in profile (b) before and (c) after tidal smoothing. Particle paths are separated into three groups by color

as described in text. Time-averaged salinity is contoured as in previous figures.

The plume backwash and upstream shelf water source less of the total estuarine inflow than the water sourced from the downstream shelf path but quantifying their relative importance from particle tracking and TEF produces different results, because TEF is an Eulerian calculation and particle tracks are Lagrangian. Counting up the particle tracks, 48.8% originated as shelf water downstream of the estuarine channel, 40.7% originated in the plume, and 10.5% originated upstream of the channel. While a plurality of particles originated downstream, the downstream shelf water path accounted for under half of all particles that made it to the estuary. However, these estimates may be biased towards the shallower inflow sources (i.e. plume backwash) because of the higher density of particles released in shallow water (see *Methods*). The relative significance of each source should be addressed with TEF. The plume backwash is sorted by TEF by salinity as part of the relatively fresh water mass primarily exporting salt out of the estuary. Therefore, plume backwash can be identified at a cross section at the estuary mouth as all of the fresher water transported into the estuary (rather than out of the estuary). Considering all water transported into the estuary mouth, 10% was fresher mixed water that shares the salinity of plume water. A different technique must be used to quantify the upstream inflow because it is not distinguished from the downstream inflow by salinity. In the particle tracks, upstream water appears to join the downstream water within the bulge (Figure 3.5). Upstream shelf water is identifiable only by the fact that it originates upstream of the channel. In order to distinguish the two, a TEF cross section is taken across the model at latitude 44.85, just upstream of the southern edge of the channel mouth (not shown). The net transport of shelf water across that cross section was only 86 m^3/s, accounting for less than 1% of the total inflow. The calculation of TEF at this

section offers a lower estimate of the significance of plume backwash and upstream inflow than what was suggested by the particle tracking analysis. The difference between these calculations is owing to the fact that the properties of particles can change along their path through mixing, an inherent difference in Eulerian and Lagrangian approaches. Both analyses agree on the following points: three paths are present; the downstream shelf path accounts for the greatest portion of inflow; backwash from the plume accounts for the second greatest portion of inflow; and water upstream of the channel accounts for the smallest fraction of inflow.

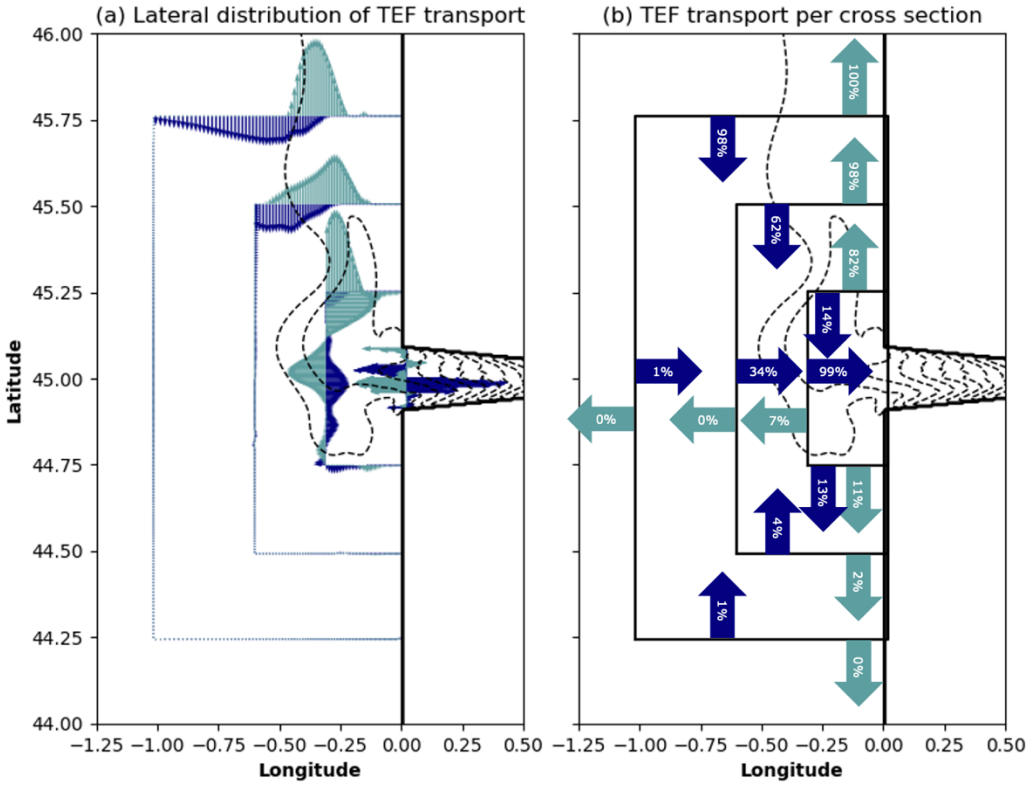

Figure 3.6 Time averaged TEF transport visualized (a) laterally as vertically-integrated mixed water transport vectors (light blue) and shelf water transport vectors (dark blue) for each column of grid cells at the perimeter of three shelf boxes. Note the grid cells are narrower near the mouth. (b) The percentage of the transport of mixed water out of and shelf water into a shelf box that each side accounts for, such that the sides of each box add to 100%. Time-averaged surface salinity is contoured as in previous figures.

3.3.2 *Inflow depth*

Inflow originated from all depths of the water column, consistent with expectations for an unstratified shelf. This was seen in the particle tracking analysis, as particles that were drawn into the estuary from the shelf occupied all depths before tidal averaging (Figure 3.5b). This differs when the particle tracks were tidally smoothed using a Godin filter. After tidal smoothing, a preference emerged for mid-depths. Further, even though particle tracks occupied the bottom boundary layer before tidal smoothing, no tracks appeared in the bottom boundary layer after tidal smoothing (Figure 3.5c). This is because vertical shear in boundary layers induces vertical mixing, so the particles cannot reside in the boundary layers for very long. Inflowing currents were fastest beneath the tilted isopycnals of the plume-shelf interface (Figure 3.7). Even at its fastest, the inflowing current was slower than the outflowing current of the river plume, averaging between 1 and 2 cm/s compared with the plume velocity which exceeded 15 cm/s.

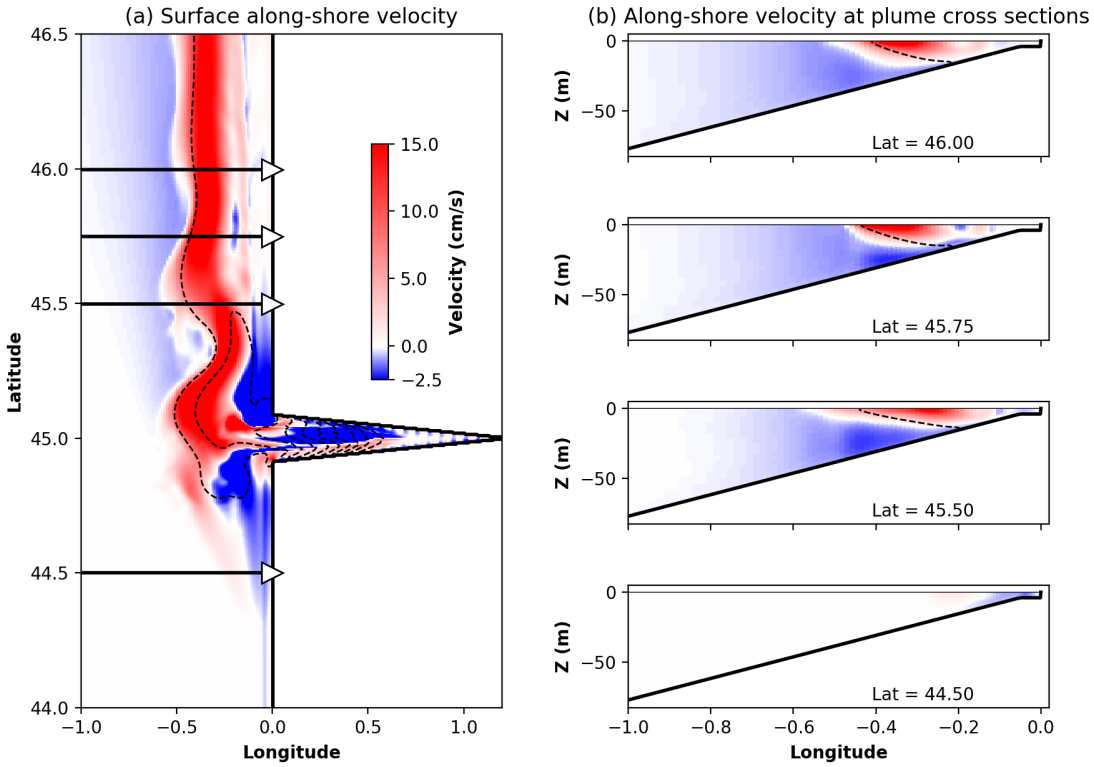

Figure 3.7 Time-averaged along-shore velocity field. (a) Surface N-S velocity plotted in plan view. (b) Cross sections plotted at four latitudes: three through the plume (45.5, 45.75, and 46.0), and one on the upstream side of the shelf as a control (44.5), with locations of cross sections indicated on (a) with arrows. Salinity is contoured as in previous figures.

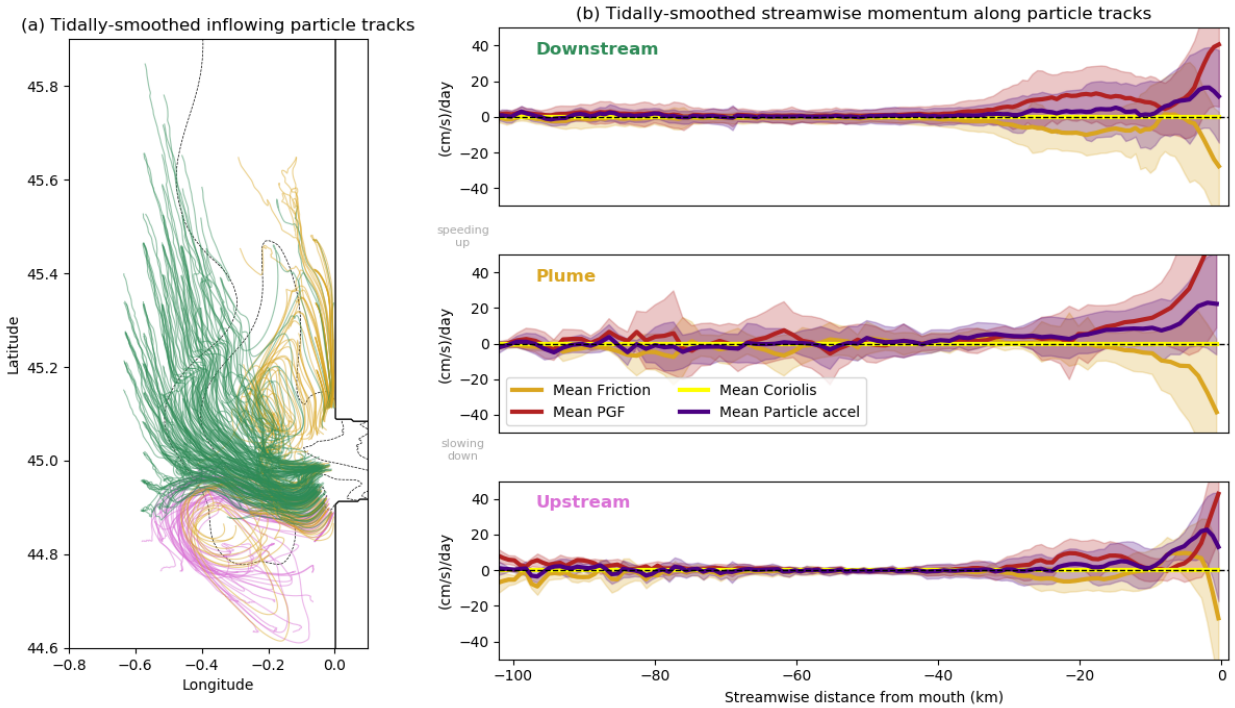

Figure 3.8 The momentum balance in the streamwise direction for each of the three particle groups. (a) Three groups of particle tracks plotted with surface salinity contours (contoured as in previous figures). (b) Momentum acting along the particles' trajectories within each group, binned by streamwise distance from the mouth. The heavy line is the average value at that distance from the mouth and the shading depicts +/- 1 standard deviation. The vertical lines in (b) correspond to the circles drawn on (a).

3.4 Discussion

3.4.1 *Inflow paths: interpretation and importance*

The balance of forces on all inflow paths is mostly geostrophic. This is found by constructing momentum budgets along the particle paths (detailed in *Methods* section). The particle tracks were separated by the three sources of inflow identified above (downstream shelf, plume, or upstream shelf; Figure 3.5) and their momentum values were binned by their streamwise distance from the channel mouth. This way, we find the average momentum balance experienced by particles along the three broadly defined inflow paths as they approach the channel mouth

(Figure 3.8 and Figure 3.9). The standard deviation of the values found in each bin demonstrates the extent to which the mean represents the range of particle experiences within an inflow path.

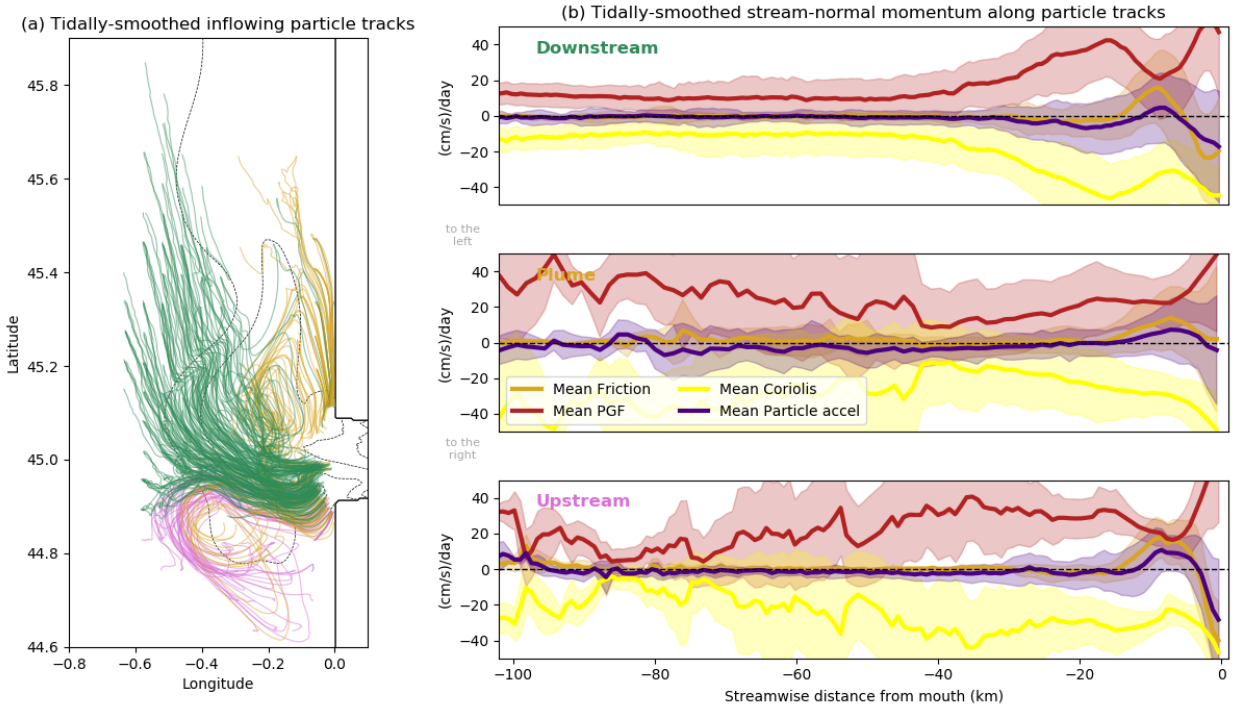

Figure 3.9 Same as Figure 3.8, but for stream-normal momentum.

Geostrophic balance appears in the stream-normal momentum balance (Figure 3.9). The magnitudes of the pressure gradient force and Coriolis increase as the particles approach the channel, demonstrating an acceleration of the geostrophic current beginning at the bulge and continuing to the channel mouth. Geostrophic balance dominates the momentum budget everywhere; the three flow paths are primarily driven, then, by three different pressure gradients that arise in the system. The downstream inflow is driven by the pressure gradients from sea surface tilt and density front tilt around the offshore edge of the plume. The inflow that originates within the plume is driven at the onshore edge of the plume, where a sea surface height low forms in the center of curvature of the outflowing plume as it turns to the right to

travel up the coast. The inflow that originates upstream on the shelf is drawn in by a meandering sea surface height anomaly found in the wobbling bulge. All of these inflow paths travel towards the estuarine channel because geostrophic currents are spun up by these stream-normal pressure gradients.

Streamwise dynamics are negligible until inflow gets within 30 km of the mouth. This region seems to correspond to the "near field region" designated in Horner-Devine et al. (2015) between the river mouth and the bulge where increased turbulence occurs as the plume lifts off from the seafloor and shoals rapidly. In this near field region, all inflow paths experience heightened friction (orange line in Figure 3.8b and Figure 3.9b), consistent with the description of high turbulence between inflow and the plume in the near field region (Horner-Devine et al., 2015) and the fact that the inflow is moving from deeper offshore waters toward the shallower waters of the estuary mouth. Particles within 30 km of the mouth accelerate in response to an increased along-stream pressure gradient, somewhat opposed by friction. Stream-normal frictional shear also appears in this region, generating flow curvature and disrupting the simple geostrophic balance (Figure 3.9b).

To conclude, the dynamic assumptions used in the arrested topographic wave-based solutions in previous work (Csanady, 1978; Beardsley and Hart, 1978; Masse, 1990) are relevant outside of the near field. They found a steady state solution using geostrophic dynamics with cross-shelf friction. In this model, time-dependent terms and pressure gradients from plume rotation are also dynamically relevant for inflow within the near field. Although the plume and upstream inflow paths make up a less significant amount of inflow than the downstream shelf path (see analysis in

Results section), they are important to consider when it is necessary to account for all possible paths into an estuary, such as in studies of transport of larvae or pollutants.

3.4.2 *Inflow depth: interpretation and importance*

The downstream shelf inflow path was driven geostrophically (Figure 3.9) by a pressure gradient force that arose in part from the density front between the fresher plume and the more saline shelf. Geostrophic currents at a density front conform to thermal wind balance, wherein the slope of the density front is proportional to the vertical shear of the velocity. Conversely, the consequence of having an inflowing current under the plume is the imposition of vertical shear on plume flow that tilts the density front. This is important because it shows how inflow can modify conventional wisdom about the dynamics of buoyant plumes. The existing theory for calculating the width and depth of river plumes is based on the assumption that the buoyant plume is propagating over a quiescent shelf (no inflow current present) (Chapman and Lentz, 1994; Yankovsky and Chapman, 1997; Lentz and Helfrich, 2001). The slope of the density front is estimated assuming the necessary vertical shear of velocity is merely sufficient to bring the surface current to zero. However, if inflow is present, the vertical shear of velocity must be larger, requiring a larger slope. Thus inflow tilts the density front, and the geometry of the river plume changes.

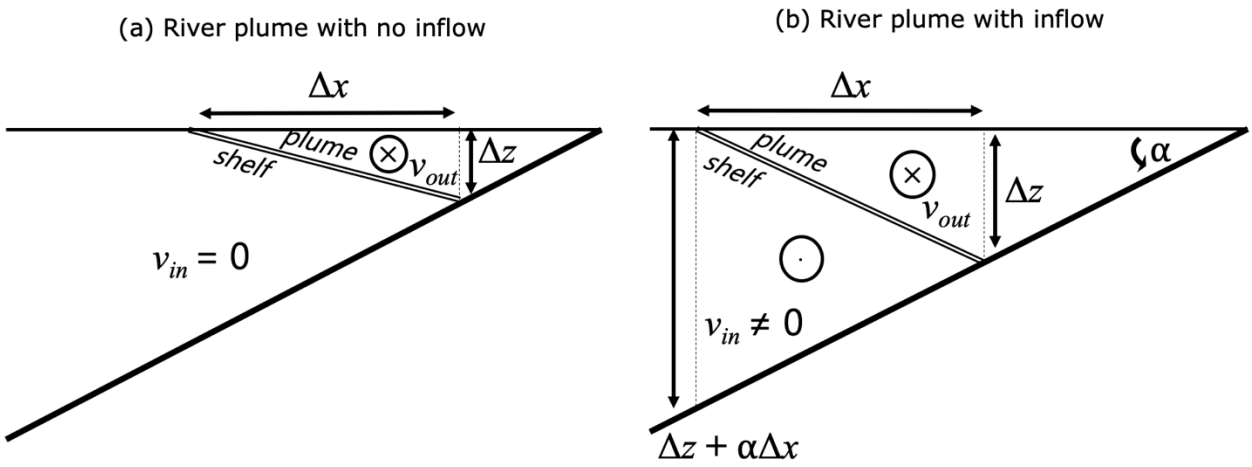

Figure 3.10 Schematic of (a) the cross section of a river plume without an inflowing current, and (b) a river plume with an inflowing current that is deeper, wider, and has a steeper interface.

We use a simple mathematical model to demonstrate the impact of inflowing currents on river plume geometry. A schematic for a cross section of the plume and the shelf is used (Figure 3.10) inspired by the river plume schematics in Lentz and Helfrich (2001) but including an inflow current based on where such a current was seen in the velocity fields of the model (Figure 3.7). In this schematic, the river plume flows through a triangular cross-section under a tilted sea surface height and above a tilted density front. Inflow passes through a triangular section beneath the density front to the seafloor. The triangle of outflow transport and the triangle of inflow transport share a width, Δx (which scales with the Rossby radius) but differ in their heights. The height of the buoyant outflow is the depth of the water column beneath the onshore end of the plume, Δz, plus the height of the sea surface, δz, such that the tilt of the sea surface, $\delta z/\Delta x$, is in geostrophic balance with the outflowing current. The height of the inflow is the seafloor depth beneath the offshore edge of the current, or $\Delta z + \alpha\Delta x$, where α is the seafloor slope. The areas of the outflow and inflow are:

$$A_{out} = \frac{1}{2}\Delta x(\Delta z + \delta z) \simeq \frac{1}{2}\Delta x \Delta z, \textit{ since } \delta z \ll \Delta z \qquad \text{(Chapter 3.5)}$$

$$A_{in} = \frac{1}{2}\Delta x(\Delta z + \alpha \Delta x) \qquad \text{(Chapter 3.6)}$$

We can use the Margules relation for two-layer geostrophic flow at a density front to relate the slope of the front to the velocity difference between the currents (Margules, 1906):

$$v_{out} - v_{in} = \frac{g\prime}{f}\frac{\Delta z}{\Delta x} \qquad \text{(Chapter 3.7)}$$

Next we assume the velocities are spread evenly over their respective areas, such that

$$v_{out} = \frac{Q_{out}}{A_{out}} = \frac{Q_{out}}{\Delta x \Delta z/2} \qquad \text{(Chapter 3.8)}$$

$$v_{in} = \frac{Q_{in}}{A_{in}} = \frac{Q_{in}}{\Delta x(\Delta z + \alpha \Delta x)/2} \qquad \text{(Chapter 3.9)}$$

Finally, because the current is in geostrophic balance, the width Δx will scale as the internal Rossby radius of deformation. For a plume with Froude number < 1, Yankovsky and Chapman (1997) estimate the surface extent that the plume will spread offshore is approximately 4.24 times the Rossby radius, so the formula for plume width we assume is

$$\Delta x = 4.24\frac{\sqrt{g\prime \Delta z}}{f} \qquad \text{(Chapter 3.10)}$$

The difference in a river plume flowing over a quiescent shelf and a river plume flowing over an inflowing current can be found by solving the Margules relation for Δz with $v_{in} = 0$ and with $v_{in} \neq 0$.

3.4.3 *Margules Relation solved with $v_{in} = 0$*

When $v_{in} = 0$, Eq. (Chapter 3.7) simplifies to

$$v_{out} = \frac{g\prime}{f}\frac{\Delta z}{\Delta x} \qquad \text{(Chapter 3.11)}$$

If we substitute Eq. (Chapter 3.8) for v_{out} in Eq. (Chapter 3.11), we get

$$\frac{Q_{out}}{\Delta x \Delta z/2} = \frac{g\prime}{f}\frac{\Delta z}{\Delta x} \qquad \text{(Chapter 3.12)}$$

which can be rearranged to solve for Δz:

$$\Delta z = \sqrt{\frac{2Q_{out}f}{g\prime}} \qquad \text{(Chapter 3.13)}$$

Eq. (Chapter 3.13) matches the result for the depth of a bottom trapped plume derived in Yankovsky and Chapman (1997).

3.4.4 *Margules Relation solved with $v_{in} \neq 0$*

When $v_{in} \neq 0$, Eq. (Chapter 3.7) maintains all terms. Substituting Eqs. (Chapter 3.8) and (Chapter 3.9) into Eq. (Chapter 3.10) so that both velocities are written in terms of net transport,

$$\frac{Q_{out}}{\Delta x \Delta z/2} - \frac{Q_{in}}{\Delta x(\Delta z + \alpha \Delta x)/2} = \frac{g\prime}{f}\frac{\Delta z}{\Delta x} \qquad \text{(Chapter 3.1)}$$

If Eq. (Chapter 3.1) is multiplied by $\Delta x \Delta z(\Delta z + \alpha \Delta x)$, and all terms are moved to the left-hand side of the equation, the result is:

$$2Q_{out}(\Delta z + \alpha \Delta x) - 2Q_{in}\Delta z - \frac{g\prime}{f}\Delta z^2(\Delta z + \alpha \Delta x) = 0 \quad \text{(Chapter 3.2)}$$

The terms can be rearranged so that the equation looks like a cubic in Δz:

$$\Delta z^3 + \alpha \Delta x \Delta z^2 + \frac{2f}{g\prime}(Q_{in} - Q_{out})\Delta z - \frac{2fQ_{out}}{g'}\alpha \Delta x = 0 \quad \text{(Chapter 3.3)}$$

However, Eq. (Chapter 3.3) cannot be solved as a cubic in Δz because Δx is a function of Δz. Once Eq. (Chapter 3.10) is substituted in for Δx, the resulting equation for Δz is:

$$\Delta z^3 + \frac{4.24\alpha g\prime^{\frac{1}{2}}}{f}\Delta z^{\frac{5}{2}} + \frac{2f}{g\prime}(Q_{in} - Q_{out})\Delta z - \frac{8.48\alpha Q_{out}}{g\prime^{\frac{1}{2}}}\Delta z^{\frac{1}{2}} = 0 \qquad \text{(Chapter 3.4)}$$

Eq. (Chapter 3.4) can be reduced by $\Delta z^{\frac{1}{2}}$ to become

$$\Delta z^{\frac{5}{2}} + \frac{4.24\alpha g'^{\frac{1}{2}}}{f}\Delta z^2 + \frac{2f}{g'}(Q_{in} - Q_{out})\Delta z^{\frac{1}{2}} - \frac{8.48\alpha Q_{out}}{g'^{\frac{1}{2}}} = 0 \qquad \text{(Chapter 3.5)}$$

which must be solved numerically.

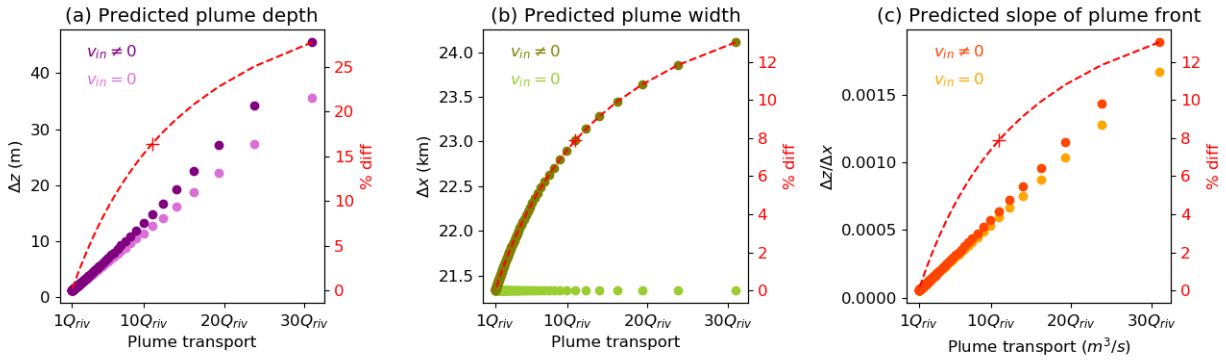

Figure 3.11 Predictions for plume (a) depth, (b) width, and (c) front slope given by the Margules theory with $v_{in} \neq 0$ (Eq. Chapter 3.5) and $v_{in} = 0$ (Eq. Chapter 3.13) for a range of plumes. The percent difference between the two predictions is plotted in red, with a cross indicating where the estuary model is in parameter space.

3.4.5 *Quantifying the impact of $v_{in} \neq 0$*

To examine the impact of including inflow in the river plume schematic ($v_{in} \neq 0$), we compare the predictions for plume shape given by Eq. (Chapter 3.13) with Eq. (Chapter 3.5). Parameter space is explored by varying the plume transport, Q_{out}. For a given river, Q_{out} varies with the amount of mixing the freshwater undergoes before it emerges as a plume on the shelf. As mixing increases, exchange flow volume increases and a larger volume of Q_{out} is produced. The lower limit is no mixing at all, which produces a completely fresh river plume with $Q_{out} = Q_{riv}$, $Q_{in} = 0$, and $S_{out} = 0$ g kg^{-1}. If there is mixing, then $Q_{in} = Q_{out} - Q_{riv}$. If the shelf has fixed slope $\alpha = 0.001$ and salinity $S_{in} = 31$ g kg^{-1}, and the river has fixed outflow $Q_{riv} = 1500$ m^3 s^{-1}. Predictions are made for the shapes of one hundred values of plume volume transport, Q_{out}, corresponding to values of S_{out} from 0 to 31 g kg^{-1}. Appropriate ΔS and Q_{in} can be derived using the Knudsen

relations. The reduced gravity, g', for each plume can be derived given the plume salinity. These values are used to solve Eqs. (Chapter 3.13) and (Chapter 3.5) or the depth, Δz. Then the width, Δx, is solved for using Δz and g'. Finally, the ratio $\Delta z/\Delta x$ is taken to determine the slope. The relative difference is calculated between the predictions given by the theory that includes inflow and the theory that neglects inflow.

The new configuration presented in Figure 3.10b with $v_{in} \neq 0$ predicts a deeper, wider, and steeper plume front (Figure 3.11) than using river plume geometry assuming a quiescent shelf (Yankovsky and Chapman, 1997; Lentz and Helfrich, 2001; Figure 3.10a). The impact of including inflow in the schematic increased for plumes with larger volume transport. To evaluate these theoretical predictions, we can use the numerical ocean model. When using parameters based on the modeled plume properties and found that the density front was predicted to be 7.9% steeper, 7.9% wider, and 16.4% deeper when the shear from the inflowing current was taken into account (these values are represented with crosses on the red percent difference curve in Figure 3.11). For the values of inflow in the model (Figure 3.4b), the predicted Δz increased from 12.6 m to 14.7 m, and the predicted Δx increased from 21.3 km to 23.0 km. These updated predictions for Δz and Δx better capture the position of the density front and the location of the currents in the model output (Figure 3.12), which supports the claim that this process is occurring as described. While these geometric changes are small compared to the spatial scale of the plume, they can be significant for applications in which ocean properties of interest change over vertical and horizontal spatial scales smaller than the plume (as is common in the coastal ocean). The values of S_{out} and Q_{riv} used for this calculation are presumed reasonable for a typical partially-mixed estuary; recall that the modeled estuary was constructed to have dynamics typical of

partially-mixed estuaries given its placement in the middle of Geyer and MacCready (2014) parameter space. The impacts on plume shape prediction were the result of allowing additional shear on geostrophic flow at a density front, as was suggested by the vertical position of the inflowing current in the model results.

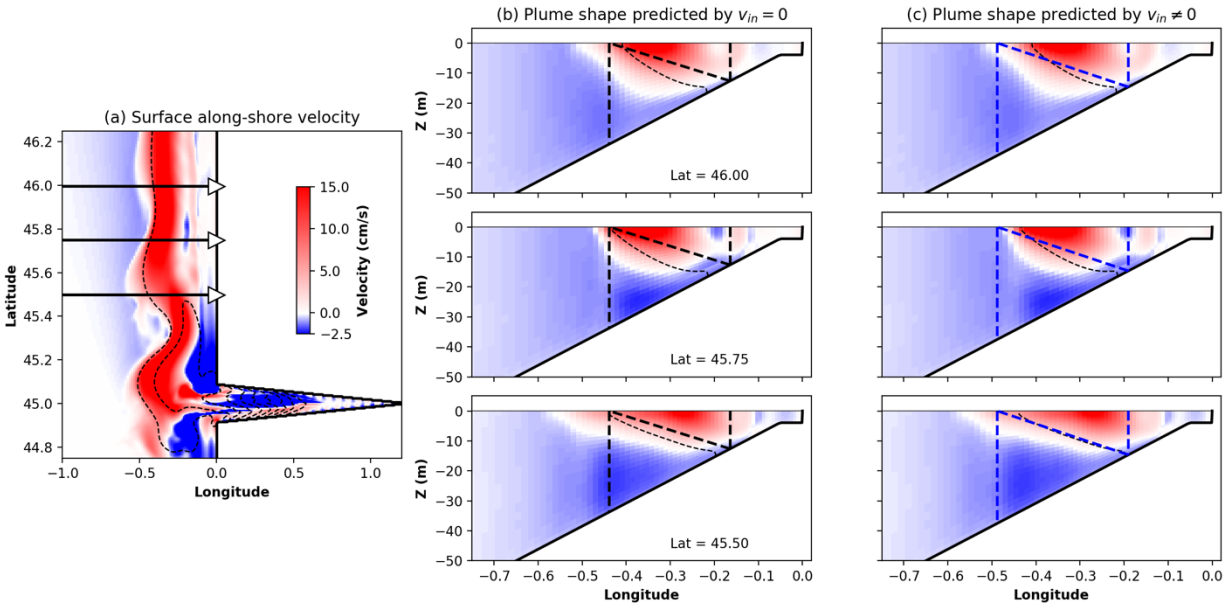

Figure 3.12 Demonstration at (a) three plume cross sections comparing the different theoretical predictions of plume shape to the velocity field and isohalines (salinity is contoured as in previous figures). (b) Predicted plume shape assuming $v_{in} = 0$ (Eq. Chapter 3.13) (black), and (c) predicted plume shape allowing $v_{in} \neq 0$ (Eq. Chapter 3.5) (blue).

One other result worth noting is that the plume width, Δx, does not increase with plume transport when $v_{in} = 0$. This is because the solution for $\Delta z \propto \frac{1}{\Delta S}$ in the $v_{in} = 0$ case (Eq. Chapter 3.13) and $g' \propto \Delta S$. Therefore, the internal wave speed, $\sqrt{g'\Delta z}$ does not change when ΔS is varied, and subsequently neither does the Rossby radius of deformation of the plume or Δx. When $v_{in} \neq 0$, Δz (as solved for in Eq. Chapter 3.5) changes more rapidly than $\frac{1}{\Delta S}$ (Figure 3.11), freeing the internal

wave speed to increase as ΔS decreases. This means that considering $v_{in} \neq 0$ not only increases estimates of Δx, but $v_{in} \neq 0$ is a prerequisite for the plume width Δx to vary with ΔS.

This study assumed a geometric schematic of the shape that the estuarine inflow current takes on the shelf based on the results in an idealized model (occupying a triangle beneath the river plume) similar to previous river plume studies (Yankovsky and Chapman, 1997; Lentz and Helfrich, 2001) and hypothesized a mechanism by which inflow occupying that space may deepen and widen the river plume. Considering these changes to river plume geometry is significant, as the width of the river plume could have consequences for along-shelf transport and exchange (Banas et al. 2009). The depth of the river plume is important for shelf transport as well, as Jia and Yankovsky (2012) posited that if a river plume deepens enough to displace the thermocline, instabilities develop which enhance off-shelf transport of plume water. So, understanding the currents inflowing to and outflowing from an estuary likely have consequences for shelf transport.

3.4.6 *Drawbacks*

The proposed inflow schematic (Figure 3.10) is a depiction of where the inflowing current is fastest, but the triangular bounds drawn do not actually encapsulate all of the downstream shelf water that eventually enters the estuary. This can be seen distinctly in the TEF results (Figure 3.6a). On the downstream edge of the largest shelf box in Figure 3.6a, more inflowing transport is occurring offshore of the plume edge than beneath the plume edge. Further, the downstream shelf particles tend to originate offshore of the plume rather than beneath it, if the isohaline contours are taken to accurately represent the edge of the plume (Figure 3.5). Thus, the inflow

schematic should not be taken as a depiction of where all inflow originates, but rather as a depiction of a relatively fast current that is spun up on the shelf by estuarine exchange and the geostrophic dynamics that then modify the river plume.

Another drawback is that the schematic for inflow is derived from the simplest case scenario and it may not hold under all combinations of complicating conditions. Inflow may hypothetically be uncoupled from outflow if either wind forcing at the surface or ambient currents at depth separate them. Wind forcing has been observed to displace and bifurcate plumes (Hickey et al. 2005). A schematic for river plumes under upwelling winds has been developed where the plume detaches from the shelf (Fong and Geyer, 2001; Lentz, 2004); however, this previous research does not indicate whether the inflowing current would follow the plume offshore. Model results and observations at the mouth of Chesapeake Bay suggest that in the presence of an ambient shelf current, estuaries will source inflow primarily from *upstream* of the channel mouth, the opposite direction from where inflow is primarily sourced without currents (Valle-Levinson et al., 1996; Valle-Levinson et al., 1998; Masse, 1990). Again, whether inflow and outflow would vary together in the presence of a shelf current or maintain the thermal wind interaction described above is unclear. This particular model did not include shelf stratification which could create additional effects. Because no shelf in nature lacks wind, ambient currents, or stratification, validation against real estuaries is, at this point, difficult.

3.4.7 *Future directions*

The next step toward understanding inflow is to perform experiments using a similar model under upwelling- and downwelling-favorable winds. The main questions would be whether

inflow and outflow stay coupled when surface forcing is applied and how the shape of the inflow current changes when upwelling circulation spins up. Upwelling circulation includes Ekman transport in the boundary layers and a geostrophic current in the middle of the water column (Lentz and Fewings, 2012). The geostrophic current could change the direction from which inflow is sourced (Masse, 1990). Beyond that, it would be important to validate the source of inflow in the results from the idealized model with high resolution realistic models of estuaries. Further validation with observations would also be beneficial. Additionally, the role of shelf stratification on inflow could be addressed, as well as the role of topographic features such as undersea canyons.

3.5 CONCLUSION

Exchange flow in an estuary draws in ocean water (inflow) and ejects mixed water (outflow). The source of inflow has been examined here in an idealized, three-dimensional primitive equation model. The prior body of work on the inflow problem consisted of barotropic analytical models styled on the arrested topographic wave solution (Csanady, 1987; Beardsley and Hart, 1987; Masse, 1990). Outstanding questions included the path of the flow on the shelf before it arrives in the estuary (especially the width and depth of the estuary-bound current) and the interactions on the shelf between estuary inflow and estuary outflow. The three-dimensional model with full ocean dynamics here allows for nonlinear dynamics and entrainment between the shelf and the outflowing plume. We find that exchange between the shelf and the plume occurs at a rate comparable to the rate of exchange within the estuary. The model here reproduced inflow patterns from previous research (Beardsley and Hart, 1978; Masse, 1990) far from the channel mouth, wherein the dominant source of inflow was found downstream of the estuarine

channel and inflow travelled in a geostrophic coastal current. However, near the mouth, nonlinear dynamics became non-negligible. The three-dimensional model found new, albeit smaller, inflow paths originating in the plume and upstream of the estuarine channel. On the shelf downstream of the channel, the presence of the geostrophic inflowing current beneath the plume increased shear of the plume current. The increased shear is in thermal wind balance with a steepened density front at the plume-shelf interface. This balance requires a plume that is deeper and wider than predicted by theories for plume shape in the existing literature that did not account for an inflow current (Yankovksy and Chapman, 1997; Lentz and Helfrich, 2001). We present a modified theory that gives predictions for plume width and depth that were found to more accurately describe the shape of the inflowing and outflowing currents on the shelf in the model, albeit the difference in the predictions between the two theories was modest. While the inclusion of inflow in the conceptual model of plume flow has a small effect on the plume geometry, the change to shelf transport is significant because the inflowing current has approximately the same transport as the plume. It remains an open question whether the inflow and outflow stay coupled under wind forcing or shelf currents.

Understanding where the inflow current lies on the shelf is important for understanding the transport pathways on the shelf and into the estuary. These pathways move salt, thermal content, nutrients, oxygen, and invasive species larvae. In glacial fjords, the thermal content of inflow can change the melting rate of glaciers (Sutherland and Straneo, 2012). Fjord temperature is increasingly recognized to be important for glacier melt, as recent observations near a tidewater glacier found that the rate of ambient glacial melt is orders of magnitude larger in the meltwater budget than initial theories predicted (Jackson et al., 2019). Therefore, understanding the source

of inflow on the shelf has consequences for estuarine dynamics, shelf dynamics, biology, chemistry, and the future of ice.

Chapter 4. WIND STRESS EFFECTS ON THE SOURCE OF ESTUARINE INFLOW IN AN IDEALIZED MODEL

4.1 INTRODUCTION

Wind-induced upwelling is a path for deep water to get into the shallow nearshore regions, including estuaries and bays. Deep water is notably dense, cold, rich in nutrients but low in oxygen and pH. Because of the nutrient content of deep water, wind-induced upwelling is a major source of nutrients for primary producers in the coastal ocean, but in estuaries, which are often nutrient-loaded, upwelling can have detrimental effects. In 2007, a massive shellfish die off along the west coast of North America was attributed to the upwelling of a bacteria, *Vibrio tubiashii*. It was postulated that *V. tubiashii* populations rose from the deep Pacific after an unusually strong upwelling season in late July and August of 2007, then multiplied explosively in the unusually warm surface temperatures that followed. The outbreak caused up to 59% reduction in oyster hatchery production in one key west coast hatchery (Elston et al., 2008). Other examples of undesirable wind effects on estuaries include the upwelling of hypoxic water into the Columbia river estuary (Roegner et al. 2011) and Mobile Bay (Coogan, et al. 2019), depriving marine animals of oxygen. Upwelling-sourced nutrients are important to some nitrogen-depleted estuaries, encouraging production of macroalgae and a reduction in eelgrass in some nutrient-depleted estuaries along the northern California Current system (Hessing-Lewis and Hacker, 2013).

The horizontal change in the source of inflow may also change under wind stress, with a different set of consequences. Although vertical gradients in density, nutrients and oxygen are typically stronger than horizontal gradients in the coastal ocean, the lateral source of inflow may impact the whether planktonic larvae can reach an estuary (Pringle et al., 2011) or the intrusion of rivers or phytoplankton blooms to an estuary (Roegner et al., 2002).

This link between the shelf response to wind stress and the estuarine ecosystem is therefore consequential, but it is currently understood as a correlation. The physics that bridges the shelf-estuary connection is still full of unanswered questions. Here we will focus on the effects of wind on the paths that connect shelf water to the estuary. This study seeks to answer the following questions:

1. How does the path into an estuary changes during upwelling and downwelling wind stress? Is deeper water pulled into the estuary during upwelling-favorable wind events?
2. How does the direction from which inflow is drawn change under wind stress?
3. How does the rate of inflow to an estuary change under wind stress?

4.1.1 *The effect of wind stress on estuaries*

Wind advects surface waters through Ekman transport in the surface and bottom boundary layers, horizontally converging or diverging at the coastal boundary. This results in upwelling or downwelling and tilted isopycnals in the nearshore region (Lentz and Fewings, 2012). These effects happen within both the estuarine channel (local) and on the shelf (remote). The relative significance of remote and local wind stress on the estuary depends on the spatial scale of interest (Wong and Moses-Hall, 1998), but the combined effects have strong biological

implications: one study estimated 88% of the dissolved oxygen distribution in Chesapeake Bay was attributable to physical, rather than biological, effects (Du and Shen, 2014). Here, upwelling-favorable and downwelling-favorable are defined with respect to the shelf response, since an estuary has two banks such that one will be down-wind and one will be up-wind regardless of the direction of wind stress. The estuarine response to wind stress is a combination of a local response and a remote response to the changes on the shelf (Wong and Moses-Hall, 1998). Local wind stress is important in estuaries where high stratification generates and maintains hypoxic or even anoxic bottom layers. These situations become lethal when estuarine bottom water is upwelled along the up-wind bank (Kemp et al., 2009), as observed in Chesapeake Bay (Scully, 2016), Mobile Bay crab jubilees (Schroeder and Wiseman Jr., 1988), and fish kills in the Neuse river estuary (Reynolds-Fleming and Luettich Jr., 2004). Remote wind stress changes the estuary by acting on the adjacent shelf, mostly evident as changes in river plume position. By raising or lowering sea level at the coast, wind generates a barotropic pressure signal at the coast that propagates into the estuary or bay (Wong and Moses-Hall, 1998).

Despite these biologically important responses to the redistribution of density in estuaries by wind stress, the volume flux of the estuarine exchange flow may be relatively unchanged in response to wind stress. This hypothesis follows from a modeling study that found that cross-estuary and along-estuary responses to alongshore wind stress seemed to offset each other (Chao, 1988). During upwelling-favorable wind stress, wind advection opposed the cross-estuary sea level set-up from Coriolis, while Ekman transport (down-estuary at the surface, compensated by up-estuary at depth) reinforced the along-estuary density-driven set-up. During downwelling-favorable wind stress, wind advection reinforced the cross-estuary sea level set-up while Ekman

transport (down-estuary at surface, up-estuary at depth) opposed the along-estuary density-driven set-up (Chao, 1988). Only cross-shore wind stress could significantly affect transport in the estuary. This cross-shore wind effect has been observed in the Hudson River, wherein the volume of estuary outflow was enhanced by offshore winds (Ralston, et al., 2007; Jurisa and Chant, 2012). Here, we focus on the impact of alongshore wind to supplement the qualitative result in Chao (1988) by using Total Exchange Flow (TEF) (MacCready, 2011) to quantify the change, if any, that alongshore wind produces in estuarine exchange flow. TEF estimates the volume and salinity of inflow and outflow in exchange flow using a salinity-weighted coordinate calculation.

4.1.2 *The effect of wind stress on the shelf origin of estuarine inflow*

Earlier work interested in identifying the source of estuarine inflow found that, when there is an alongshore current (due to winds or otherwise), inflow will originate from the direction from which the current is flowing. This was found using two-dimensional analytical solutions for the streamfunction of inflowing water. Inflow is modelled mathematically as constant removal of shelf water at a location on the coast representing the estuary mouth. The analytical solution can be found for vertically homogeneous shelf water in a two-layer ocean using the steady-state, frictional, rotating shallow-water equations of motion on a sloped shelf (Beardsley and Hart, 1978; Masse, 1990). The inflowing water streamfunction with wind stress looks very different from the no-wind case. In the no-wind case, there is no current to pull from. Inflow is sourced from the direction of coastal trapped wave propagation (from the right when looking to the shelf from the estuary in the northern hemisphere) because of Coriolis and bottom friction. As flow approaches the estuary from a sloped shelf, it encroaches into shallower water where bottom

friction is more effective at decelerating the flow. As inflow decelerates, it turns to its left due to Coriolis. From the perspective of the estuary receiving this flow, inflow approaches from the right (Beardsley and Hart, 1978; Masse, 1990; Chapter 3). Because the estuarine inflow and outflow are both to the right of the estuary, there is some overlap between them that shears the plume-front interface. The paths of inflow slowly extend offshore with distance from the estuary mouth but there is no upper limit on the offshore distance from which inflow can be sourced; the shape diffuses as in Csanady's arrested topographic wave solution (Csanady, 1978). That is, the rate of turning and offshore spread of the paths of inflowing water scale as the ratio of the Coriolis force to the strength of bottom friction acting on the water column (Csanady, 1978; Masse, 1990). In these solutions, inflow approaches the estuary from the right at a gentle arc that asymptotes towards a coast-parallel current as distance increases from the channel mouth.

When wind is introduced, an alongshore current develops that changes the inflow solution significantly because the estuarine inflow is drawn from the alongshore current. The reasoning here is reproduced from Masse (1990). The first consequence of the alongshore current is that inflow does not necessarily enter from the right – under downwelling-favorable winds, for example, inflow originates from the left. Another consequence of drawing inflow from an alongshore current is that the inflowing water is sourced from a finite distance offshore. The estuary requires a certain amount of inflow, Q_{in}, to balance mass and salt content. This inflow is sourced from the ambient current. From some offshore point, x_0, the estuary will have drawn the requisite inflowing water, Q_{in}. This x_0 is determined by Q_{in} and the along shelf current assumed to have constant strength, v_0:

$$Q_{in} = |v_0| \int_{-x_0}^{0} h(x)\, dx \qquad \text{(Chapter 4. 1)}$$

where $h(x)$ is the seafloor depth as a function of offshore distance. For the west coast model in this study, the x-axis is positive in the onshore direction; in east coast models, the x-axis will be positive in the offshore direction. In Masse (1990), $h(x) = -x\alpha$, where α is the constant shelf slope, so Eq. (Chapter 4.1) solved for x_0 is:

$$x_0 = \sqrt{\frac{2Q_{in}}{\alpha|v_0|}} \qquad \text{(Chapter 4.2)}$$

Plugging in example values, x_0 = 20 km when using Q_{in} = 10,000 m^3s^{-1}, α = 0.001, and v_0 = 0.05 ms^{-1}. Note that x_0 is independent of the sign of v_0 (Masse, 1990). Here we explore the hypotheses that under wind stress, inflow will originate in an alongshore current driven by that wind stress, and thus come from the same direction the wind is coming from; and that inflow will be sourced from a coastal current of finite width.

4.2 METHODS

The impact of wind stress on the source and rate of estuarine inflow can be isolated and interrogated by using an idealized numerical model. The model for this study was built using the Regional Ocean Modeling System (ROMS), which is a three-dimensional Reynolds-averaged Navier-Stokes model that uses a terrain-following vertical coordinate (Shchepetkin and McWilliams, 2005). The model used in this study features a river flowing out onto a slightly stratified shelf (N=0.01 s^{-1}). The model grid is based on that of MacCready et al. (2018), but with a 30-m no-slip coastal wall (Figure 4.1). The deeper coastal wall was added to prevent plume water from becoming trapped along the coastline. The shelf is linearly sloped (slope of 1 m per 1 km offshore distance). The river channel is v-shaped and widens and deepens toward the mouth to about 20 m deep and 20 km wide. The grid is plaid and has telescopic resolution, with highest horizontal resolution of 500 m near the estuary mouth. The resolution is coarser around the

model edges. The vertical grid had 30 levels that stretch to follow bathymetry and the free surface. Fresh water was added to the model through the river channel at a constant rate of 1,500 $m^3\ s^{-1}$. The three open ocean boundaries (offshore, north, and south) used boundary conditions described by Chapman (1985) for the surface elevation and Flather (1976) for momentum terms. Bottom stress is modeled using a logarithmic drag function with a roughness length of z_0 = 0.0005 m, consistent with a sandy seafloor (Soulsby, 1983). A single-frequency, 12-hour tidal forcing was used to enhance mixing. Turbulent mixing was modeled using the k–ϵ turbulence closure parameters (Umlauf and Burchard, 2003).

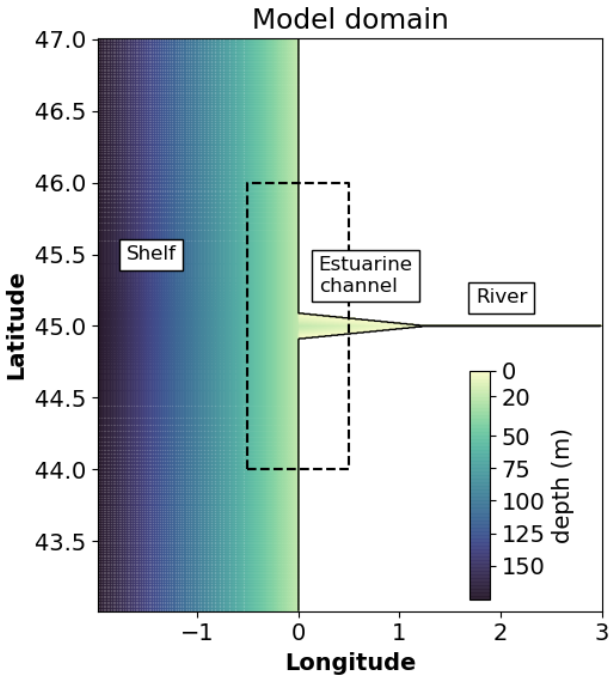

Figure 4.1 Model domain and bathymetry. The dashed box indicates the subset of the model domain that is the focus of subsequent plots and analysis.

The model was run without wind stress for 45 days to let exchange flow spin up to a quasi-steady state. Five alongshore wind stress experiments were then performed, including one no-wind control case. Following spin-up, wind stress was added to the model over a subsequent 45-day

period with values of ±0.01 Pa or ±0.0025 Pa (negative for upwelling, positive for downwelling) to test the effect of upwelling- and downwelling-favorable wind stress on exchange on the shelf and in the estuary. To examine the source of inflow, particle tracking experiments were used. To examine the rate of inflow, the estuarine exchange flow was quantified using TEF (MacCready, 2011).

Particle tracking experiments determined where inflow originated on the shelf. These experiments consisted of choosing initial locations for the particles and calculating where they would go if they were passively advected by the ocean currents and mixed by turbulence. Inflowing particles are identified as those that, at any point after their release, entered the estuarine channel. The paths of inflowing water were visualized by plotting the paths of the inflowing particles. The particle tracking algorithm worked by forward-integrating a particle's position using the currents interpolated in time from saved hourly snapshots from the model. The forward integration scheme used is 4^{th}-order Runge-Kutta with a 300-second time step to resolve tides, similar to that used in Banas et al. (2009), Giddings et al. (2014), Brasseale et al. (2019), and in Chapter 3. Vertical turbulent diffusion of particles was modeled as a random walk, following the technique developed by Visser (1997). A nearest-neighbor search algorithm was used for finding the velocities used to advect particles. 7500 particles were released at 25 evenly-spaced offshore positions, 30 evenly-spaced alongshore positions, and 10 vertical positions.

The rate of exchange flow was determined using TEF (MacCready, 2011). In TEF, inflow and outflow were calculated using isohaline coordinates to account for tidal variation in the distribution of salinity and velocity. The resulting transports through a section consisted of four

tidally-averaged time series of: the volume transport of the in- and outflow, Q_{in} and Q_{out}, and their flux-weighted salinities S_{in} and S_{out}. The calculation was done using the "dividing salinity" method (MacCready et al. 2018; Lorenz et al., 2018). Chapter 3 extended TEF to integrate across shelf boxes as well as estuarine cross sections, conceptually treating the river plume and any compensating inflow as an extension of the estuary onto the shelf.

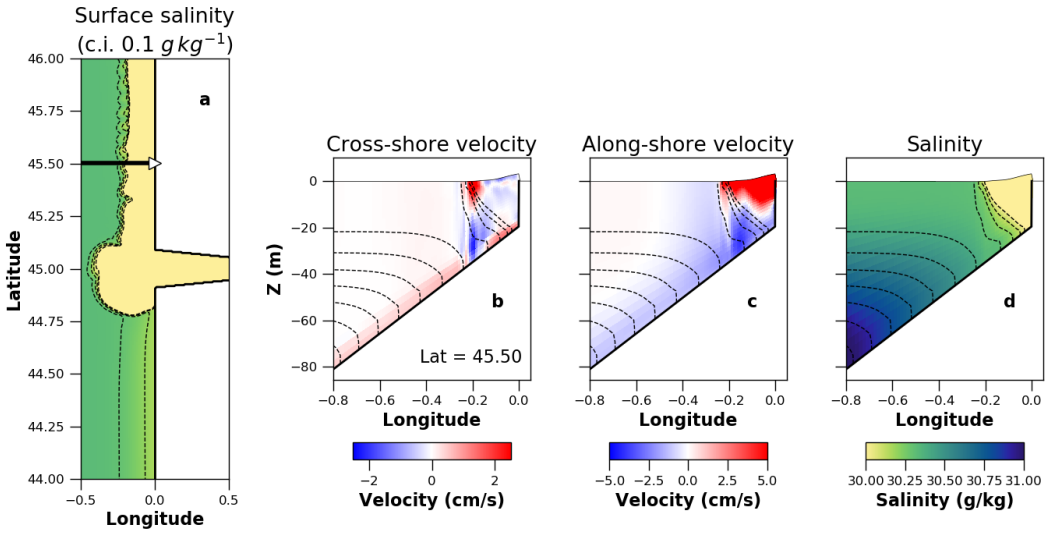

Figure 4.2 The salinity and velocity fields of the no-wind control experiment, averaged over a 24-hour period two weeks after the start of the experiment. Subplot (a) is a plan view of surface salinity (contoured from 30–31g kg^{-1}, with a contour interval of 0.1 g kg^{-1}, same color fill as in (d)); the arrow indicates the location of the cross-section depicted in (b)–(d). Subplots (b) and (c) depict velocity (color fill) with salinity contoured (contour interval same as in (a)). Subplot (d) depicts salinity at the cross section in color to provide reference for the values of the contours in (a)–(c). Surface height in (b)–(d) has been exaggerated by a factor of 100.

4.3 RESULTS

4.3.1 *General model description*

Exchange within the no-wind estuary was characteristic of a partially-mixed estuary within the Geyer and MacCready (2014) estuary classification. The estuarine outflow produced a buoyant

plume on the shelf (Figure 4.2a). The plume formed an anticyclonic bulge outside of the estuary mouth before turning to the right to form a northward current. The alongshore velocity field indicated that the primary return flow i\was found to the right of the estuary, with the strongest velocities found directly under the plume (Figure 4.2c). No ambient shelf currents formed. That is, in the no-wind experiment, inflow and outflow were found downstream of the estuary with respect to the direction of coastal-trapped wave propagation.

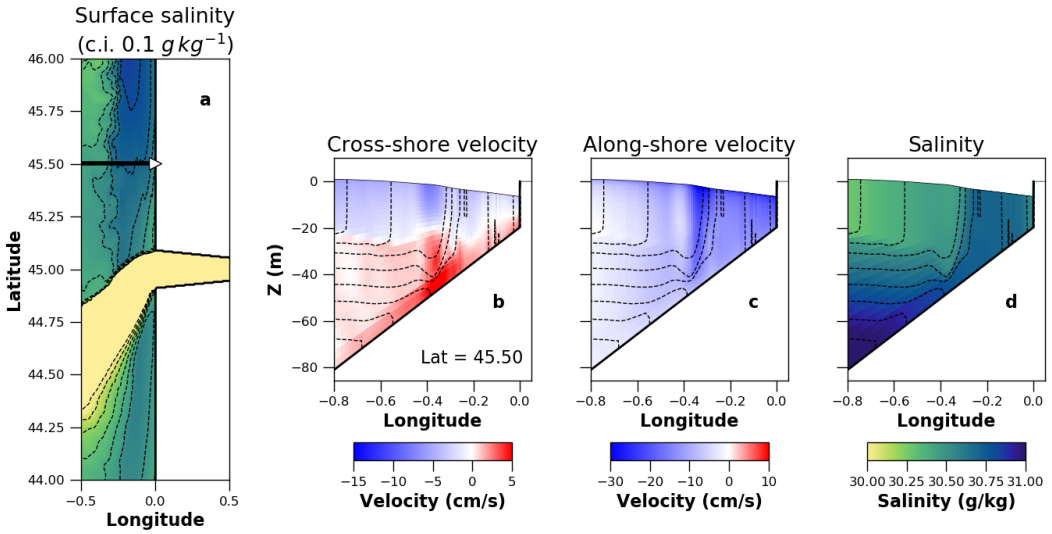

Figure 4.3 As Figure 4.2, but for the strong upwelling experiment. The velocity fields are averaged over a 24-hour period two weeks after the start of the experiment.

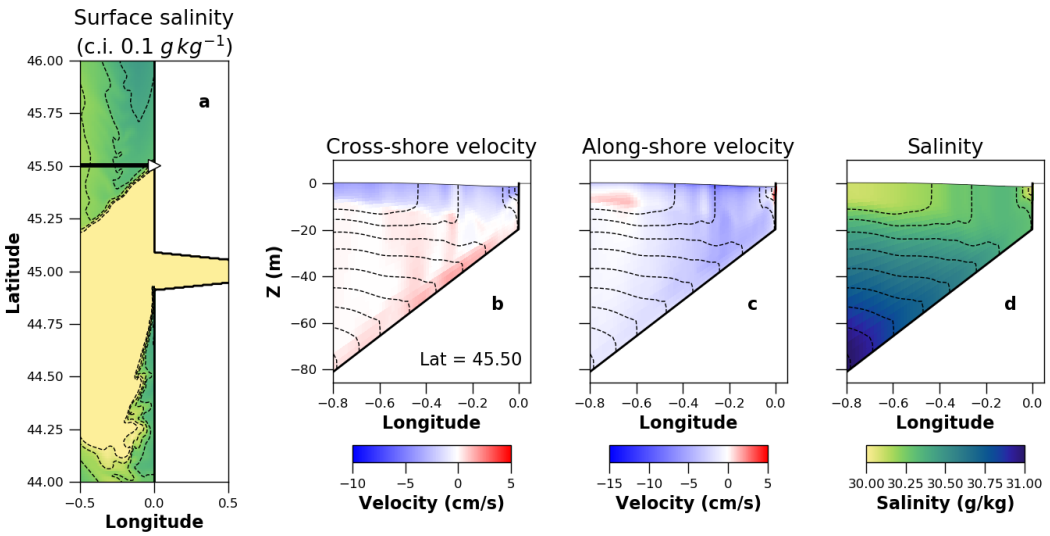

Figure 4.4 As for Figure 4.2 and Figure 4.3, but for the weak upwelling experiment. The 24-hour averaged fields are taken four weeks after the start of the experiment, because the plume takes longer to adjust under weaker wind stress.

For the upwelling experiments, Ekman transport occured in the surface in both upwelling experiments, transporting water offshore (Figure 4.3b and Figure 4.4b) and lowering the sea level along the coast (Figure 4.5a and Figure 4.5b). This sea level tilt drove a downwind alongshore current near the coast of 19 cm s^{-1} in the strong upwelling case (Figure 4.3c) and 3 cm s^{-1} in the weak upwelling case (Figure 4.4c). The plume was driven offshore and to the left of the estuary at approximately a 45° angle, growing wider as it moved offshore. The bulge was absent in the strong upwelling experiment, but it was still discernible in the weak upwelling experiment where some plume water began to move to the right before being pulled offshore by Ekman transport and downwind by wind advection. The offshore Ekman transport also drove a baroclinic response at the coast by lifting isopycnals to form a cross-shore density gradient (Figure 4.3d and Figure 4.4d).

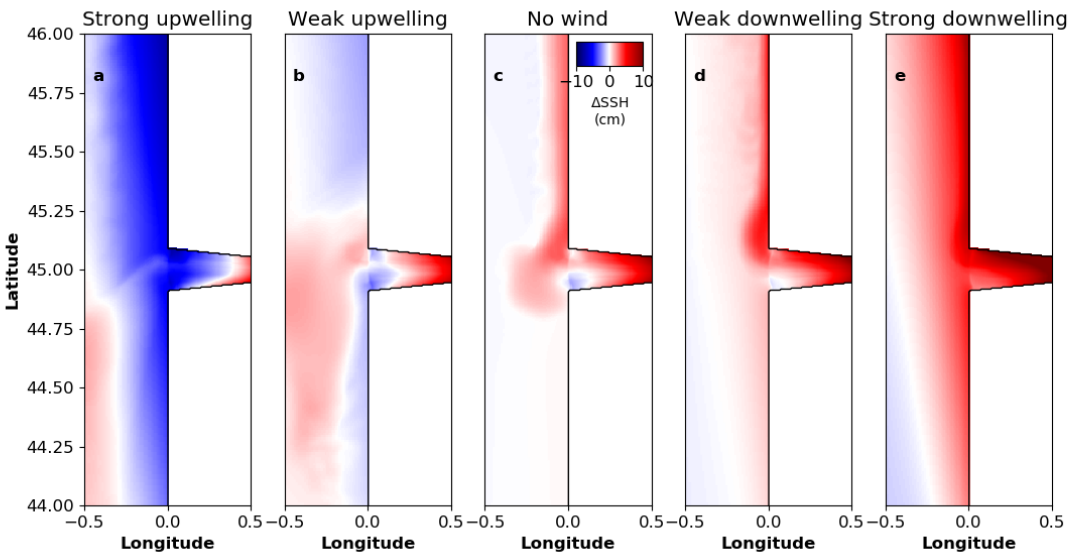

Figure 4.5 Sea surface height (SSH) displacement from a reference sea level of a quiescent ocean for the five experiments. SSH values are 24-hour averages taken at two weeks for the strong wind stress experiments and the no-wind experiment, and at four weeks for the weak wind stress experiments.

In the two downwelling experiments, Ekman transport moved surface water onshore (Figure 4.6b and Figure 4.7b), raising the sea level at the coast (Figure 4.5d and Figure 4.5e). This drove downwind along-shore currents of 18 cm s^{-1} in the strong downwelling experiment (Figure 4.6c) and 7 cm s^{-1} in the weak downwelling experiment (Figure 4.7c). Isopycnals initially tilted downward at the coast, but onshore Ekman transport at the surface filled the nearshore region with homogeneous water, pushing the density front offshore and arresting cross-shore transport in the nearfield (Figure 4.6d and Figure 4.7d) as described in Austin and Lentz (2002). The plume flowed to the right as in the no-wind case, as the ambient current was flowing in the direction of coastal trapped wave propagation which steers the plume in the absence of wind, but it was pushed onshore by Ekman transport. This resulted in a thinner plume relative to the no-wind case. As in the upwelling experiments, the bulge wa absent in the strong downwelling case, but it was still slightly discernible in the weak downwelling case.

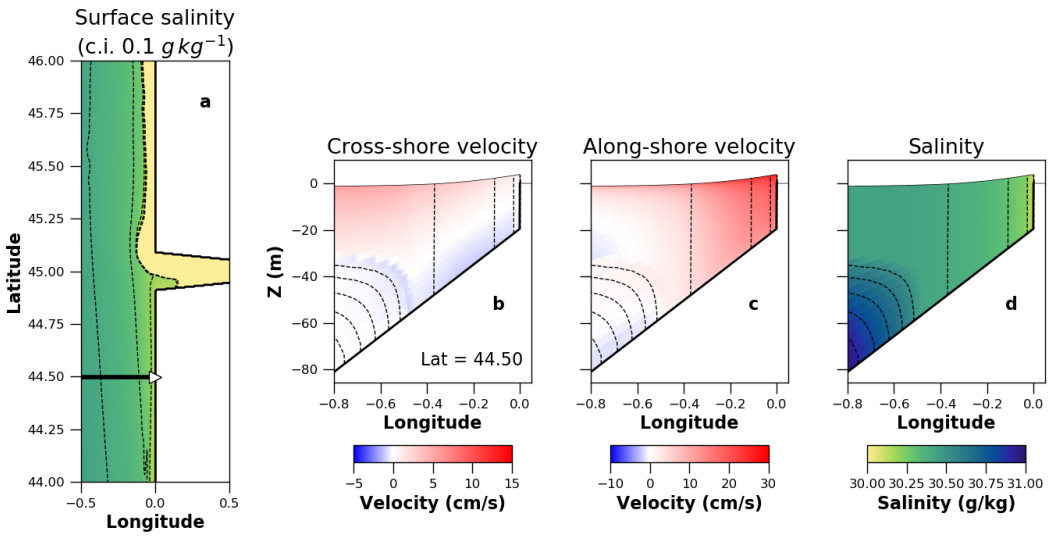

Figure 4.6 As Figure 4.2, Figure 4.3, and Figure 4.4, but for the strong downwelling experiment. The 24-hour averaged fields are taken two weeks after the start of the experiment.

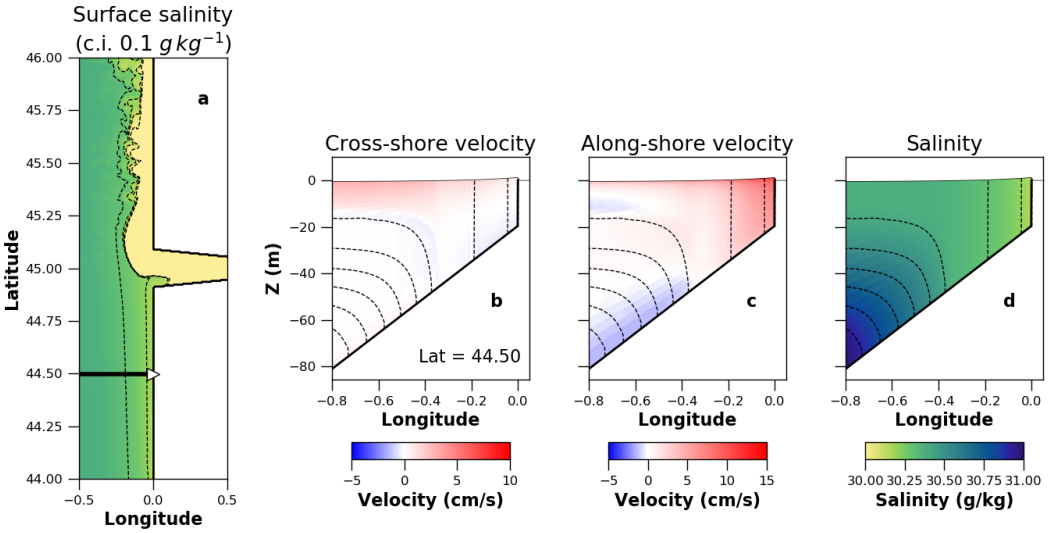

Figure 4.7 As Figure 4.2, Figure 4.3, Figure 4.4, and Figure 4.6, but for the weak downwelling experiment. The 24-hour averaged fields are taken four weeks after the start of the experiment.

4.3.2 *Particle tracking results*

In the no-wind experiment, particles that flow into the estuary originate primarily from the right (Figure 4.8e), with some originating from the left in eddies south of the bulge, also found in simulations in Chapter 3.

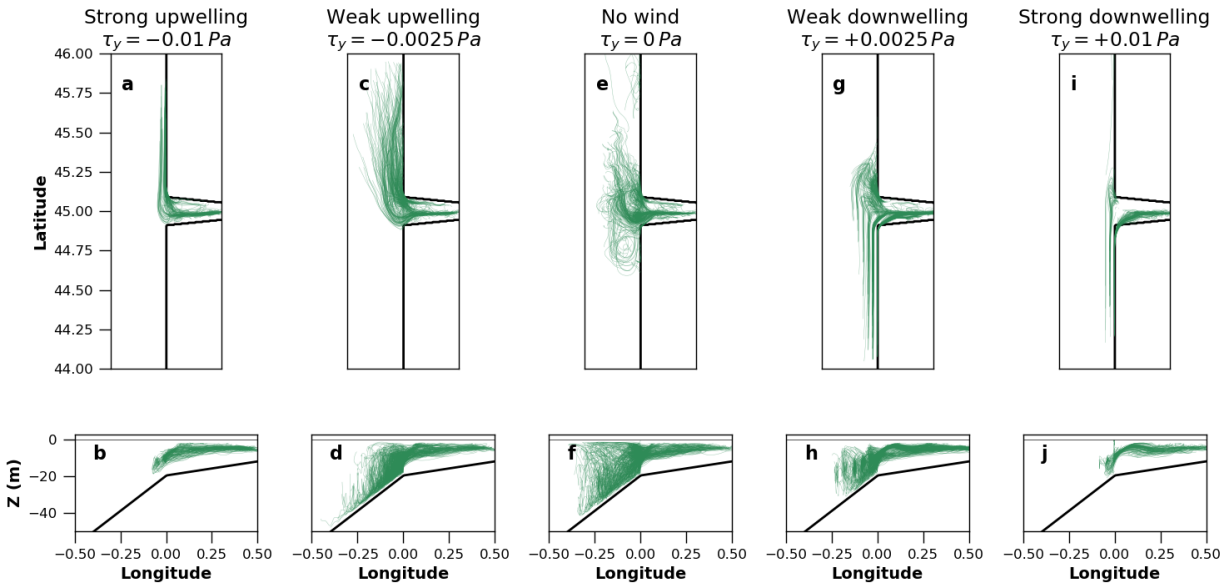

Figure 4.8 Tracks of particles that were released on the shelf and reached the estuary within a 30-day period under five wind conditions (increasing from strong upwelling-favorable at left to strong downwelling-favorable at right). The top row displays the tracks in plan view and the bottom row displays them in profile. The tracks have been tidally-smoothed using a Godin filter (Godin, 1972); any corner-cutting by tracks is a byproduct of the filter.

In the upwelling experiments, the particles that flowed into the estuary originated from the right of the estuary in the alongshore current driven by the lower sea level at the coast. In the strong upwelling experiment, the only particles that reached the estuary were released within a few kilometers of the coast (Figure 4.8a). In the weak upwelling experiment, particles reached the estuary from release points farther offshore (Figure 4.8b). This result is consistent with the theory that the offshore extent of inflow is inversely proportional to the speed of the ambient alongshore current (described in Masse (1990), summarized in section 4.1.2).

In the downwelling experiments, the inflowing particles that reached the estuary originated from the south, to the left of the estuary (Figure 4.8d and Figure 4.8e). Similar to the upwelling experiments (shown in Figure 4.8a and Figure 4.8b), the inflowing particles originated closer to

the shore during the strong downwelling-favorable wind stress than the weak downwelling-favorable wind stress. During weak downwelling wind stress, the estuary drew some particles from the right, sourcing them from the plume current. This is visible as a u-turn at the mouth in some particle paths (Figure 4.8g).

4.3.3 *TEF results*

After wind stress was introduced, the rate of inflow to the estuarine channel as found by TEF fluctuated for about 10 days (Figure 4.9b and Figure 4.9d). The length of this adjustment period was comparable to the observed 8-days required for the spin-up of the upwelling front on the Oregon coast (Austin and Barth, 2002). After the adjustment period, the rate of inflow to the channel under wind stress settled to nearly the same rate as the no-wind experiment, with one minor exception: the exchange rate for the strong downwelling experiment at the mouth settled to a rate that was elevated by about 20% (Figure 4.9d). The channel response differs from the shelf response, wherein the exchange rate between the plume and the shelf was elevated during strong wind stress and did not approach a steady state (Figure 4.9f). As a whole these results suggest that under wind stress, exchange between the plume and the shelf was enhanced relative to the no-wind case, but exchange flow in the estuary occurred at the same rate.

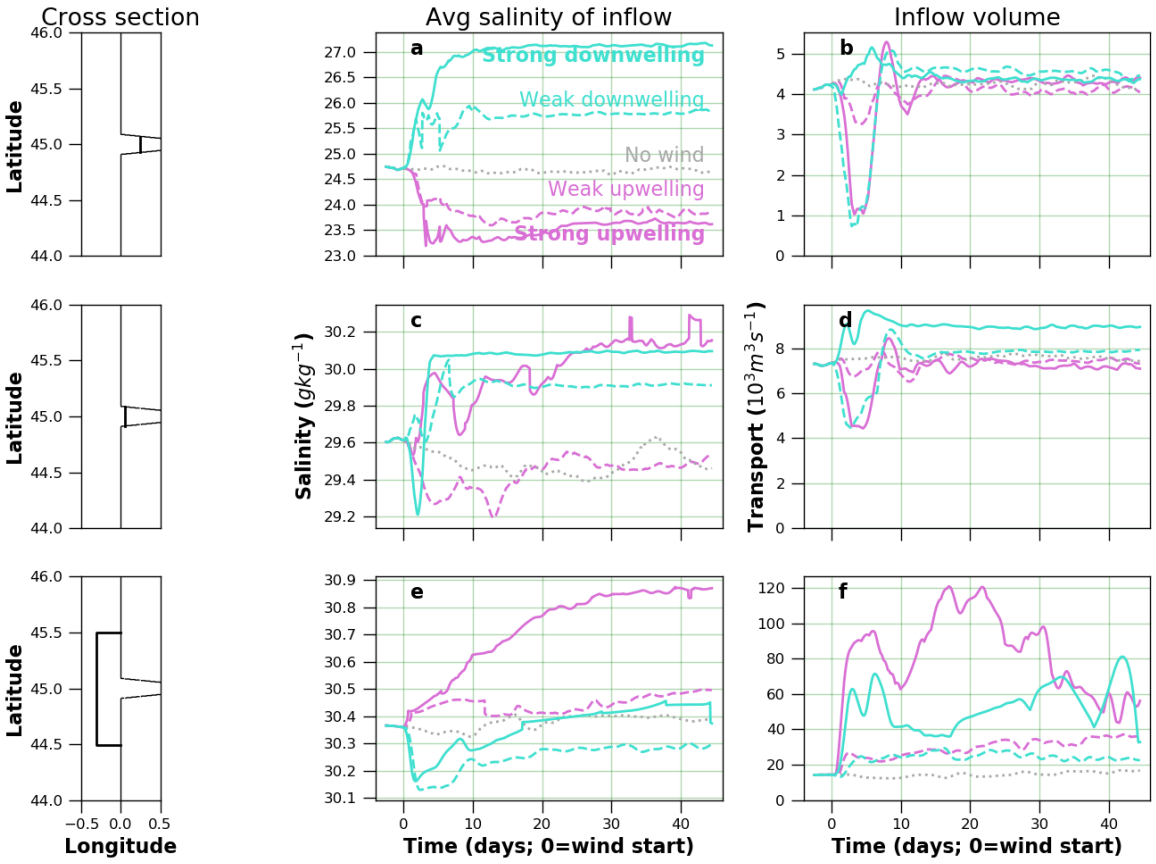

Figure 4.9 Evolution of bulk properties of inflow over 45 days after the start of wind stress, at three cross-sections. Cross-section locations are depicted in the left column at the mid-estuary, the estuary mouth, and a shelf box. The middle column (a, c, e) depicts the time evolution of the average salinity of inflow at the given cross-section. The right column (b, d, f) depicts the rate of transport of inflow. Results from each of the experiments are plotted in a consistent line format: line color indicates wind direction and line style represents magnitude of wind stress.

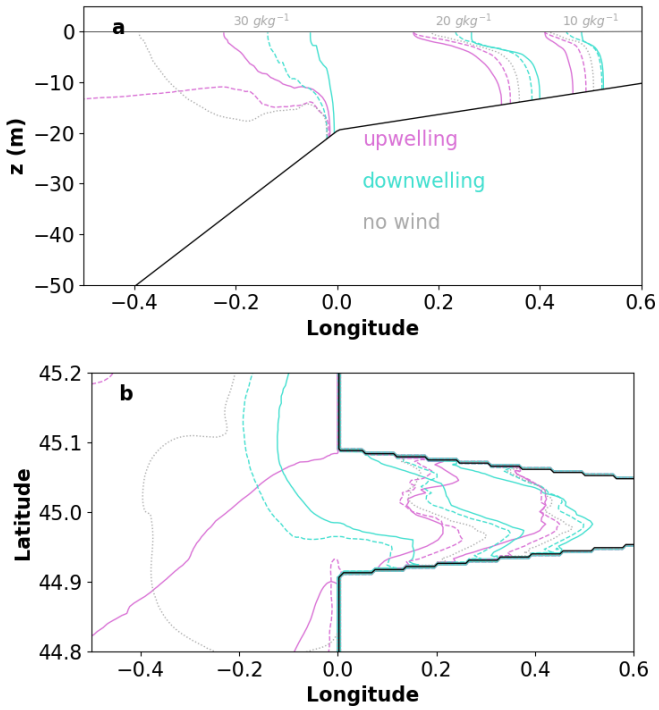

Figure 4.10 Three isohalines (10 g kg^{-1}, 20 g kg^{-1}, 30 g kg^{-1}) plotted in the channel for the five wind experiments, plotting in (a) in profile along a cross-section taken at the thalweg and in (b) at the sea surface.

The inflow drawn into the channel during upwelling-favorable wind stress was fresh relative to the no-wind case (Figure 4.9a and Figure 4.9c), despite increased salinity of inflowing water on the shelf relative to the no-wind case (Figure 4.9e). This suggests that the salt intrusion was shorter under upwelling conditions, a conclusion supported by the distribution of isohaline profiles along the thalweg of the channel (pink lines in Figure 4.10a). A plan view of the isohalines shows the lateral variation in this pattern under different wind conditions: under upwelling-favorable wind stress, the channel was fresher on the south bank and saltier on the north bank relative to the no-wind and downwelling experiments (Figure 4.10b). As Chao (1988) described, upwelling-favorable wind advected outflow to its left, opposing the Coriolis tendency to move the outflow to its right. The relatively down-estuary position of isohalines in the

upwelling experiments may also have been the result of offshore Ekman transport, either acting within the channel to move water down-estuary or as a remote response to the lowered sea surface on the shelf. The lowered sea surface did extend into the mouth of the estuary during the strong upwelling experiment, strengthening the along-estuary sea surface gradient (Figure 4.5a). This may also have been true in the weak upwelling experiment, but the effect is subtler (Figure 4.5b).

Inflow was saltier during downwelling conditions throughout the channel (Figure 4.9a and Figure 4.9c), suggesting that salinity intruded farther up-estuary during downwelling conditions. This was supported by the distribution of isohalines at the thalweg, the deepest cross section of the channel (Figure 4.10a). This result is similar to an observational result from the Choptank river, a tributary of Chesapeake Bay, wherein downwelling-favorable winds lengthened the salt intrusion (Sanford and Boicourt, 1990). Despite being saltier along the thalweg, in plan view it appears that the estuary was much fresher on the north wall relative to the other experiments (Figure 4.10b). In general, the downwelling experiments resulted in a much stronger cross-estuary salinity gradient; inflow and outflow were more segregated along the cross-estuary axis. This was because wind advection reinforced the movement of the outflow by the Coriolis force towards the north wall. In addition to the salinity gradient, there was an enhancement of the cross-estuary sea surface height gradient (Figure 4.5d and Figure 4.5e).

4.4 DISCUSSION

4.4.1 *Width of inflow current*

The results in these model simulations of estuarine inflow supported the hypotheses from the analytical Masse (1990) model. When there was an alongshore current, estuarine inflow originated in the alongshore current. Further, the particle tracking results supported the existence of an offshore limit, x_0, of the inflow current that scaled inversely with the square root of the speed of the alongshore current, $|v_0|^{-1/2}$. The experiments with stronger wind stress produced faster alongshore currents with subsequently thinner inflow streams, while the weaker wind stress experiments produced slower alongshore currents with wider inflow streams. Eq (Chapter 4.1) with the seafloor bathymetry of this model is written

$$Q_{in} = |v_0| \int_{-x0}^{0} (h_w - \alpha x) dx \qquad \text{(Chapter 4.3)}$$

where h_w is the depth of the coastal wall. Integrating Eq (Chapter 4.3) and solving for x_0 gives the following formula,

$$x_0 = \sqrt{\left(\frac{h_w}{\alpha}\right)^2 + \frac{2Q_{in}}{\alpha|v_0|}} - \frac{h_w}{\alpha} \qquad \text{(Chapter 4.4)}$$

The depth of the coastal wall h_w = 30 m and the slope is α = 0.001 for all cases. The rate of inflow used for this calculation was taken from a cross section across the estuary mouth (Figure 4.9d), Q_{in} = 8000 m^3 s^{-1}. Since there was no major change in the volume of inflow to the channel between the different experiments, a single value can be used for Q_{in}. Eq. Chapter 4.4 for x_0 as a function of v_0 was plotted for values of v_0 = 0.01 ms^{-1} to 0.3 ms^{-1} in the gray dashed line in Figure 4.11.

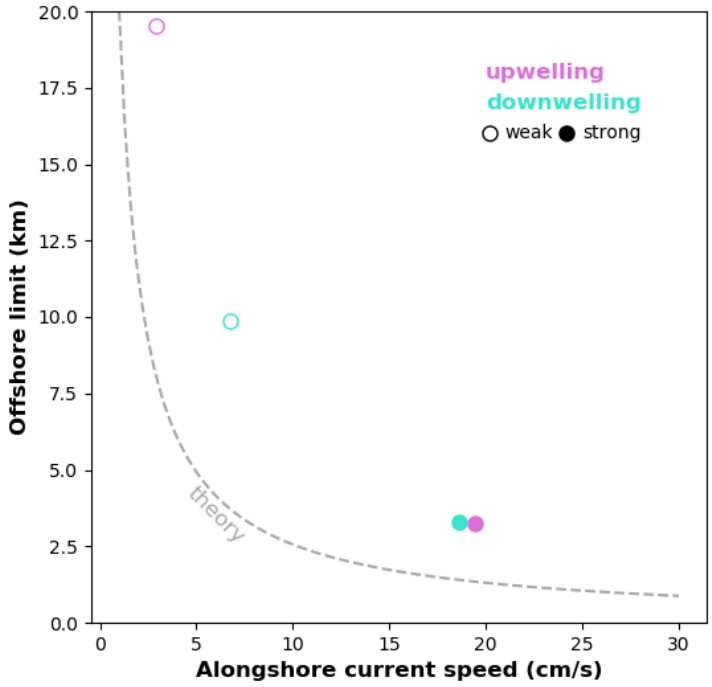

Figure 4.11 Three isohalines (10 g kg^{-1}, 20 g kg^{-1}, 30 g kg^{-1}) plotted in the channel for the five wind experiments, plotting in (a) in profile along a cross-section taken at the thalweg and in (b) at the sea surface.

To compare the model results with Eq (Chapter 4.4), values for x_0 and v_0 were extracted from the four different wind stress experiments. The offshore distance limit was derived from the release points of the particles that reached the estuary. To avoid overweighing outlying particles, the offshore limit was calculated as the 90th percentile of initial offshore position; that is, x_0 iwa calculated such that 90% of particles originate onshore of x_0. To extract the speed of the alongshore current v_0 in the model, the alongshore velocity was averaged at a cross-section from x_0 to the coast. This cross-section was drawn at the mean latitude of the inflowing particles' release points. One x_0, v_0 pair was found for each of the four wind stress experiments; these four points were plotted as colored circles on Figure 4.11.

The model-derived x_0 values were greater than the theoretical predictions for all experiments. However, the curvature of the relationship seems to be correct: as currents increase, the width of the inflow current decreases; the width changes are greater for slower currents than for faster ones.

4.4.2 *Open questions*

Some of the guiding questions in this study were not satisfactorily answered. Firstly, no obvious path from the deep shelf to the estuary was identified during the upwelling-favorable wind stress experiments. Because of the narrowness of the inflow current, the inflowing particles during the strong upwelling experiment all originated in the shallow nearshore region (Figure 4.8a), with the deepest particle originating at a depth of 17 m. This was shallower than the inflowing particle origins in the no-wind (40 m), weak downwelling wind stress (33 m), and weak upwelling wind stress (48 m) experiments (Figure 4.8b, Figure 4.8c, and Figure 4.8d). Even in the strong downwelling wind stress experiment, inflowing particles originated slightly deeper than those in the strong upwelling experiment, with the deepest inflowing particle originating at a depth of 21 m (Figure 4.8e). In the weak upwelling experiment, there did appear to be a preference for particles to move through the bottom boundary layer (Figure 4.8b), but this was not visible in the strong upwelling case. It could have been that the speed of the alongshore current in the strong upwelling case made the slower cross-shore velocities imperceptible except at very large length scales. The nearshore region from which inflowing particles originated in the strong upwelling case did appear to be the saltiest inflow current of the five experiments (Figure 4.3d), which suggests that even though the particle origins were not deep, the water in which they were released was deep at some prior point. However, that heightened salinity signal does not extend

into the estuarine channel, where both upwelling experiments had fresher inflow compared with the downwelling and no-wind experiments (Figure 4.9a). On the other hand, the strong upwelling experiment did produce saltier inflow near the channel mouth (Figure 4.9c). The question of how deep shelf water is transported up the estuarine channel during upwelling-favorable wind stress is still an open one. One hypothesis is that up-estuary transport is diminished during upwelling-favorable winds. If this were the case, intermittency of wind stress would be necessary for up-estuary transport of upwelled water. That is, for deep water to be found up-estuary, a period of upwelling-favorable wind stress would be necessary to bring deep water up to the estuary mouth and subsequent onset of cross-shelf or downwelling-favorable wind stress would be necessary for carrying the upwelled water farther into the channel. Another potential explanation is that the shape of estuaries is important in their response to upwelling. Estuaries in the same region that are subject to the same atmospheric forcing have been observed to have different responses to upwelling events (Hessing-Lewis and Hacker, 2013; Hayduk et al., 2019). Wide and stratified systems, like Mobile Bay (Coogan et al., 2019), are more susceptible to wind stress effects (Scully, 2016). A wide, shallow channel shape may transfer upwelled water up-estuary more effectively than the channel shape used in this idealized model. Further exploration of parameter space, either changing the river flow or the aspect ratio of the channel, could test this hypothesis. Other interesting parameters to test would be the shelf slope or stratification.

The lack of change in the exchange flow in the estuarine channel during alongshore wind stress compared with exchange on the shelf (Figure 4.9b and Figure 4.9d) is another open question. MacCready and Geyer (2010) observe that exchange (surprisingly) varies only with river flow and bathymetry, suggesting that the changes in the estuarine circulation must, as Chao (1988)

found, offset each other. To understand how different wind stress experiments produce the same exchange flow, further work should quantify the changes in the force balance that arose to accommodate wind stress, including the observed changes to the subtidal salinity gradient (Figure 4.10) and the sea surface height tilt (Figure 4.5) in both the along-estuary and cross-estuary directions.

Some insight into the estuarine force balance may be found in the 10-day adjustment period (Figure 4.9). It must be noted that 10 days is a typical length scale for weather event intermittency so a given estuary may never reach the quasi-steady state described in this study. In that case, the estuary would experience upwelling as the fluctuations during the adjustment period, which were glossed over in this analysis. To this end, it would also be interesting to develop a picture of the spin-up of the inflow current from its location beneath the plume in the no-wind case to its position on the opposite side of the estuarine channel from the plume under wind stress. Further examination of this adjustment period would be fruitful for understanding estuarine physics and developing a more realistic picture of the combined estuarine-shelf response to wind.

4.5 CONCLUSIONS

Five experiments were performed to test the effect of wind stress on the source of estuarine inflow in an idealized model. These included weak and strong upwelling-favorable wind stress (τ_y = -0.0025 Pa and τ_y = -0.01 Pa, respectively), weak and strong downwelling-favorable wind stress (τ_y = +0.0025 Pa and τ_y = +0.01 Pa), and a control case with no wind stress. During upwelling-favorable wind stress, inflow was sourced from the right of the estuary, and during

downwelling-favorable wind stress, inflow was sourced from the left of the estuary. This is because inflow is sourced from the alongshore current in the downwind direction induced by the wind stress. Inflow was drawn from a thinner coastal stream during the stronger wind stress experiments. This result is consistent with an analytical result presented in Masse (1990) which suggested that, in the presence of an alongshore current, the offshore extent from which inflow would be drawn was inversely proportional to the square root of the speed of the alongshore current. The theory underestimated the offshore extent from which inflow was sourced for the estuary in the idealized model, but the shape of the theoretical curve seemed correct. The rate of exchange in the estuary was essentially unchanged outside of an initial adjustment period, despite some changes in the salinity distribution in the channel and large changes in the rate of exchange between the plume and the shelf.

Chapter 5. THE SOURCES OF INFLOW TO THE STRAIT OF JUAN DE FUCA UNDER TWO WIND CONDITIONS

5.1 INTRODUCTION

The Salish Sea is a large inland sea shared by the Pacific northwest United States and Canada which has seasonal wind regimes that alternate between being predominately upwelling-favorable in summer and downwelling-favorable in winter (Hickey and Banas, 2003). An estimated 93% of the transport to the Salish Sea from the Pacific Ocean flows through the Strait of Juan de Fuca (Thomson, 1981). The Strait of Juan de Fuca has an accompanying canyon, the Juan de Fuca canyon, that slices across the continental shelf below the mouth of the strait, providing a path for water deeper than the shelf to reach the Salish Sea. Inflow to the Salish Sea has been observed to originate in the Juan de Fuca canyon during upwelling-favorable winds (Alford and MacCready, 2014), and deep water believed to originate below the shelf has been observed in the inland branches of the Salish Sea, including Puget Sound, during the upwelling-favorable wind season (Feeley et al., 2010). This deep Pacific Ocean water has low aragonite saturation state and low pH, which may interfere with the growth of juvenile oyster and krill populations which inhabit Puget Sound (Feeley et al., 2010; McLaskey et al., 2016). Although deep water was observed to pass through the Juan de Fuca canyon during upwelling-favorable winds, it is still unknown, however, whether inflow to the Strait of Juan de Fuca originates in the Juan de Fuca canyon under downwelling-favorable winds. Observations presented in Cannon (1972) suggest that it does not, at least near the seaward end of the canyon at the shelf break. The inflow to the Strait of Juan de Fuca originating outside of the Juan de Fuca canyon has also not yet been described. Because wind stress is hypothesized to be a primary controller of the source of inflow to any estuarine system (Chapter 4), the problem of the source of inflow to the Strait of

Juan de Fuca can begin to be addressed by comparing inflow during one downwelling period with inflow from one upwelling period.

5.2 METHOD

To explore the effect of wind stress on inflow to the Strait of Juan de Fuca, two particle release experiments were performed in a realistic model of the Salish Sea and neighboring Pacific Ocean (Figure 5.1). The first experiment released particles at the beginning of an extended downwelling event for two months in winter of 2017 and the second released particles at the beginning of an extended upwelling event for two months in late spring of 2018 (Figure 5.2). In both experiments, particles were tracked for 60 days. The particle tracking program was the same as that described in previous chapters. Approximately 260,000 particles were released: one particle for every 15 m of depth at 10,000 latitude-longitude pairs, chosen at 100 evenly spaced positions between 47 and 49 N and 100 evenly spaced positions between -126 and -124 E. The particles with release points on land or within the Strait of Juan de Fuca were masked out (Figure 5.1).

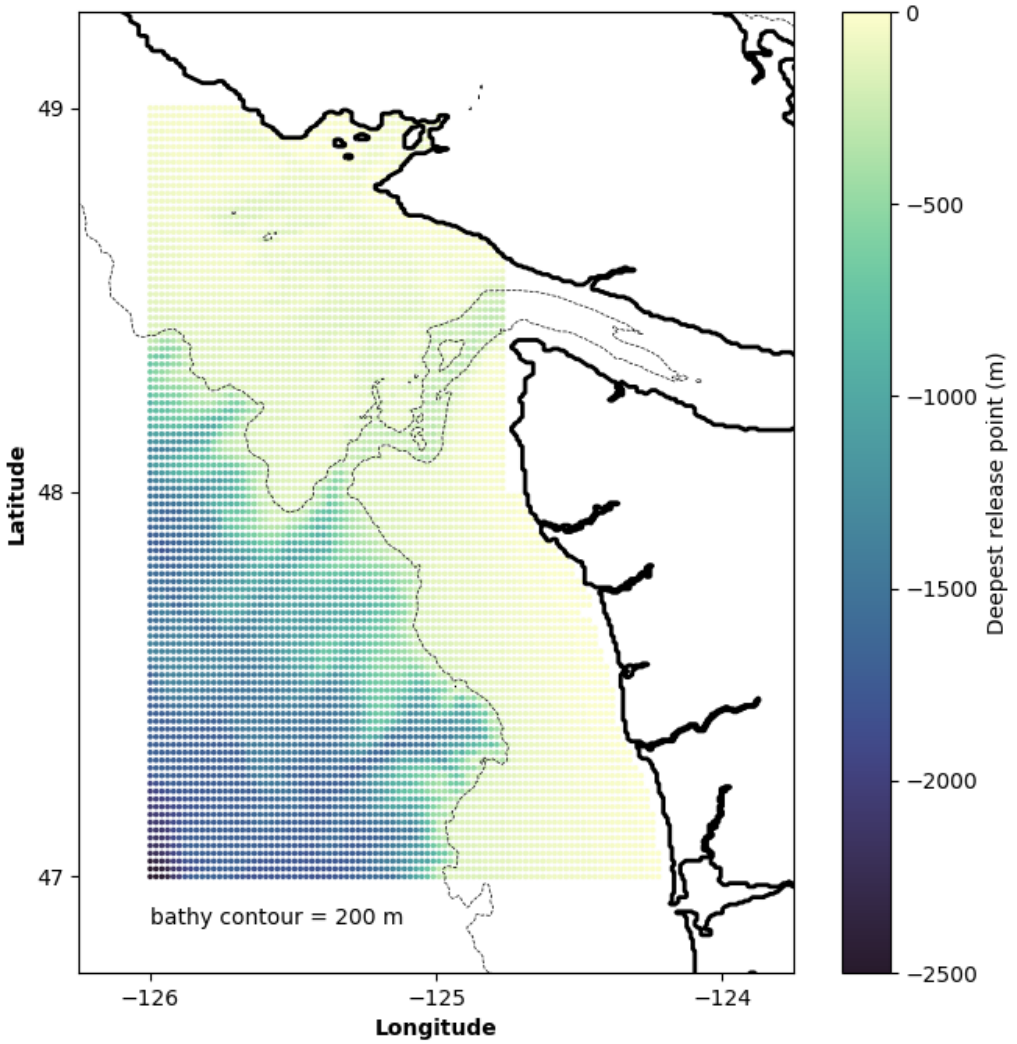

Figure 5.1 Latitude-longitude positions of particle release points. At each position, one particle was released for every 15 m of depth. The colors represent the deepest particle released at each position.

The realistic ocean model used was the LiveOcean model, built using Regional Ocean Modeling System (Shchepetkin & McWilliams, 2005). The model domain included the Salish Sea and all coastal waters of Oregon, Washington, and Vancouver Island. The horizontal resolution was 500 m in most of the Salish Sea and Washington coast, stretched up to 3 km at open boundaries. The model had 30 vertical levels, following the bathymetry and free surface. The model was

configured with realistic forcing, including 45 rivers, 8 tidal constituents, open ocean conditions from a global data-assimilative model, and high-resolution atmospheric forcing from a regional weather forecast model. The three-year model hindcast has been extensively compared to observations.

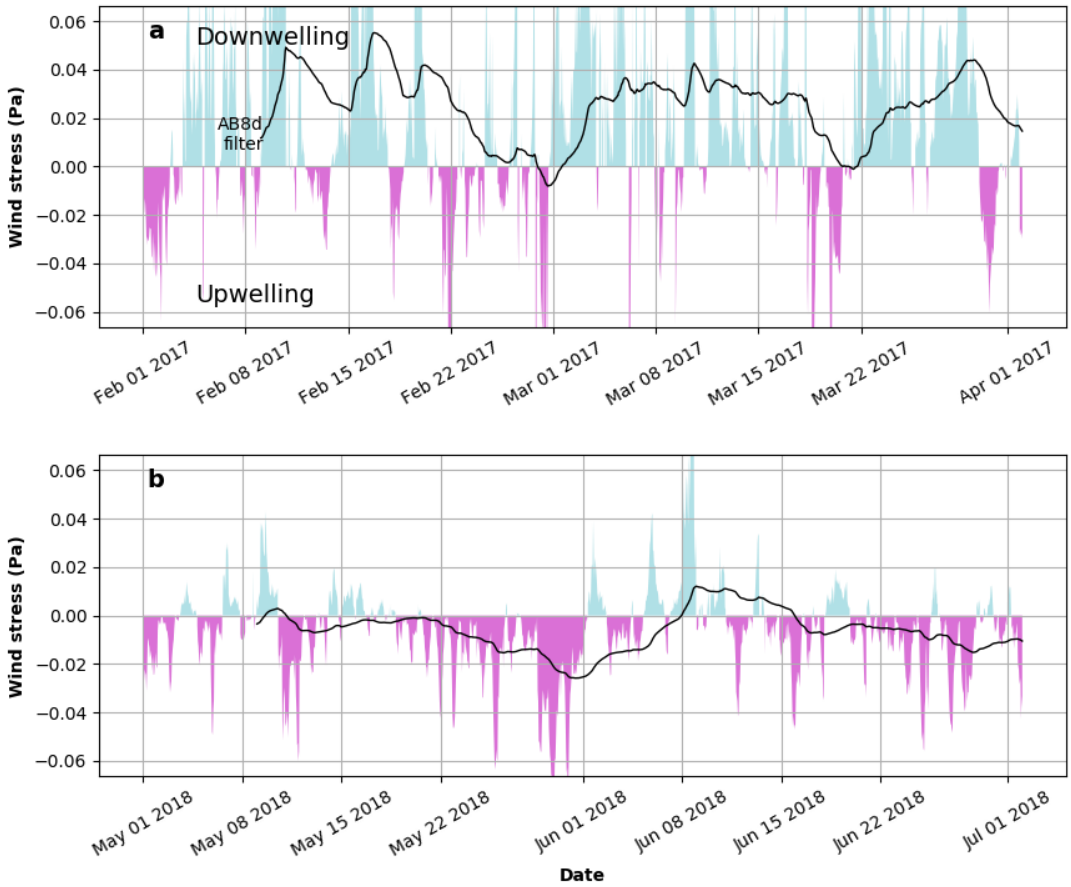

Figure 5.2 Wind stress during (a) the downwelling experiment and (b) the upwelling experiment, displayed as hourly data (color fill) and Austin-Barth 8-day filtered data (black line) (Austin and Barth, 2002).

For the following analysis, inflowing particles were separated into four groups depending on the time it took them to reach the Strait of Juan de Fuca from their release locations. Each group represents a two-week time frame: 0–14 days, 14–28 days, 28–42 days, and 42–56 days. This grouping was done for a few reasons. First, two weeks is a typical weather time scale in this

region, so the initial two-week results can be considered in isolation as the most relevant for most situations. Second, separating by arrival time separated fast paths from slow ones, potentially contrasting dynamics that act on shorter and longer time scales. Third, because the wind was not steady, particles that were in the water for longer experienced a different average wind stress and amount of wind variation. Therefore, dividing the 60-day particle releases into four time frames enabled the extraction of eight wind stress samples from two particle release experiments.

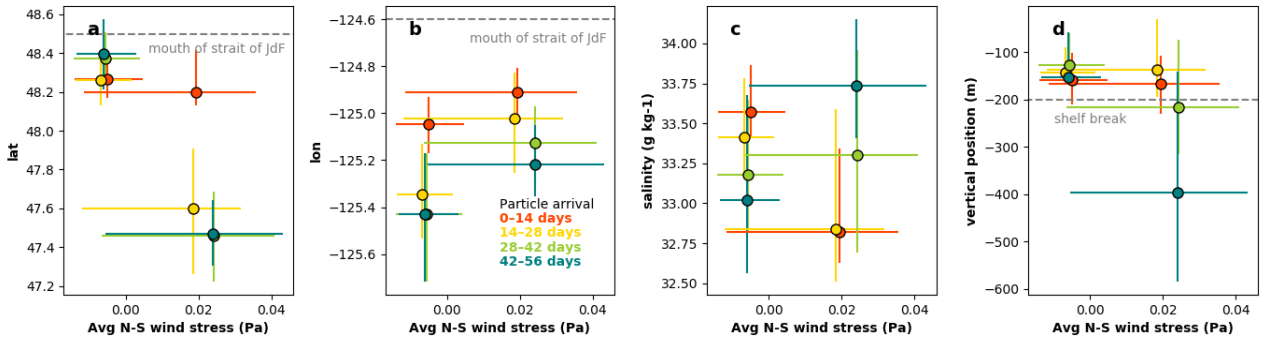

Figure 5.3 Average properties of release points of particles that reached the Strait of Juan de Fuca. Colors indicate the time frame during which they arrived. Colored lines represent the spread from the 25th percentile to the 75th percentile for both axes. Dashed lines indicate useful reference values.

5.3 RESULTS

To understand the source of inflow to the Strait of Juan de Fuca (and ultimately, the Salish Sea), some properties of the initial positions of inflowing particles were compared. These properties were the initial longitude and latitude (together referred to as a particle's "lateral" position), vertical position, and salinity. These properties were plotted against the average wind stress experienced by the particles (*x*-axis of subplots in Figure 5.3) and the time it took for the particles to reach the Strait of Juan de Fuca (indicated by the color of data point in Figure 5.3). Reaching the Strait of Juan de Fuca was defined as passing the longitude -124.05 E while

between the latitudes of 48 and 49 N. The spread of the source properties was also plotted as asymmetric cross hairs indicating the 25th percentile to the 75th percentile of the data (Figure 5.3).

5.3.1 *Inflow properties correlated with wind stress*

The lateral source of inflowing particles was correlated with wind stress. The particles that reached the Strait of Juan de Fuca originated relatively south and east of the strait (i.e. the Washington shelf) during the downwelling-favorable wind experiment. During the upwelling-favorable wind experiment, inflowing particles originated relatively north and west (i.e. the Vancouver Island shelf) compared with the downwelling results, although still south of the mouth of the Strait of Juan de Fuca on average (Figure 5.3a and Figure 5.3b).

The salinity and depth of the inflowing particles were not strictly correlated with wind stress (Figure 5.3c and Figure 5.3d). This seems to challenge the hypothesis that upwelling wind brings deeper, denser water into the Salish Sea. The particles that arrived during the first two periods, 0–14 days and 14–28 days, of the downwelling release were fresher than any of the inflowing particles during the upwelling release. However, the particles that arrived in the later two time frames, 28–42 days and 42–56 days, of downwelling winds were, on average, deeper and saltier than their upwelling counterparts. There was also a larger spread of depths and salinities of inflowing particles during the downwelling experiment than their upwelling counterparts, suggesting that inflow was sourced from diverse water masses during the downwelling period (discussed in section 5.4).

5.3.2 *Inflow properties correlated with arrival time frame*

The average latitude, longitude, and salinity of inflowing particle sources varied monotonically with the length of time it took particles to reach the Strait of Juan de Fuca. For example, in both releases, the particles that reached the Strait of Juan de Fuca in 0–14 days were the easternmost of their release, and subsequent groups originated farther and farther westward (Figure 5.3b). Considering latitude, in both experiments the particles that originated further south arrived later (Figure 5.3a). Salinity trended in opposite directions. The saltiest particles in the downwelling experiment took the longest to arrive, but during the upwelling release, the saltiest particles arrived first (Figure 5.3c). There was no monotonic trend in the vertical positions, although the first two groups, arriving in the 0–14-day time frame and 14–28-day time frame, originated from approximately the same depths in both releases. However, in the downwelling experiment the particles that arrived in the 28–42-day time frame originated on average from below the shelf break, and the particles that arrived after 42 days originated even deeper (Figure 5.3d).

5.4 DISCUSSION

The results of these two experiments supported the Chapter 4 result that inflow originates from up-wind of an estuary. During southerly winds, inflow to the Strait of Juan de Fuca originated from farther south, and during northerly winds, inflow originated from farther north. Interestingly, the Juan de Fuca canyon was populated during both wind experiments. Beyond that, the two experiments form interesting case studies. The results were significantly different, supporting the hypothesis that inflow to the Strait of Juan de Fuca has different properties during different wind regimes. During the downwelling experiment, particles reached the Strait of Juan de Fuca from water with diverse properties (see: longer crosshairs on data points with

downwelling-favorable wind stress in Figure 5.3), suggesting inflow is sourced from diverse water masses. During the upwelling experiment, particles that reached the Strait of Juan de Fuca had less variety in their source water.

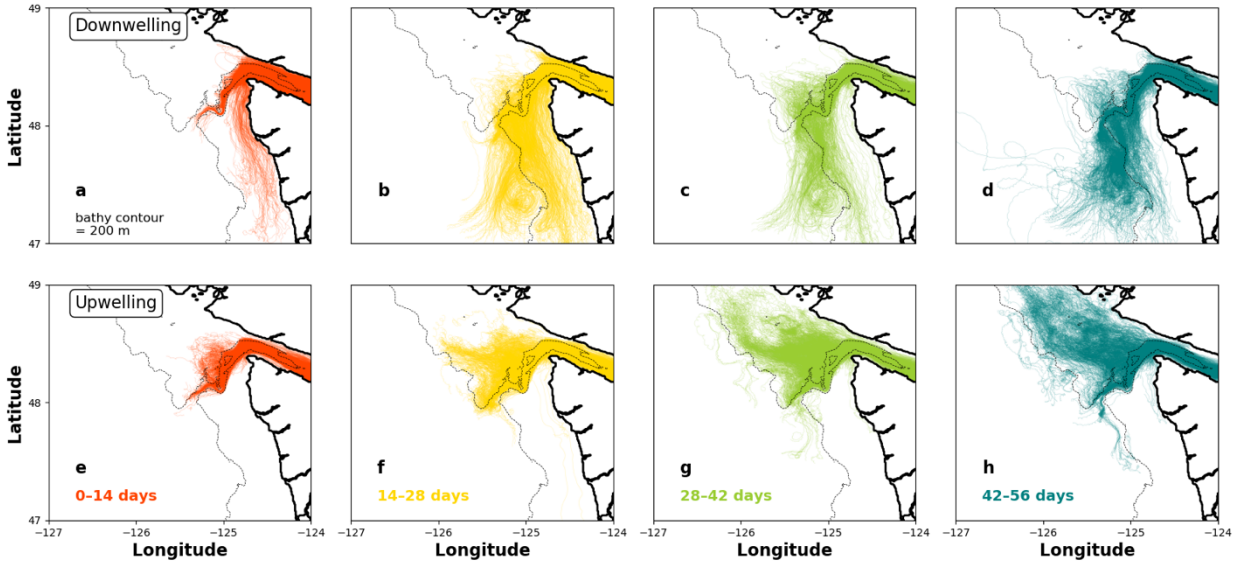

Figure 5.4 Paths of inflowing particles during the two experiments (rows), separated out by the time frame in which they arrive (columns, color).

5.4.1 *Speculated sources of inflow during the downwelling experiment*

For the downwelling experiment in winter of 2017, the particles that reached the Salish Sea originated from diverse sources south of the Strait of Juan de Fuca. There was a significant difference in the density and depth of the particles arriving in the first two groups, 0–14 days and 14–28 days, and those that arrived in the subsequent two groups, 28–42 days and 42–56 days. The first and second groups of particles were relatively fresh and shallow (from the Columbia river plume and the Juan de Fuca canyon), and the third and fourth groups were relatively salty and deep (from the Washington shelf and beyond the shelf break). 20% of all inflowing particles during the downwelling experiment originate from 400 m or deeper.

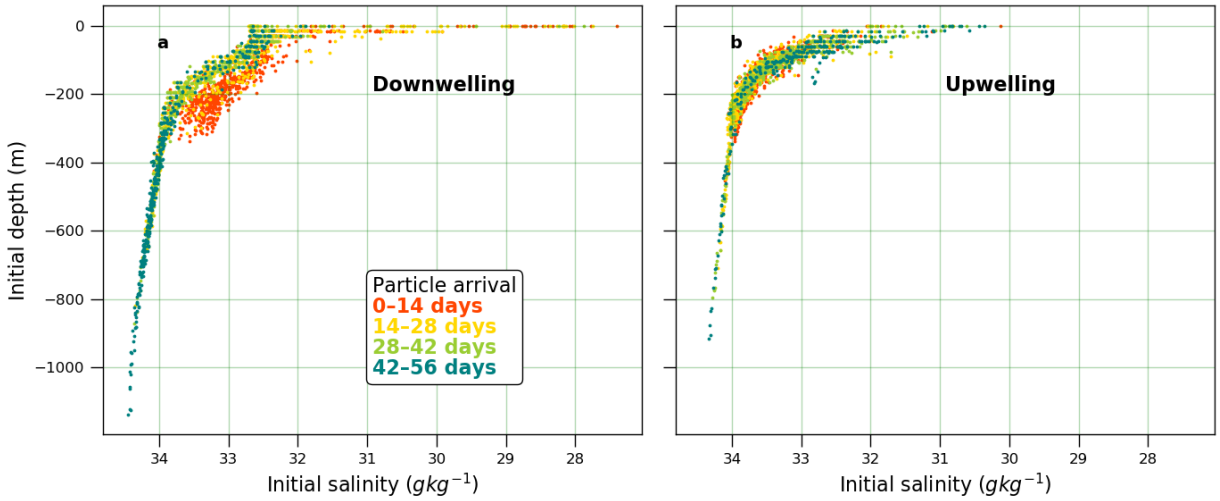

Figure 5.5 Initial salinities and depths of inflowing particles in (a) the downwelling and (b) the upwelling experiments. Particles are colored by the time it took them to reach the Strait of Juan de Fuca from their release points.

The relatively fresh particles that arrived in the first 14-day time frame came from the Columbia River plume and the Juan de Fuca canyon (Figure 5.4a). The Columbia River plume has previously been observed to enter the Strait of Juan de Fuca during downwelling-favorable wind events called “flow reversals” (Thomson et al., 2007; Giddings and MacCready, 2017). The Columbia River plume was contained on the shelf well above the 200 m isobath contour – the plume signal is likely the scattered points in the upper 30 m that are fresher than 31 g kg^{-1} (Figure 5.5a). The relatively fresh particles of depths from 100–300 m that arrived in the first group (anomalous red cluster in Figure 5.5a) must have been sourced from the Juan de Fuca canyon, since those were the only particle tracks that originated below the 200-m shelf break in that group (Figure 5.4a). It follows that the particles that originated in Juan de Fuca canyon during downwelling winds were notably fresh — at least 0.5 g kg^{-1} fresher than Juan de Fuca canyon water during upwelling (Figure 5.5b). Those particles were also fresher than the water at

similar depths that arrives later in the downwelling experiment from the shelf and below the shelf break (green and teal in Figure 5.5a).

The particles that arrived in the two late downwelling groups (arriving in either the 28–42-day or 42–56-day time frame) all originated from the outer Washington shelf or beyond the shelf break (Figure 5.4c and Figure 5.4d). There appeared to be a 100-m mixed layer on the Washington shelf because all particles that originated in the upper 100 m had a salinity around 32.5 g kg^{-1} (Figure 5.5a). The deepest and saltiest particles that reached the Strait of Juan de Fuca arrived in these two time frames. The particles tracks indicated the presence of an anticyclonic eddy just beyond the shelf break (Figure 5.4b–d), perhaps enabling the transport of deep, open ocean water onshore and eventually into the Salish Sea. Such onshore transport of open ocean water by shelf break eddies is described in Cherian and Brink (2019).

Sources of inflow during the upwelling event

For the upwelling experiment in the late spring of 2018, particles that reached the Strait of Juan de Fuca were sourced consistently from the Juan de Fuca canyon and the Vancouver Island shelf. At least 75% of particles were sourced from the shelf (defined here as above the 200-m isobath) in all but the group arriving in the first 14 days (Figure 5.3c). This appears to be because the group that arrived in the first 14 days includes Juan de Fuca canyon water (Fig. 4e), but even in that 0–14-day time frame, at least 50% of particles were sourced from above the shelf break. Evidence of the California Undercurrent may be seen in the particles that originated below the shelf break. The California Undercurrent is a relatively oxygen-depleted, warm, and salty current found below the Washington shelf break in the summertime, traveling poleward beneath the

faster, equatorward California Current at the surface (Hickey, 1979; Thomson and Krassovski, 2010). The California Undercurrent is evident in a few particles that entered the base of the canyon coming from the south and particles that travelled north before being upwelled to the shelf where they reversed direction (Figure 5.4f–h). The particles that originated between depths of 400 m and 1000 m accounted for only 5% of all inflowing particles in the upwelling experiment (visible in Figure 5.5b).

Future work

Upwellings winds are understood to bring deep, hypoxic water into estuaries, but in these experiments, the deepest water arrived during downwelling-favorable winds. One explanation is that wind stress is only one of many factors that determine the source of Salish Sea inflow. Based on the divergence in the downwelling results between the particles that arrived within 28 days and those that arrived later, it is hypothesized that wind stress was important on time scales of two to four weeks, and larger scale dynamics became important on longer time scales. Such larger scale dynamics would include the seasonal variations of the northern California Current System, such as the northward wintertime Davidson Current (Hickey and Banas, 2003). More experiments in the Live Ocean model would help identify which aspects of Salish Sea inflow and which time scales are most influenced by wind stress.

Future work should also report the dissolved oxygen (DO) content of inflowing particle origins. The source depth of inflow is mostly of interest as a proxy for DO. However, DO in the bottom water of the Vancouver Island and Washington shelves is highly seasonal, being especially depleted in the summertime beneath the Juan de Fuca eddy (Crawford and Peña, 2013). It could

be that the inflow to the Strait of Juan de Fuca is more hypoxic under upwelling winds even though its source is shallower than its downwelling counterpart because it originates from the DO-depleted summertime Vancouver Island shelf bottom water. This hypothesis could be explored by tracking biogeochemical properties along with particle position and velocity.

5.5 CONCLUSIONS

Two particle tracking experiments were performed in a realistic model of the Salish Sea and neighboring Pacific Ocean to determine the sources of inflow to the Strait of Juan de Fuca. One experiment was performed during a 60-day period of downwelling-favorable winds in winter of 2017 and the other was performed during a 60-day period of upwelling-favorable winds in late spring of 2018. In both experiments, inflow was sourced laterally from the up-wind direction. That is, inflow was sourced from farther south during the experiment with downwelling winds and farther north during the experiment with upwelling winds. This supports a main result from Chapter 4. The Juan de Fuca canyon was a source of deep inflow in both experiments, suggesting submarine canyons may be an important conduit of inflow under all wind stress conditions. The time it took for particles to reach the Strait of Juan de Fuca from their source point was considered. In the downwelling experiment, particles that arrived within 28 days of release were fresh and shallow compared with particles that arrived later than 28 days after release, which originated in distinctly deep, salty water from the outer shelf and below the shelf break. In the upwelling experiment, arrival time did not have a similarly dramatic effect on the sources of inflowing particles, which consistently came from the Juan de Fuca canyon and the Vancouver Island shelf. Regardless, the downwelling result suggested that time scale may be an important consideration for understanding the effect of wind stress on the source of inflow to the Strait of

Juan de Fuca, as other dynamics may become important on time scales longer than 28 days. Further work is needed to isolate the effect of wind stress from coincident seasonal features of Pacific northwest oceanography, to understand the connection between wind stress and hypoxia in the Salish Sea, and to determine whether the Juan de Fuca canyon is a permanent source of inflow to the Strait of Juan de Fuca.

Chapter 6. CONCLUSION

In this thesis, the origin of estuarine inflow in the coastal ocean has been explored in four chapters. Overarching themes include the importance of wind and the journey of estuarine inflow before it reaches the estuarine channel.

Chapter 2 demonstrated the importance of meteorological forcing and timing on the waters that enter the Salish Sea. By trying to recreate the trajectory of a marine invasive species, it also highlighted the potential ecological harm at stake. Particles (programmed to behave like the planktonic green crab larvae which inhabit surface waters) were episodically transported into the eastern Salish Sea from four locations on the west coast with established European green crab populations. Successful transport of particles was found to depend to some extent on the phenomena of flow reversals in the Strait of Juan de Fuca resulting from strong southerly winds carrying the Columbia river plume up the Washington coast.

Chapter 3 found a generic solution for how inflow reaches an estuary in an idealized model with simplified forcing. The forcing included river flow, planetary rotation, and a single-frequency 12-hour tide. Inflow was identified using particle tracking experiments and the calculation of Total Exchange Flow (TEF) (MacCready, 2011). Under this set up, inflow originated primarily from the right of the estuary in an alongshore current in geostrophic balance. The river plume partially overlapped inflow. Where the inflowing current occurred beneath the river plume, thermal wind tilted the plume-shelf interface. Exchange between the plume and the shelf was found to increase monotonically with distance from the freshwater source. The particle tracks revealed some alternative routes for estuarine inflow arising from aspects of the modern model

not included in previous estuarine inflow literature, including plume recirculation and bulge instabilities.

Chapter 4 demonstrated that the result in Chapter 3, wherein the source of inflow was determined by planetary rotation, is overpowered when wind stress is introduced. As in Chapter 3, the source of inflow was identified using particle tracking experiments and the rate of inflow was calculated using TEF. In four alongshore wind stress experiments, inflowing particles originated from the upwind direction of the estuary. The river plume was carried downwind, so inflow and outflow did not overlap when wind stress was present. During weaker wind stresses, inflowing particles originated farther offshore than during stronger wind stresses. When wind stress is initialized, the rate of inflow to the estuarine channel fluctuates for 10 days before returning to its pre-wind value. This channel response is very different from the shelf response, wherein rates of exchange between the plume and the shelf increase without reaching a steady rate.

In 0, the upwind source of inflow observed in Chapter 4 in an idealized model was supported by results in a realistic model of the Salish Sea and the neighboring Pacific Ocean. Two 60-day particle tracking experiments were performed, the first during a period of persistent downwelling-favorable wind stress and the second during a period of persistent upwelling-favorable wind stress. Results suggested that submarine canyons and time scales were important to the sources of inflow. Particles that reached the Strait of Juan de Fuca originated in the Juan de Fuca canyon in both experiments. During the downwelling-favorable wind stress experiment, particles that reached the Strait of Juan de Fuca in the first 28 days originated primarily from the Juan de Fuca canyon or the Columbia river plume, and particles that reached the Strait of Juan de

Fuca after day 28 originated from the Washington shelf and below the shelf break. During the upwelling-favorable wind stress experiment, all inflowing particles originated from the Juan de Fuca canyon and the Vancouver Island shelf. Open questions remain whether these results are representative of typical Salish Sea inflow, and further experiments are necessary to isolate the role of wind stress in these results.

This work contributed to understanding how inflow reaches estuaries both in general and for the Salish Sea in particular. It addressed the steady state solutions as well as the importance of time variance and unusual events. Observations and models in a variety of specific estuaries are necessary to truly generalize this work, as the source of inflow in the absence of forcing (Chapter 3) is clearly capable of being overridden by wind stress (Chapter 4) and is impacted by topographic steering by submarine canyons (Chapter 5). The results in this thesis relied heavily on particle tracking experiments, which need to be ground truthed to verify some of the surprising preliminary results in Chapter 5, especially the very deep source of inflow to the Strait of Juan de Fuca during the downwelling experiment. I hope this dissertation inspires future coastal scientists to continue the exploration of the rich and important topic of estuarine inflow.

REFERENCES

Ahyong, S.T., 2005. Range extension of two invasive crab species in eastern Australia: *Carcinus maenas* (Linnaeus) and *Pyromaia tuberculata* (Lockington). *Marine Pollution Bulletin*, 50: 460–462, doi:10.1016/J.MARPOLBUL.2005.02.003.

Alford, M.H., and P. MacCready, 2014. Flow and mixing in the Juan de Fuca canyon, Washington. *Geophys. Res. Lett.*, 41(5):1608–1615, doi: 10.1002/2013GL058967.

Austin, J.A. and J.A. Barth, 2002. Variation in the position of the upwelling front on the Oregon shelf. *J. Geophys. Res. Oceans*, 107(C11): 1–15, doi: 10.1029/2001JC000858.

Austin, J.A., and S.J. Lentz, 2002. The inner shelf response to wind-driven upwelling and downwelling over sloping topography. *J. Phys. Oceanogr.* 32: 3132–60.

Banas, N.S., B.M. Hickey, P. MacCready, and J.A. Newton, 2004. Dynamics of Willapa Bay: a highly unsteady, partially mixed estuary. *J. Phys. Oceanogr.*, 34: 2413–2427, doi:10.1175/JPO2637.1.

Banas, N.S., P. MacCready, and B.M. Hickey, 2009. The Columbia River plume as cross-shelf exporter and along-coast barrier. *Cont. Shelf Res.*, 29(1): 292–301, doi:10.1016/j.csr.2008.03.011.

Banas, N.S., P.S. Mcdonald, and D.A. Armstrong, 2009. Green crab larval retention in Willapa Bay, Washington: an intensive Lagrangian modeling approach. *Estuaries and Coasts*, 32: 893–905, doi:10.1007/s12237-009-9175-7.

Beardsley, R.C., and J. Hart, 1978. A simple theoretical model for the flow of an estuary onto a continental shelf. *J. Geophys. Res.: Oceans*, 83(C2): 873–883, doi:10.1029/JC083iC02p00873.

Behrens Yamada, S., 2001. *Global invader: the European green crab*. Oregon Sea Grant, Oregon State University, Corvallis, OR, 123 pp.

Behrens Yamada, S., and G.E. Gillespie, 2008. Will the European green crab (*Carcinus maenas*) persist in the Pacific Northwest? *ICES Journal of Marine Science*, 65: 725–729, doi:10.1093/icesjms/fsm191.

Behrens Yamada, S., and P.M. Kosro, 2010. Linking ocean conditions to year class strength of the invasive European green crab, *Carcinus maenas*. *Biological Invasions*, 12: 1791–1804, doi:10.1007/s10530-009-9589-y.

Behrens Yamada, S., A. Randall, W.M. Sletton, 2013. Status of the European green crab in Oregon and Washington estuaries. *Report prepared for the Aquatic Nuisance Species Project, Pacific States Marine Fisheries Commission*. Oregon State University, Corvallis, OR.

Behrens Yamada, S., W.T. Peterson, and M.P. Kosro, 2015. Biological and physical ocean indicators predict the success of an invasive crab, *Carcinus maenas*, in the northern California Current. *Marine Ecology Progress Series*, 537: 175–189, doi:10.3354/meps11431.

Behrens Yamada, S., R.E. Thomson, G.E. Gillespie, and T.C. Norgard, 2017. Lifting barriers to range expansion: the European green crab *Carcinus maenas* (Linnaeus, 1758) enters the Salish Sea. *Journal of Shellfish Research*, 36: 201–208, doi:10.2983/035.036.0121.

Berril, M., 1982. The life cycle of the green crab *Carcinus maenas* at the northern end of its range. *Journal of Crustacean Biology*, 2: 31–39, doi: 10.2307/1548108.

Brasseale, E.A., E.W. Grason, P.S. McDonald, J. Adams, and P. MacCready, 2019. Larval transport modeling support for identifying population sources of European green crab in the Salish Sea. *Estuaries and Coasts*, 42: 1586–1599, doi:10.1007/s12237-019-00586-2.

Bravo, M.A., B. Cameron, and A. Metaxas, 2007. Salinity tolerance in the early larval stages of *Carcinus maenas* (Decapoda, Brachyura), a recent invader of the Bras d'Or Lakes, Nova Scotia, Canada. *Crustaceana*, 80: 475–490.

Burchard, H., K. Bolding, R. Feistel, U. Gräwe, K. Klingbeil, P. MacCready, V. Mohrholz, L. Umlauf, and E.M. van der Lee, 2018. The Knudsen theorem and the Total Exchange Flow analysis framework applied to the Baltic Sea. *Prog. Oceanography*, 165: 268–286, doi: 10.1016/j.pocean.2018.04.004.

Cai, W., A. Santoso, G. Wang, S. Yeh, S. An, K.M. Cobb, M. Collins, E. Guilyardi, F. Jin, J. Kug, M. Lengaigne, M.J. McPhaden, K. Takahashi, A. Timmermann, G. Vecchi, M. Watanabe, and L. Wu, 2015. ENSO and greenhouse warming. *Nature Climate Change*, 5: 849–859, doi:10.1038/nclimate2743.

Cannon, G.A., 1972. Wind effects on currents observed in Juan de Fuca submarine canyon. *J. Phys. Oceanogr.* 2(3): 281–285, doi: 10.1175/1520-0485(1972)002<0281:WEOCOI>2.0.CO;2.

Carlton, J.T., and A.N. Cohen, 2003. Episodic global dispersal in shallow water marine organisms: the case history of the European shore crabs *Carcinus maenas* and *C. aestuarii*. *Journal of Biogeography*, 30: 1809–1820, doi:10.1111/j.1365-2699.2003.00962.x.

Chapman, D.C., 1985. Numerical treatment of cross-shelf open boundaries in a barotropic coastal ocean model. *J. Phys. Oceanogr.*, 15: 1060–1075, doi:10.1175/1520-0485(1985)015<1060:NTOCSO>2.0.CO;2.

Chapman, D.C. and S.J. Lentz, 1994. Trapping of a coastal density front by the bottom boundary layer. *J. Phys. Oceanogr.*, 24: 1464–1479, doi:10.1175/1520-0485(1994)024<1464:TOACDF>2.0.CO;2.

Chao, S., 1988. Wind-driven motion of estuarine plumes. *J. Phys. Oceanogr.* 18:1144–66.

Cherian, D. A., and K. H. Brink, 2019. Shelf flows forced by deep-ocean anticyclonic eddies at the shelf break. *J. Phys. Oceanogr.* 48(5): 1117–1138, doi:10.1175/JPO-D-17-0237.1.

Cohen, A.N., J.T. Carlton, and M.C. Fountain, 1995. Introduction, dispersal and potential impacts of the green crab *Carcinus maenas* in San Francisco Bay, California. *Marine Biology*, 122: 225–237.

Cole, K.L., and R.D. Hetland, 2016. The effects of rotation and river discharge on net mixing in small-mouth Kelvin number plumes. *J. Phys. Oceanogr.*, 46: 1421–1436, doi:10.1175/jpo-d-13-0271.1.

Coogan, J., B. Dzwonkowski, and J. Lehrter, 2019. Effects of coastal upwelling and downwelling on hydrographic variability and dissolved oxygen in Mobile Bay. *J. Geophys. Res. Oceans*, 124: 791–806, doi: 10.1029/2018JC014592.

Crawford, W.R., and M.A. Peña, 2013. Declining Oxygen on the British Columbia Continental Shelf. *Atmosphere-Ocean*, 51(1): 88-103, doi: 10.1080/07055900.2012.753028.

Csanady, G.T., 1978. The arrested topographic wave. *Am. Meteorol. Soc.*, 8: 47–62, doi:0022-3670/78/0047-0062$08.00.

Curtis, L.J.F., D.L. Curtis, H. Matkin, M. Thompson, F. Choi, P. Callow, G.E. Gillespie, T.W.

Therriault, and C.M. Pearce, 2015. Evaluating transfers of harvested shellfish products, from the west to the east coast of Vancouver Island, as a potential vector for European Green Crab (*Carcinus maenas*) and other non-indigenous invertebrate species. *Department of Fisheries and Oceans Canadian Science Advisory Secretariat Research Document* 2015/2016.

Darling, J.A., M.J. Bagley, J. Roman, C.K. Tepolt, and J.B. Geller, 2008. Genetic patterns across multiple introductions of the globally invasive crab genus *Carcinus*. *Molecular Ecology*, 17: 4992–5007. doi:10.1111/j.1365-294X.2008.03978.x.

Davis, K.A., N.S. Banas, S.N. Giddings, S.A. Siedlecki, P. MacCready, E.J. Lessard, R.M. Kudela, and B.M. Hickey, 2014. Estuary-enhanced upwelling of marine nutrients fuels coastal productivity in the U.S. Pacific Northwest. *Journal of Geophysical Research: Oceans*, 119: 8778–8799, doi:10.1002/2014JC010248.

Dawirs, R.R., 1985. Temperature and larval development of *Carcinus maenas* (Decapoda) in the laboratory; predictions of larval dynamics in the sea. *Marine Ecology Progress Series*, 24: 297–302, doi:10.2307/1548108.

Department of Fisheries and Oceans Canada. 2018. Summary of locations in British Columbia, Canada supporting invasive tunicate species and European green crab as of 2017. *Department of Fisheries and Oceans Canada Science Advisory Secretariat Science Response* 2018/047.

DiBacco, C., and T.W. Therriault, 2015. Reproductive periodicity and larval vertical migration behavior of European green crab *Carcinus maenas* in a non-native habitat. *Marine Ecology Progress Series*, 536: 123–134, doi:10.3354/meps11422.

Du, J., and J. Shen, 2014. Decoupling the influence of biological and physical processes on dissolved oxygen in Chesapeake Bay. *J. Geophys. Res. Oceans*, 120(1): 78–93, doi: 10.1002/2014JC010422.

Duxbury, A.C., 1979. Upwelling and estuary flushing. *Limnol. Oceanogr.*, 24(4): 627–633, doi:10.4319/lo.1979.24.4.0627.

Egbert, G.D., and S.Y. Erofeeva, 2002. Efficient inverse modeling of barotropic ocean tides. *Journal of Atmospheric and Oceanic Technology*, 19: 183–204, doi:10.1175/1520-0426(2002)019<0183:EIMOBO>2.0.CO;2.

Elston, R.A., H. Hasegawa, K.L. Humphrey, I.K. Polyak, and C.C. Häse, 2008. Re-emergence of *Vibrio tubiashii* in bivalve shellfish aquaculture: severity, environmental drivers, geographic extent and management. *Dis. Aquat. Org.*, 82: 119–134, doi:10.3354/dao01982.

Feeley, R.A., S.R. Alin, J. Newton, C.L. Sabine, M. Warner, A. Devol, C. Krembs, and C. Maloy, 2010. The combined effects of ocean acidification, mixing, and respiration on pH and carbonate saturation in an urbanized estuary. *Estuar. Coast. Shelf S.*, 88: 442–449, doi: 10.1016/j.ecss.2010.05.004.

Flather, R.A., 1976. A tidal model of the northwest European continental shelf. *Mem. Soc. R. Sci. Liege*, 6: 141–164.

Fong, D.A., and W.R. Geyer, 2001. Response of a river plume during an upwelling favorable wind event. *J. Geophys. Res.: Oceans*, 106(C1): 1067–1084, doi:10.1029/2000JC900134.

Frisch, A.S., J. Holbrook, and A.B. Ages, 1981. Observations of a summertime reversal in circulation in the Strait of Juan de Fuca. *Journal of Geophysical Research: Oceans*, 86: 2044–2048, doi:10.1029/JC086iC03p02044.

Garvine, R.W., 1995. A dynamical system for classifying buoyant coastal discharges. *Cont. Shelf Res.*, 15(13): 1585–1596, doi:10.1016/0278-4343(94)00065-U.

Gawarkiewicz, G., and D.C. Chapman, 1991. Formation and maintenance of shelfbreak fronts in an unstratified flow. *J. Phys. Oceanogr.*, 21: 1225–1239, doi:10.1175/1520-0485(1991)021<1225:FAMOSF>2.0.CO;2.

Geller, J.B., E.D. Walton, E.D. Grosholz, and G.M. Ruiz, 1997. Cryptic invasions of the crab *Carcinus* detected by molecular phylogeography. *Molecular Ecology*, 6: 901–906, doi:10.1046/j.1365-294X.1997.00256.x.

Geyer, W.R., and P. MacCready, 2014. The estuarine circulation. *Annu. Rev. Fluid Mech.*, 46: 175–197, doi:10.1146/annurev-fluid-010313-141302.

Gharouni, A., M.A. Barbeau, J. Chassé, L. Wang, and J. Watmough, 2017. Stochastic dispersal increases the rate of upstream spread: A case study with green crabs on the northwest Atlantic coast. *PLoS ONE* 12: e0185671, doi:10.1371/journal.pone.0185671.

Giddings, S.N., P. MacCready, B.M. Hickey, N.S. Banas, K.A. Davis, S.A. Siedlecki, V.L. Trainer, R.M. Kudela, N.A. Pelland, and T.P. Connolly, 2014. Hindcasts of potential harmful algal bloom transport pathways on the Pacific northwest coast. *J. Geophys. Res.: Oceans*, 119(4): 2439–2461, doi:10.1002/2013JC009622.

Giddings, S.N., MacCready, P., 2017. Reverse estuarine circulation due to local and remote wind forcing, enhanced by the presence of along-coast estuaries. *Journal of Geophysical Research: Oceans*, 122: 10184–10205, doi:10.1002/2016JC012479.

Gillespie, G.E., T.C. Norgard, E.D. Anderson, D.R. Haggarty, and A.C. Phillips, 2015. Distribution and biological characteristics of European green crab, *Carcinus maenas*, in British Columbia, 2006-2013. *Canadian Technical Report of Fisheries and Aquatic*

Sciences 3120.

Godin, G., 1972. *The analysis of tides*. University of Toronto Press, 264 p.

Grason, E.W., P.S. McDonald, J. Adams, K. Litle, J.K. Apple, and A. Pleus, 2018. Citizen science program detects range expansion of the globally invasive European green crab in Washington State (USA). *Management of Biological Invasions*, 9: 39–47, doi:10.3391/mbi.2018.9.1.04.

Griffen, B.D., 2014. Linking individual diet variation and fecundity in an omnivorous marine consumer. *Oecologia*, 174: 121-130, doi: 10.1007/s00442-013-2751-3.

Grosholz, E.D., 2005. Recent biological invasion may hasten invasional meltdown by accelerating historical introductions. *Proceedings of the National Academy of Sciences of the United States of America*, 102: 1088–91, doi:10.1073/pnas.0308547102.

Grosholz, E.D., and G.M. Ruiz, 1995. Spread and potential impact of the recently introduced European green crab, *Carcinus maenas*, in central California. *Marine Biology*, 122: 239–247, doi:10.1007/bf00348936.

Grosholz, E.D., G.M. Ruiz, C.A. Dean, K.A. Shirley, J.L. Maron, and P.G. Connors, 2000. The impacts of a nonindigenous marine predator in a California bay. *Ecology*, 81: 1206–1224, doi:10.1890/0012-9658(2000)081[1206:TIOANM]2.0.CO;2.

Hayduk, J.L., S.D. Hacker, J.S. Henderson, and F. Tomas, 2019. Evidence for regional-scale controls on eelgrass (*Zostera marina*) and mesograzer community structure in upwelling-influenced estuaries. *Limnol. Oceanogr.*, 64: 1120–1134, doi: 10.1002/lno.11102.

Hench, J.L., and R.A. Luettich, 2003. Transient tidal circulation and momentum balances at a shallow inlet. *J. Phys. Oceanogr.*, 33: 913–932.

Hessing-Lewis, M.L., and S.D. Hacker, 2013. Upwelling-influence, macroalgal blooms, and seagrass production; temporal trends from latitudinal and local scales in northeast Pacific estuaries. *Limnol. Oceanogr.* 58: 1103–1112, doi:10.4319/lo.2013.58.3.1103.

Hickey, B.M., 1979. The California Current system: Hypotheses and facts. *Prog. Oceanogr.* 8: 191–279, doi: 10.1016/0079-6611(79)90002-8.

Hickey, B.M., and N.S. Banas, 2003. Oceanography of the U.S. Pacific northwest coastal ocean and estuaries with application to coastal ecology. *Estuaries,* 26(4B): 1010–1031.

Hickey, B., S. Geier, N. Kachel, and A. MacFadyen, 2005. A bi-directional river plume: The Columbia in summer. *Cont. Shelf Res.*, 25: 1631–1656, doi:10.1016/j.csr.2005.04.010.

Hidalgo, F.J., P.J. Barón, J.M. Orensanz, 2005. A prediction come true: the green crab invades the Patagonian coast. *Biological Invasions*, 7: 547–552, doi:10.1007/s10530-004-5452-3.

Horner-Devine, A.R., R.D. Hetland, and D.G. MacDonald, 2015. Mixing and Transport in Coastal River Plumes. *Annu. Rev. Fluid Mech.*, 47: 569–594, doi: 10.1146/annurev-fluid-010313-141408.

Hulme, P. E., 2009. Trade, transport and trouble: managing invasive species pathways in an era of globalization. *Journal of Applied Ecology*, 46: 10–18, doi:10.1111/j.1365-2664.2008.01600.x.

Infantes, E., C. Crouzy, and P. Moksnes, 2016. Seed predation by the shore crab *Carcinus maenas*: a positive feedback preventing eelgrass recovery? *PLoS ONE* 11: e0168128, doi:10.1371/journal.pone.0168128.

Jackson, R.H., J.D. Nash, C. Kienholz, D.A. Sutherland, J.M. Amundson, R.J. Motyka, D. Winters, E. Skyllingstad, and E.C. Pettit, 2019. Meltwater intrusions reveal mechanisms

for rapid submarine melt at a tidewater glacier. *Geophys. Res. Lett.*, 47: e2019GL085335, doi: 10.1029/2019GL085335.

Jamieson, G. S., M.G.G. Foreman, J. Cherniawsky, and C.D. Levings, 2002. European green crab (*Carcinus maenas*) dispersal: The Pacific experience. In: Paul, A. J., E.G. Dawe, R. Elner, G.S. Jamieson, G.H. Kruse, R.S. Otto, B. Sainte-Marie, T.C. Shirley, and D. Woodby (Eds.), *Crabs in Cold Water Regions: Biology, Management, and Economics*. Alaska Sea Grant College Program, Fairbanks, AK, pp. 561–576, doi:10.4027/ccwrbme.2002.41.

Jia, Y., and A.E. Yankovsky, 2012. The impact of ambient stratification on freshwater transport in a river plume. *J. Mar. Res.*, 70: 69–92, doi:10.1357/002224012800502408.

Jurisa, J.T., and R. Chant, 2012. The coupled Hudson River estuarine-plume response to variable wind and river forcings. *Ocean Dynam.* 62: 771–784, doi: 10.1007/s10236-012-0527-7.

Kemp, W.M., J.M. Testa, D.J. Conley, D. Gilbert, and J.D. Hagy, 2009. Temporal responses of coastal hypoxia to nutrient loading and physical controls. *Biosciences*, 6: 2985–3008, doi: 10.5194/bg-6-2985-2009.

Kimbro, D. L., E.D. Grosholz, A.J. Baukus, N.J. Nesbitt, N.M. Travis, S. Attoe, and C. Coleman-Hulbert, 2009. Invasive species cause large-scale loss of native California oyster habitat by disrupting trophic cascades. *Oecologia*, 160: 563–575, doi:10.1007/s00442-009-1322-0.

Klassen, G., and A. Locke, 2007. A biological synopsis of the European green crab, *Carcinus maenas*. *Canadian Manuscript Report of Fisheries and Aquatic Sciences* 2818.

Knudsen, M., 1900. Ein hydrographischer Lehrsatz. *Hydrogr. Mar. Meteorol.*, 28(7): 316–320.

Lentz, S.J., 2004. The response of buoyant coastal plumes to upwelling-favorable winds. *J. Phys. Oceanogr.*, **34**, 2458–2469, doi: 10.1175/JPO2647.1.

Lentz, S.J., and M.R. Fewings, 2012. The wind- and wave-driver inner-shelf circulation. *Annu. Rev. Mar. Sci.* 4: 317–43, doi: 10.1146/annurev-marine-120709-142745.

Lentz, S.J., and K.R. Helfrich, 2001. Buoyant gravity currents along a sloping bottom in a rotating fluid. *J. Fluid Mech.*, 464: 251–278, doi:10.1017/S0022112002008868.

Lindley, J. A., 1987. Continuous plankton records: the geographical distributions and seasonal cycles of decapod crustacean larvae and pelagic post-larvae in the north-eastern Atlantic Ocean and the North Sea, 1981–83. *Journal of Marine Biological Association of the United Kingdom*, 67: 145–167, doi:10.1017/S0025315400026424.

Lorenz, M., K. Klingbeil, P. MacCready, and H. Burchard, 2019. Numerical issues of the Total Exchange Flow (TEF) analysis framework for quantifying estuarine circulation. *Ocean Sci.*, 15(3): 601–614, doi: 10.5194/os-15-601-2019.

MacCready, P., 2011. Calculating estuarine exchange flow using isohaline coordinates. *J. Phys. Oceanogr.*, 41: 1116–1124, doi:10.1175/2011JPO4517.1.

MacCready, P., and W.R. Geyer, 2010. Advances in estuarine physics. *Annu. Rev. Mar. Sci.*, 2: 35–58, doi: 10.1146/annurev-marine-120308-081015.

MacCready, P., W.R. Geyer, and H. Burchard, 2018. Estuarine exchange flow is related to mixing through the salinity variance budget. *J. Phys Oceanogr.* 48(6): 1375–1384, doi: 10.1175/JPO-D-17-0266.1.

Malyshev, A., and P.A. Quijon, 2011. Disruption of essential habitat by a coastal invader: new evidence of the effects of green crabs on eelgrass beds. *International Council Exploration of the Sea Journal of Marine Science*, 68: 1852–1856, doi:10.1093/icesjms/fsr126.

Margules, M., 1906. Zur Sturmtheorie. *Meteorol. Z.*, 23(11): 481–497.

Mass, C. F., M. Albright, D. Ovens, R. Steed, M. Maciver, E. Grimit, T. Eckel, B. Lamb, J. Vaughan, K. Westrick, P. Storck, B. Colman, C. Hill, N. Maykut, M. Gilroy, S.A. Ferguson, J. Yetter, J.M. Sierchio, C. Bowman, R. Stender, R. Wilson, and W. Brown, 2003. Regional environmental prediction over the Pacific Northwest. *Bulletin of the American Meteorological Society*, 84: 1353–1366, doi:10.1175/BAMS-84-10-1353.

Masse, A.K., 1990. Withdrawal of shelf water into an estuary: a barotropic model. *J. Geophys. Res*. 95(C9): 16,085–96.

Matheson, K., C.H. McKenzie, R.S. Gregory, D.A. Robichaud, I.R. Bradbury, P.V.R. Snelgrove, and G.A. Rose, 2016. Linking eelgrass decline and impacts on associated fish communities to European green crab *Carcinus maenas* invasion. *Marine Ecology Progress Series*, 548: 31–45, doi:10.3354/meps11674.

McCabe, R.M., P. MacCready, and B.M. Hickey, 200.: Ebb-tide dynamics and spreading of a large river plume. *J. Phys. Oceanogr.*, 39: 2839–2856, doi: 10.1175/2009JPO4061.1.

McLaskey, A.K., J.E. Keister, P. McElhany, M.B. Olson, D.S. Busch, M. Maher, and A.K. Winans, 2016. Development of *Euphausia pacifica* (krill) larvae is impaired under pCO_2 levels currently observed in the Northeast Pacific. *Mar. Ecol. Prog. Ser.*, 555: 65–78, doi: 10.3354/meps11839.

Mileikovsky, S.A., 1973. Speed of active movement of pelagic larvae of marine bottom invertebrates and their ability to regulate their vertical position. *Marine Biology*, 23: 11–17. doi:10.1007/ BF00394107.

Mofjeld, H.O., and L.H. Larsen, 1984. Tides and Tidal Currents of the Inland Waters of Western Washington. National Oceanic and Atmospheric Administration Technical Memo. ERL

PMEL-56, Pacific Marine Environmental Laboratory, NOAA.

Nagaraj, M., 1993. Combined effects of temperature and salinity on the zoeal development of the green crab, *Carcinus maenas* (Linnaeus, 1758) (Decapoda, Portunidae). *Scientia Marina*, 57: 1–8.

Narberhaus, I., 2019. Species profile: *Carcinus maenas*. *Global Invasive Species Database*. http://www.iucngisd.org/gisd/species.php?sc=114. Accessed on 24 February 2019.

Nash, J.D., L.F. Kilcher, and J.N. Moum, 2009. Structure and composition of a strongly stratified, tidally pulsed river plume. *Journal of Geophysical Research*, 114: 1–16. CB0012, doi:10.1029/2008JC005036.

Neckles, H. A., 2015. Loss of eelgrass in Casco Bay, Maine, linked to green crab disturbance. *Northeastern Naturalist*, 22: 478–500, doi:10.1656/045.022.0305.

Pawlowicz, R., O. Riche, and M. Halverson, 2006. The circulation and residence time of the strait of Georgia using a simple mixing-box approach. *Atmos.-Ocean*, 45(4): 173–193, doi:10.3137/ao.450401.

Peterson, J.O., and W.T. Peterson, 2009. Influence of the Columbia River plume on cross-shelf transport of zooplankton. *Journal of Geophysical Research*, 114: 1–11, doi:10.1029/2008JC004965.

Pineda, J., J. Hare, and S. Sponaugle, 2007. Larval transport and dispersal in the coastal ocean and consequences for population connectivity. *Oceanography*, 20: 22–39, doi:10.5670/oceanog.2007.27.

Pringle, J.M., A.M.H. Blakeslee, J.E. Byers, and J. Roman, 2011. Asymmetric dispersal allows an upstream region to control population structure throughout a species' range.

Proceedings of the National Academy of Sciences, 108: 15288–15293, doi:10.1073/pnas.1100473108.

Queiroga, H., 1996. Distribution and drift of the crab *Carcinus maenas* (L.) (Decapoda, Portunidae) larvae over the continental shelf off northern Portugal in April 1991. *Journal of Plankton Research*, 18: 1981-2000, doi:10.1093/plankt/18.11.1981

Queiroga, H., J.D. Costlow, and M.H. Moreira, 1994. Larval abundance patterns of *Carcinus maenas* (Decapoda, Brachyura) in Canal de Mira (Ria de Aveiro, Portugal). *Marine Ecology Progress Series*, 111: 63–72, doi:10.3354/meps111063.

Queiroga, H., J.D. Costlow, and M.H. Moreira, 1997. Vertical migration of the crab *Carcinus maenas* first zoea in an estuary: implications for tidal stream transport. *Marine Ecology Progress Series*, 149: 121–132, doi:10.3354/meps149121.

Queiroga, H., P. Moksnes, and S. Meireles, 2002. Vertical migration behaviour in the larvae of the shore crab *Carcinus maenas* from a microtidal system (Gullmarsfjord, Sweden). *Marine Ecology Progress Series*, 237: 195–207, doi:10.3354/meps237195.

Ralston, D.K., W.R. Geyer, and J.A. Lerczak, 2007. Subtidal salinity and velocity in the Hudson River estuary: observations and modeling. *J. Phys. Oceanogr.* 38: 753–770, doi: 10.1175/2007JPO3808.1.

Reynolds-Fleming, J.V., and R.A. Luettich Jr., 2004. Wind-driven lateral variability in a partially mixed estuary. *Estuar. Coast. Shelf S.*, 60: 395–407, doi:10.1016/j.ecss.2004.02.003.

de Rivera, C.E., N.G. Hitchcock, S.J. Teck, B.P. Steves, A.H. Hines, and G.M. Ruiz, 2007. Larval development rate predicts range expansion of an introduced crab. *Marine Biology*, 150: 1275–1288, doi:10.1007/s00227-006-0451-9.

de Rivera, C.E., E.D. Grosholz, and G.M. Ruiz, 2011. Multiple and long-term effects of an

introduced predatory crab. *Marine Ecology Progress Series*, 429: 145–155, doi:10.2307/24874481.

Roegner, G.C., B.M. Hickey, J.A. Newton, A.L. Shanks, and D.A. Armstrong, 2002. Wind-induced plume and bloom intrusions into Willapa Bay, Washington. *Limnol. Oceanogr.* 47(4): 1033–1042, doi: 10.4319/lo.2002.47.4.1033.

Roegner, G.C., J.A. Needoba, and A.M. Baptista, 2011. Coastal upwelling supplies oxygen-depleted water to the Columbia river estuary. *PLoS One*, 6(4): e18672, doi:10.1371/journal.pone.0018672.

le Roux, P.J., G.M. Branch, and M.A.P. Joska, 1990. On the distribution, diet and possible impact of the invasive European shore crab *Carcinus maenas* (L.) along the South African coast. *South African Journal of Marine Science*, 9: 85–93, doi:10.2989/025776190784378835.

Sanford, L.P., and W.C. Boicourt, 1990. Wind-forced salt intrusion into a tributary estuary. *J. Geophys. Res. Oceans,* 95(C8): 13357–13371, doi:10.1029/JC095iC08p13357.

Schroeder, W.W. and W.J. Wiseman Jr., 1988. The Mobile Bay estuary: stratification, oxygen depletion, and jubilees. In B. Kjerfve (ed.): *Hydrodynamics of estuaries*. CRC Press, Boca Raton, 41–52.

Scully, M.E., 2016. Mixing of dissolved oxygen in Chesapeake Bay driven by the interaction between wind-driven circulation and estuarine bathymetry. *J. Geophys. Res. Oceans*, 121(8): 5639–5654, doi: 10.1002/2016JC011924.

Shanks, A., S.L. Schroeder, and B.L. Dlouhy, 2011. January 2011: Report on the zooplankton sampling adjacent to the proposed Jordan Cove Liquid Natural Gas (LNG) terminal. Oregon Institute of Marine Biology. Charleston, Oregon. (Note: This report was provided

as Appendix F.3 to Resource Report 3 in the May 2013 filing.)

Shchepetkin, A.F., and J.C. McWilliams, 2005. The regional ocean modeling system (ROMS): a split-explicit, free-surface, topography-following-coordinate oceanic model. *Ocean Modeling*, 9: 347–404, doi:10.1016/j.ocemod.2004.08.002.

Siedlecki, S.A., N.S. Banas, K.A. Davis, S.N. Giddings, B.M. Hickey, P. MacCready, T.P. Connolly, and S. Geier, 2015. Seasonal and interannual oxygen variability on the Washington and Oregon continental shelves. *Journal of Geophysical Research: Oceans*, 120: 608–633, doi:10.1002/2014JC010254.

Soulsby, R.L. 1983. The bottom boundary layer of shelf seas. In Johns, B. (ed) *The physical oceanography of coastal and shelf seas*. Amsterdam: Elsevier Science Publishers B.V., 189–266. doi: 10.1016/S0422-9894(08)70503-8.

Sponaugle, S., R.K. Cowen, A. Shanks, S.G. Morgan, J.M. Leis, J. Pineda, G.W. Boehlert, M.J. Kingsford, K.C. Lindeman, C. Grimes, and J.L. Munro, 2002. Predicting self-recruitment in marine populations: Biophysical correlates and mechanisms. *Bulletin of Marine Science*, 70: 341–375.

Sponaugle, S., C. Paris, K.D. Walter, V. Kourafalou, and E. D'Alessandro, 2012. Observed and modeled larval settlement of a reef fish to the Florida Keys. *Marine Ecology Progress Series*, 453: 201–212, doi:10.3354/meps09641.

Sprung, M., 2001. Larval abundance and recruitment of *Carcinus maenas* L. close to its southern geographic limit: a case of match and mismatch. *Advances in Decapod Crustacean Research*. Developments in Hydrobiology, 449: 153–158, doi:10.1007/978-94-017-0645-2_16.

Sutherland, D.A., and F. Straneo, 2012, Estimating ocean heat transports and submarine melt rates in Sermilik Fjord, Greenland using acoustic Doppler current profiler (ADCP) velocity profiles. *Ann. Glaciol.*, 53(60): 50–58, doi:10.3189/2012AoG60A050.

Thomson, R.E., 1981. *Oceanography of the British Columbia Coast*. Canadian Special Publication of Fisheries and Aquatic Sciences, 56: 291.

Thomson, R.E., S.F. Mihály, and E.A. Kulikov, 2007. Estuarine versus transient flow regimes in Juan de Fuca Strait. *Journal of Geophysical Research: Oceans*, 112: 1–25, doi:10.1029/2006JC003925.

Thomson, R.E., and M.V. Krassovski, 2010. Poleward reach of the California Undercurrent. *J. Geophys. Res. Oceans.* 115(C9): 1–9, doi: 10.1029/2010JC006280.

Thresher, R., C. Proctor, G.M. Ruiz, R. Gurney, C. MacKinnon, W. Walton, L. Rodriguez, and N. Bax, 2003. Invasion dynamics of the European shore crab, *Carcinus maenas*, in Australia. *Marine Biology*, 142: 867–876, doi:10.1007/s00227-003-1011-1.

Umlauf, L., and H. Burchard, 2003. A generic length-scale equation for geophysical turbulence models. *J. Mar. Res.*, 61: 235–265, doi:10.1357/002224003322005087.

Valle-Levinson, A., J.M. Klink, and G.H. Wheless, 1996. Inflows/outflows at the transition between a coastal plain estuary and the coastal ocean. *Cont. Shelf Res.*, 16(14): 1819–1847, doi:10.1016/0278-4343(96)00016-7.

Valle-Levinson, A., C. Li, T.C. Royer, and L.P. Atkinson, 1998. Flow patterns at the Chesapeake Bay entrance. *Cont. Shelf Res.*, 18: 1157–1177, doi: 10.1016/s0278-4343(98)00036-3.

Visser, A.W., 1997. Using random walk models to simulate the vertical distribution of particles in a turbulent water column. *Mar. Ecol. Prog. Ser.*, 158: 275–281.

Whitlow, W. L., 2009. Changes in survivorship, behavior, and morphology in native soft-shell

clams induced by invasive green crab predators. *Marine Ecology*, 31: 418–430, doi:10.1111/j.1439-0485.2009.00350.x.

Wong, K. and J.E. Moses-Hall, 1998. On the relative importance of the remote and local wind effects to the subtidal variability in a coastal plain estuary. *J. Geophys. Res.* 103 (C9): 18,393–18,404.

Yankovsky, A.E., and D.C. Chapman, 1997. A simple theory for the fate of buoyant coastal discharges. *J. Phys. Oceanogr.*, 27: 1386–1401, doi:10.1175/1520-0485(1997)027<1386:ASTFTF>2.0.CO;2.

Zeng, C., and E. Naylor, 1996. Synchronization of endogenous tidal vertical migration rhythms in laboratory-hatched larvae of the crab *Carcinus maenas*. *Journal of Experimental Marine Biology and Ecology*, 198: 269–289, doi:10.1016/0022-0981(96)00004-4.

Zeng, C., and E. Naylor, 2018. Rhythms of larval release in the shore crab *Carcinus maenas* (Decapoda: Brachyura). *Journal of Marine Biological Association of the United Kingdom*, 77: 451–461, doi:10.1017/S0025315400071794.

VITA

Elizabeth Brasseale grew up in Madison, Alabama. She moved to Seattle for her undergraduate education at Seattle University where she completed the University Honors Program and received a B.S. in Physics. She stayed in Seattle for her graduate education in Physical Oceanography at the University of Washington. While in graduate school, she co-founded an Oceanography graduate student zine, *The Touch Tank*.